University of Strathclyde Science

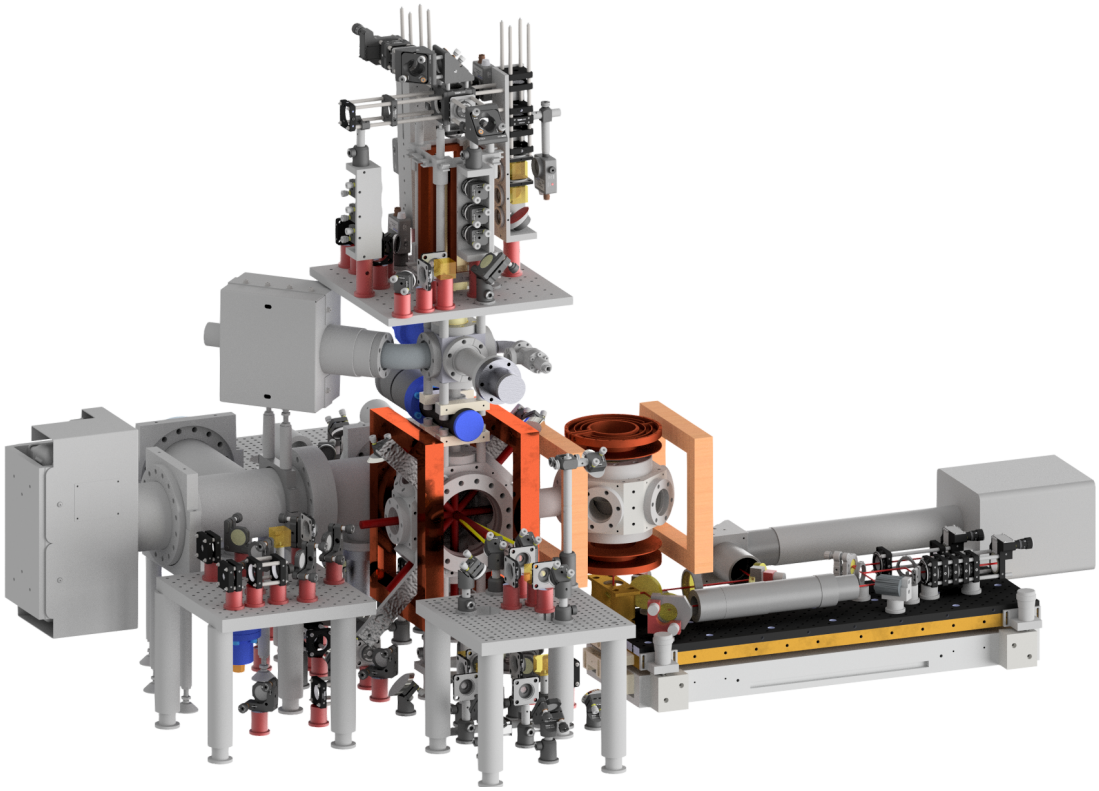

The Construction of a Bosonic Quantum-Gas Microscope

PhD Thesis

Ilian Despard

Experimental Quantum Optics and Photonics Group

Physics

University of Strathclyde, Glasgow

June 6, 2022

This thesis is the result of the author's original research. It has been composed by the author and has not been previously submitted for examination which has led to the award of a degree.

Signed: Ilian Despard

"Let us fight for a new world - a decent world that will give men a chance to work - that will give youth a future and old age a security.

By the promise of these things, brutes have risen to power.

But they lie!

They do not fulfil that promise.

They never will!

Dictators free themselves but they enslave the people!

Now let us fight to fulfil that promise!

Let us fight to free the world - to do away with national barriers - to do away with greed, with hate and intolerance.

Let us fight for a world of reason, a world where science and progress will lead to all men's happiness"

Charlie Chaplin, The Great Dictator

Abstract

Quantum-gas microscopy has proven to be a valuable tool for the field of quantum simulation. It provides single-atom and single-site resolution for atoms contained within an optical lattice. This has enabled the study of Hubbard models for both bosons and fermions, the observation of quantum walks and the probing of complex dynamical systems out of equilibrium.

This thesis presents the construction of a quantum-gas microscope for ^{87}Rb that achieves single-atom and single-site imaging resolution. I start with presenting the theoretical models which describe the physics of an ultra-cold cloud of atoms cooled to form a Bose-Einstein condensate. I present the creation of an all-optically cooled condensate of 3×10^5 atoms in a time of less than 4 s which is initially cooled through the use of grey molasses cooling on the D_2 line. Following this, I present the experimental procedure for creating a 2D system of ultracold atoms, at quantum degeneracy, contained within a 3D optical lattice. The 2D system is then imaged using a large NA objective and single-site resolved images are obtained.

During the conclusion of this thesis, preliminary results are presented showing the creation of a Mott insulator and a discussion on the future of the experiment, including the introduction of a second bosonic species, ^{85}Rb.

Contents

List of Figures

List of Tables

Acknowledgements

I can honestly say that without my beautiful fiancee Nicola I would not be where I am today. She has been my continued rock and has always believed in my scientific goals. She has provided me with the strength and determination to keep going when the times got tough. I will be forever in your debt.

I would like to thank Prof. Stefan Kuhr for believing in my scientific ability and providing me with a test bed for the development of my core skills. His continued input, support and enthusiasm has helped inspire me to be a better scientist. I am extremely grateful for all the help provided by Dr Elmar Haller, Dr Paul Griffin and Dr Jonathan Pritchard. My continuous onslaught of questions would of been enough to drive anyone mad and your unflinching patience was deeply appreciated. For my time in Japan I am thankful to Prof. Yoshiro Takahashi for welcoming me to his team and allowing me the opportunity to work on a fascinating project with amazing and talented individuals.

Andrés and I have formed a great continued friendship through the love of physics, video games and climbing. It was always an interesting time in the lab with you and there was never a dull moment between the never ending breaking and fixing cycles. For my daily dose of Italian current news I must thank Andrea. His love of physics and his humour had kept me going on those long days when I was sure to be the idiot of the day. To the rest of the team that I had the pleasure of working with; Arthur, Hari, Craig, Bruno, Manuel and the new students, I am thankful for all the useful conversations and more importantly laughs we had. A special thanks must be given to Maximilian, he pushed me to learn more, work harder and be more committed to my

craft.

A final thanks must be given to everyone in the EQOP group for making it such a pleasant and friendly environment while still pushing each other intellectually. Thank you to everyone I shared an office with for the daily words of motivation and the never ending stream of laughs we had.

Chapter 1

Introduction

Can the description of a single particle be easily scaled to describe a large ensemble of particles? Although systems containing single particles are well described by the single-particle Schrödinger equation [4], as soon as the system size increases to even a few atoms, the complexity grows substantially. An issue that quickly arises when simulating large, complex, quantum systems, is the exponential growth of the Hilbert space. A single-particle, two-level quantum system with states $|0\rangle$ and $|1\rangle$, has a wavefunction which can be described through

$$|\Psi\rangle = c_1|0\rangle + c_2|1\rangle, \tag{1.1}$$

where c_1 and c_2 are complex amplitudes, with $|c_1|^2 + |c_2|^2 = 1$ [5]. If the particle number, N, is increased, the total number of unique coefficients required to describe a multi-particle quantum state scales as $2^N - 1$, rather than N. This exponential increase of required storage capacity rules out classical computers for simulating large quantum systems. Even if every complex coefficient only required a single bit of storage space, for just 55 two-level atoms, the total storage space required becomes 72 PB. The fastest supercomputer in the world (Fugaku, Japan), has a total physical memory of 4.85 PB, which would mean, if it could run the calculation, it would have nowhere to store the data. If the number of particles was raised to just 300, the total number of required

coefficients outweighs the overall number of particles in the universe ($> 10^{88}$) [6]. John Preskill described the impossibility of achieving enough data storage by stating, "it will never be possible, even in principle, to write that description down" [7].

Quantum computing replaces the classical bits (1 and 0) with quantum bits (equation 1.1), known as qubits. A quantum system of N two-level atoms represents N qubits. A quantum computer with such a number of qubits would result in an overall reduction in the required resources [5, 8] for a calculation. The ultimate, most suitable platform for a universal quantum computer is still unknown but work is being developed on a number of technologies, such as: superconducting circuits [9–11], trapped ions [12–14], photonic circuits [15–18], neutral Rydberg atoms [19–21], cavity-QED systems [22], silicone chips [23] and quantum-gas microscopes [24].

Richard Feynman, remarking on the possibility of simulating quantum systems with such a new type of computer, stated that, "with a suitable class of quantum machines you could imitate any quantum system, including the physical world" [25]. Feynman was describing a quantum simulator, one quantum system which could imitate another. Quantum simulation can be considered a sub-discipline of quantum computing: whereas a quantum computer aims to simulate complex problems by running calculations on the platform with the aid of quantum algorithms, analog quantum simulators are instead built in such a manner that they can imitate another complex quantum system with a high degree of controllability. A quantum-gas microscope (QGM) is a specific type of analog quantum simulator using ultra-cold neutral atoms, which are contained within a 3D optical lattice and imaged with single-atom resolution [24, 26]. The experimental techniques required for creating such a system have been developed over the course of the last three decades. The advancement of laser technologies has been primarily driven by the telecommunications industry but has benefited the scientific community just as much. Laser cooling [27, 28] and trapping [29, 30], which was the focus of many experimental cold-atom groups in the late 1980s and 1990s, eventually combined with evaporative-cooling methods [31, 32], and resulted in the creation of a Bose-Einstein condensate (BEC) in 1995 [33, 34]. However, it took a further six years for the all-

optical creation of a BEC to be achieved [35].

The idea of using a BEC in an optical lattice for the realisation of a controllable Bose-Hubbard model was first theorised in 1998 [36] and has since been described as fundamental work that "shaped the research in the new field of quantum science" [37]. Cold atoms had already been studied within optical lattices [38]; however, cold thermal atoms would not all occupy the ground state of the system [39,40]. Adiabatically loading a BEC into an optical lattice provided the solution to this problem. A number of experiments were undertaken by combing the BEC with optical lattices [41, 42]; however, it was not until 2002 when the quantum phase transition between the superfluid and Mott-insulating regime was experimentally shown [43]. This achievement was seen as a breakthrough for the field of quantum simulation with ultra-cold atoms and opened up in particular the possibility of simulating condensed-matter physics [24, 44–47].

Experimentally showing the quantum phase transition between the superfluid and Mott-insulating regime was a huge achievement, although, the images presented in [43] are that of an ensemble of atoms observed in momentum space it does not provide information on the position of individual atoms in the optical lattice. It was not until 2009 and 2010 when optical lattice experiments were paired with high-resolution objectives to allow for single-site-resolved images of ultra-cold bosonic atoms [24, 26]. This achievement opened up a range of research directions, not limited to the study of correlation functions [48, 49], spin propagation [50], many-body localisation [51], entanglement entropy [47] and the observation of quantum walks [52]. However, it took almost five years for single-site-resolved images of fermionic species to be reported [53–55], which was followed by the first reported cold-atom Fermi–Hubbard antiferromagnet [56–58].

Quantum-gas microscope experiments have the option to realise single-site addressing. A basic implementation of this technique involves a single, diffraction-limited beam, focused on an individual lattice site that can be utilised to address any single atom in a 2D system [45, 59]. In order to create more complex scenarios, light can be projected onto the atoms by a spatial light modulator, which can create diffraction-

limited artificial potentials [60] of almost arbitrary 2D [61] and 3D [62] arrangements of atoms.

The field of quantum-gas microscopy has grown dramatically over the last decade with over a dozen machines currently in service, spread across numerous research groups [24,26,53,54,63,64]. The methodology behind the construction of such a machine is now well understood. Our group is building our second machine - which is rather different from the original one built in 2009. We are implementing additions to make the setup smaller, easier to use, easier to reconfigure and more importantly, be able to introduce a second species. A number of groups are now also building their next generation quantum-gas microscopes [65]. One of the main driving forces behind this work is to reduce the experimental repetition rate. Quantum-gas microscopes often have a slow repetition rate of $20-60$ seconds [24, 26, 53, 54] with the most competitive closing in on sub 10 seconds [66]. A faster repetition rate would open up the possibility of a more in-depth statistical study of complex many-body effects such as correlations and out-of-equilibrium dynamics. A faster cycle time will also enable a quantum-gas microscope to stay competitive with other quantum simulation platforms such as, superconducting chips, Rydberg systems, photonic systems and trapped ions. [9, 67–69].

Thesis outline

The goal of this work is to describe the methods required to design, assemble, test and run a bosonic quantum-gas microscope. Presented within this thesis are the steps involved in reducing the cycle time of the experiment while still maintaining a large atom number throughout. The work outlined here will act as the initial groundwork for the creation of a dual-species quantum-gas microscope capable of simulating complex out-of-equilibrium dynamics. This thesis is structured in the following manner:

- **Chapter 2** provides the theoretical background required to take a warm vapor of ^{87}Rb gas and cooling until a BEC is created.

- **Chapter 3** describes the experimental setup and the steps undertaken in cooling a cloud of atoms to degeneracy. However, it only briefly mentions the required laser systems and a more detailed description can be found in the thesis of Andrés Ulibarrena Díaz [70].

- **Chapter 4** provides an in-depth summary of the methods required to trap atoms within a single antinode of an optical lattice and create a 2D system.

- **Chapter 5** describes imaging single atoms with single-site resolution and provides a detailed analysis of the precise alignment of the microscope objective to ensure the atoms are imaged correctly.

- **Chapter 6** examines several experimental additions to the apparatus which are currently under development. It concludes with a brief overview of the work presented in this thesis.

Chapter 2

Foundations for the creation of a Bose-Einstein condensate in an optical lattice

W. Ketterle, commenting on the thoughts of his peers in the early 1990's towards atomic gases and the creation of a BEC wrote, "Laser-cooled alkali atoms were not regarded as a top contender" [71]. Looking at it now, it is impossible to imagine a world where ultracold atomic gases of alkali atoms are not the workhorse of almost all BEC experiments. Key to the creation of a BEC are the laser-cooling techniques which were first developed for alkali atoms almost thirty years ago. Doppler cooling [72], magneto-optical traps (MOTs) [73], sub-Doppler cooling [74, 75] and forced evaporation [76] are all techniques taken for granted by younger students now, but were major technical milestones at the time.

Being able to understand each cooling method is vital for the creation of an ultracold cloud of atoms. This chapter will discuss the basic concepts of each laser-cooling method used in our experiment along with the key tools used to characterise a Bose-Einstein Condensate. This chapter is structured in the same order as the experimental procedure, starting from a room-temperature vapour of alkali atoms all the way to bringing the atoms into a single ground state at quantum degeneracy. It concludes

with a brief description of atoms in optical lattices and the Bose-Hubbard model. This is by no means an explicit description of all the underlying physics involved in the process of going from vapor to BEC but rather stresses more the core concepts. Please see the following books and papers if further information is sought [77–79].

2.1 Laser cooling

2.1.1 Doppler cooling

In order to laser cool an atom, a well-defined optical transition is required. In the atom's frame of reference an incident photon with frequency equal to this transition frequency can be absorbed by the atom, while having the atom gain momentum in the direction of propagation of that photon. The excited atom then emits a photon after a time which is proportional to the inverse of the natural linewidth of the transition, causing a momentum kick in a random direction. This produces a force due to the momentum transfer of photons for both the absorption and emission processes. The velocity of the atom causes a shift of the transition which can be larger than the natural linewidth. This can be used to address particular velocity classes of a cloud of atoms. The Doppler-shifted frequency as seen by the atom is

$$\omega' = \omega - \vec{k} \cdot \vec{v}, \tag{2.1}$$

where $\vec{v}$ is the velocity of the atom and $\vec{k}$ is the wavevector of the light. If the atom is moving in the direction of the resonant beam, then the frequency required for the excitation will be positively offset from resonance (blue shifted). However if the atom is moving towards the laser, the frequency of the transition is reduced and is red shifted [80]. This lead to the development of Doppler cooling for atoms [81], where the cooling laser would purposely have its frequency red detuned from resonance such that, when the atom is moving towards the beam, it would absorb more photons than

when it was moving away. Having two counter-propagating beams in each axis, one can cool the atom to a minimum temperature along three dimensions. The minimum achievable temperature with Doppler cooling is called the Doppler temperature, and is given by [82]:

$$T_D = \frac{\hbar\Gamma}{2k_B}. \tag{2.2}$$

The Doppler temperature is only dependent on the natural linewidth of the atomic transition, Γ. For ^{87}Rb excited on the $5^2S_{1/2} \rightarrow 5^2P_{3/2}$ transition, this corresponds to $T_D = 145$ µK [2]. This temperature is roughly the same for all the alkalis on the D1/D2 transitions and is still high compared to the temperatures required for the creation of a Bose-Einstein condensate ($\approx$ 100 nK). However, not all transitions have the same linewidth, dipole-forbidden transitions can provide much smaller linewidths. ^{87}Rb has a natural linewidth of $\Gamma = 2\pi \times 6$ MHz, but dipole forbidden transitions in ^{40}Ca have an effective linewidth of $\Gamma = 2\pi \times 5$ kHz [83]: this would result in a Doppler temperature of 120 nK and opens up the possibility of not needing further complicated cooling steps to reach degeneracy [84], as demonstrated in 2013 for strontium [85].

It should be noted that Doppler cooling does not produce a confining force for the atoms and can only be used to cool them. In 3D this leads to a "viscous type" velocity reduction of the atoms, almost like a ball moving through thick honey. Therefore the name "molasses" was coined early on. Doppler cooling can be utilised in conjunction with an external magnetic-field gradient, which will confine the atoms spatially. This configuration is referred to as a magneto-optical trap (MOT), which both cools and traps the atoms.

2.1.2 Magneto-optical trap

A magneto-optical trap builds on the velocity dependence of Doppler cooling by adding a position-dependent restoring force that originates from the Zeeman effect. This tech-

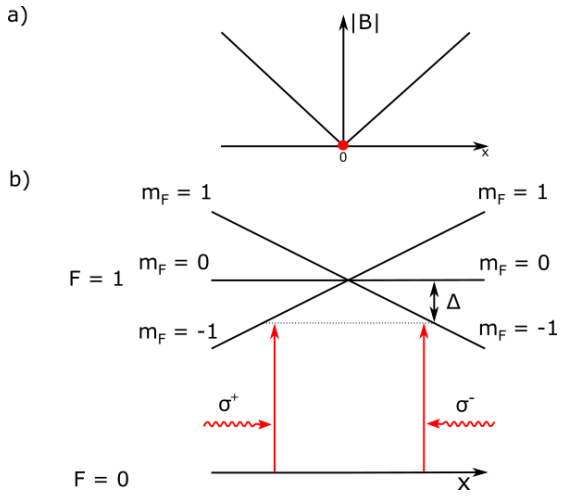

Figure 2.1: A magneto-optical trap in 1D with excited-state Zeeman sublevels shown. a) A cloud of atoms in a quadrupole field at position 0. b) A quantisation axis in the x-direction, sets the effective handedness of the two circularly polarised laser beams. Atoms have their transitions Zeeman shifted by the external magnetic-field gradient. This brings the lasers into resonance with the desired transition when the shift is large enough that it becomes equal to Δ.

nique was first successfully implemented in 3D with sodium atoms in 1987 by the group of D. Pritchard [29, 30] which advanced the previous 1982 work of W. Phillips [28] - who was the first to analyse the position-dependent slowing force created as a result of an external magnetic-field gradient in alkalis.

To better understand how a MOT works, let us first consider the 1D system shown in figure 2.1. A cloud of atoms is at the centre of a quadrupole field - created by a pair of magnetic coils with current flowing in opposite directions. A pair of counter-propagating lasers beams is red detuned from the closed cooling transition of $F = 0 \rightarrow F = 1$. The excited state possesses three Zeeman sublevels, $m_F = -1, 0, 1$. The laser beams both have opposite circular polarisations which correspond to the atomic transitions σ^+, σ^- and is dictated by a positive quantisation axis in the x direction.

An atom starting at zero and moving along x undergoes a linear Zeeman shift. The energy shift of the atom's m_F states is provided by $\Delta E = m_F g_F \mu_B \frac{\partial B}{\partial x} x$ which includes the Landé g factor, g_F, the Bohr magneton, μ_B, and the magnetic-field gradient $\frac{\partial B}{\partial x}$, along x. At some point the shift becomes large enough that the σ^- transition to the

$m_F = -1$ state becomes resonant with the circularly polarised laser beam. Due to selection rules [77] the atom absorbs σ^- light. The imbalance in forces that arise due to the directional dependence of the Doppler shift provides a restoring scattering force[1]

$$F_{\mathrm{MOT}} = -\alpha v, \tag{2.3}$$

which moves the atom back towards the trap centre. The same happens at the opposite side for σ^+, $m_F = 1$. The atoms are cooled by the velocity-selective Doppler cooling and then trapped in the cooling region by a restoring force arising from a position-dependent Zeeman shift. This back-and-forth motion is akin to a 1D damped harmonic oscillator, with equation 2.3 leading to a method of modeling the MOT dynamics [86].

2.1.3 Sub-Doppler cooling

Sub-Doppler cooling is any laser cooling method that can reduce the temperature below the Doppler limit. In our experiment we use a combination of Sisyphus cooling and grey-molasses cooling. Sisyphus cooling (sometimes referred to as red-molasses cooling) is a well-established method for cooling clouds of atoms. It has been studied extensively both theoretically [87,88] and experimentally for a number of alkalis [89–91], molecules [92–94], and various other elements [95,96].

The working principle behind Sisyphus cooling is as follows: a pair of counter-propagating laser beams in the Lin $\perp$ Lin configuration create a polarisation gradient. This gradient changes periodically between linear polarisation and left/right hand circular polarisation on a $\lambda/4$ length scale, as seen in figure 2.2b). The whole system is in a zero magnetic field, such that if there was no incident light, all of the Zeeman sublevels would be degenerate. As such the working basis now transforms from

[1] This assumes a low atom velocity, $kv \ll \gamma$, while only providing a damping force for red detuned beams, $\delta = \omega - \omega_0 < 0$.

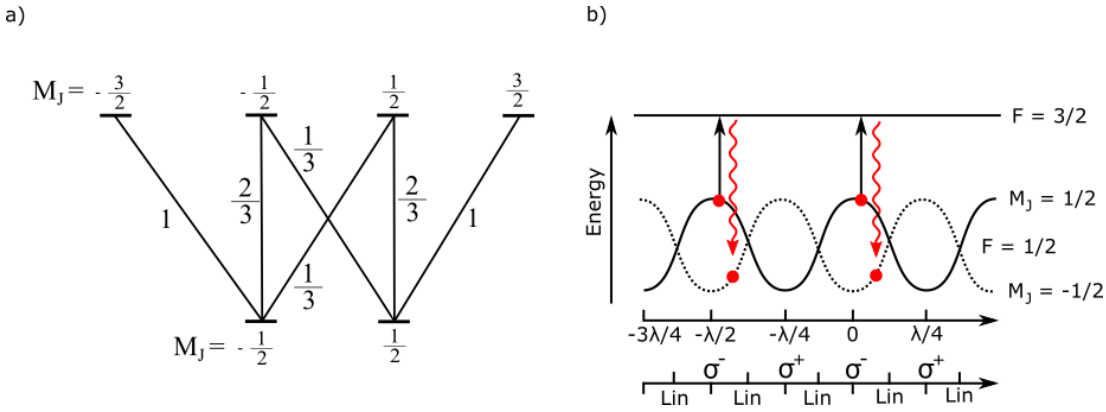

Figure 2.2: a) Relative transition strengths for all possible $J = \frac{1}{2} \rightarrow J' = \frac{3}{2}$ transitions. b) Sisyphus cooling in the Lin $\perp$ Lin configuration. Counter-propagating lasers create a polarisation gradient which varies periodically over a length scale of $\lambda/4$. Atoms are excited to the upper level and then decay back to the ground state. This process reduces the energy of the atoms due to the energy difference between the light shifted ground states.

hyperfine structure to fine structure (M_J). Looking at the structure for an atomic species with ground state $J = 1/2$ and excited state has $J' = 3/2$, this leads to two magnetic sublevels ($m_J = \pm 1/2$) in the ground state and four in the excited state ($m_J = \pm 1/2, \pm 3/2$). The energy of the two ground states varies as the atom propagates in the polarisation gradient [figure 2.2b)]. The Clebsch-Gordan coefficients, which dictate the strength of a transition and are proportional to the AC Stark shift, are largest for the transition between stretched states. This leads to a larger light shift of the $m_J = -1/2(1/2)$ state when the light is $\sigma^-(\sigma^+)$ polarised compared to the other ground state [97]. For the situation in figure 2.2, where an atom starts in $m_J = 1/2$ and reaches a region of circularly polarised light that drives a σ^- transition, the atoms are excited to $m'_J = -1/2$. From here they primarily decay to the $m_J = -1/2$ state. The light shift is different for each ground state, therefore when the atom moves up the potential hill, it transforms kinetic energy into potential energy and causes the atom to lose energy, before transitioning back to the lower energy state. The AC Stark shift is also proportional to the intensity and detuning of cooling light used, $\Delta\omega \propto \Omega^2/(4\delta)$ where $\Omega^2 \propto I$ [77]. Therefore in order to have the dipole force dominate over the scattering force, the atoms need to be moving through the spatially oscillating dipole

potential and not slowed due to scattering events. This leads to cooling beams either being low intensity with small detunings, or high intensities with large detunings.

Sisyphus-cooled atoms are constantly cycling up the potential hill caused by the light shift and then decaying back down. Sisyphus cooling allows for sub-Doppler temperatures to be achieved but is limited by the absorption and emission of a single photon. This adds and removes one recoil of energy every cycle [98]. The recoil energy in terms of temperature is given as

$$T_{\text{recoil}} = \frac{\hbar^2 k^2}{m k_B}, \tag{2.4}$$

with a value of 368 nK for ^{87}Rb. Experimental work has shown that the lower limit to the achievable temperatures with Sisyphus cooling are the order of $1 - 3$ µK for alkalis [99–102].

It should also be noted that Sisyphus cooling does have an upper limit of starting temperatures that it will efficiently cool at. As the atoms are moving through the polarisation gradient they do require some time in order for their internal states to follow the gradient adiabatically [27]. If the atoms are moving too fast, then the cooling method does not work efficiently as the polarisation has changed before an absorption and emission cycle has occurred.

2.1.4 Grey-molasses cooling

Grey-molasses cooling is another form of sub-Doppler cooling which can reach temperatures close to the recoil limit [103]. Grey-molasses is essentially a Sisyphus-enhanced velocity-selective coherent population trapping process[2]. It can be seen as an "upgrade" to Sisyphus cooling as the Sisyphus cooling process is still present but is now combined with population trapping within dark states of the system. Atoms cooled into a dark

[2]This statement is only true for a Lambda configuration of beams with an incident repumper.

state which still have a large kinetic energy motionally couple to a bright state, where they can participate in the scattering cycle. This quickly cools the atoms to the dark state and the process is repeated until the atoms become cold enough to remain in the dark state. As a result, the average temperature of the cloud is decreased.

A dark state is comprised of linear superpositions of Zeeman sublevels and the excitation of an atom out of such superposition state is dependent upon selection rules due to the local polarisation of light. It is well known that superposition Zeeman dark states can be created in an $F \rightarrow F' = F, F-1$ transition for particular polarisations of light, such there are no possible transitions available to the atoms due to selection rules. Even in a more complex system where three pairs of counter-propagating beams are used, these dark states are still created [104]. The polarisation gradient created by counter propagating cooling beams results in atoms within the lowest velocity class to remaining adiabatically dark. This dark state is maintained as the linear superposition state has sufficient time to adjust to the changing polarisation due to the low velocity of the atoms. If an atom is moving at such a velocity that it can not adjust to the polarisation gradient, then it is motionally coupled to a bright state where it undergoes a Sisyphus cooling process [105] and provides the loss mechanism for the energy of the atoms.

To better describe grey-molasses cooling we will start with a 1D Lin $\perp$ Lin configuration of counter propagating beams in zero magnetic field as seen in figure 2.3. The level system $F \rightarrow F' = F$ is of interest here. A particular requirement for grey-molasses cooling is that the cooling beams have to be blue detuned from resonance. Atoms which are absorb blue detuned light have a higher probability of losing more energy as they now have to first climb the "potential hill", before being pumped back into the dark state [106]. This puts the energy of the bright states above that of the dark states and ensures the temperature achieved with grey-molasses are lower than that obtainable with Sisyphus cooling alone [107].

Assuming all atoms start in the dark state and they are within a particular pure polarisation (σ^+/σ^-) of the cooling beam, they have a dark-state lifetime which varies

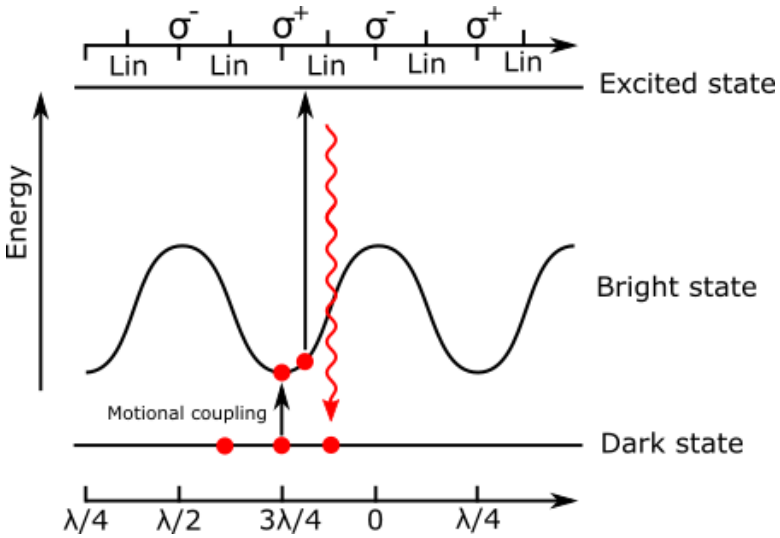

Figure 2.3: A simple grey-molasses cooling diagram where atoms start in the ground state and are then motionally coupled to a bright state where they can undergo Sisyphus cooling. After cooling atoms are pumped back into the dark state. Only one bright state is shown for convenience. Adapted from [107].

as the square of the atom's velocity [108]. They are removed from the dark state due to motional coupling to a bright state - which happens in the region of purely circularly polarised light [109], when the energy difference between the dark and bright states are closest. Motional coupling happens as the atom is moving too fast to adiabatically follow the changing polarisation field and therefore drifts into a region where the polarisation of the light can now couple to the atom. Once in this bright state they can undergo Sisyphus cooling to return them to the dark state [110]. This slows the atoms down and dissipates the energy of the cloud. If the velocity of the atom is small enough, it can adiabatically remain in the dark state and stays there almost unperturbed [104] until reaching another region of circularly polarised light. The colder the atom is, the more time it spends in the dark state with the energy of the dark state always remaining constant. The dark state is kept almost fully populated throughout the propagation over a distance of $\lambda/4$ (see figure 1 of [104]), except for when the energy differences between the dark and ground state are close. Grey-molasses cooling is experimentally investigated in section 3.1.9.

There are two main limitations to grey-molasses cooling. The first is due to the

experimental control over the stray magnetic fields within the lab. Molasses cooling in general works best in a zero magnetic field due to the degeneracy of the Zeeman sublevels. Experimentally, the zero-field region is often small compared to the size of the cloud and not very symmetrical, which can lead to an increase in temperature in one section of the cloud: as not all of the atoms undergo the same efficient cooling process. The second is the polarisation of each cooling beam. In the 1D picture, described in the last few pages, we assume they are identical, but this is never the case in 2D/3D systems, as the polarisation gradients created are not uniform. One advantage to using grey molasses over red molasses, is that the cooling process is less density dependent [111]. This has lead to temperatures of 1 µK for 10^9 atoms of ^{87}Rb in our experiment. Separate experiments have managed to measure 800 nK [91] and 1.1 µK in Cs [110] and 4 µK in Rb [109]. In our experiment, we use a repumper and cooling laser both blue detuned from the excited state and phase-coherent with each other. The phase coherence has been shown to greatly decrease the temperature of the atoms and increase their phase-space density when compered to non phase-coherent beams [109]. This phase coherence is crucial for maintaining the superposition (dark states) between the hyperfine ground states of ^{87}Rb.

2.2 Bose-Einstein condensation

Under the exchange of two particles, identical bosonic particles maintain a symmetry between their wavefunctions. As a consequence, bosons have a unique property that below a critical temperature T_c, they can occupy the same quantum state, typically the ground state. As all atoms in the ground state have identical wavefunctions, such systems experience coherent effects [112] and become a new state of matter, known as a Bose-Einstein condensate. Reviews of the history of Bose-Einstein condensation and the works leading to the creation of a BEC can be found in [113–117]. A brief summary shall be given below.

Bose condensation was first theorised by Bose in 1924 [118] in which he analysed the quantum statistics of photons. This idea was later elaborated to matter particles

by Einstein in 1924/1925 [119]. However the first creation of a BEC was not until 1995 when the group of Wieman and Cornell performed a series of beautiful experiments with dilute rubidium vapours [33]. Parallel to this work, Ketterle et al. also created a BEC of sodium atoms [34], the combined works earned the three researchers the Nobel prize in 2001.

To fully describe the creation of a BEC and the properties that it possesses, we will start by considering how a cloud of non-interacting bosons is distributed at a non-zero temperature in a harmonic trap. The harmonic trapping potential is given by:

$$V_{\text{ext}} = \frac{m}{2}\left(\omega_x^2 x^2 + \omega_y^2 y^2 + \omega_z^2 z^2\right), \tag{2.5}$$

where m is the mass of the atom and $\omega_{x,y,z}$ are the trap frequencies in the three spatial dimensions. At thermal equilibrium, a Bose-distribution function can be used to calculate the average particle number, N, of a BEC from the grand-canonical ensemble and be derived to [120]:

$$N(v) = \frac{1}{e^{(E_v-\mu)/kT} - 1}, \tag{2.6}$$

with the temperature of the cloud T, the chemical potential μ and E_v being the energy of the single-particle state v, which can be calculated from the external harmonic trap. By knowing the state distribution and recalling that the cloud is in a harmonic potential, one can calculate the critical temperature and in turn the critical atom number, for which a BEC is created at [121]:

$$T_c = \frac{0.94\hbar\bar{\omega}N^{1/3}}{k_B}. \tag{2.7}$$

Here, $\bar{\omega}$ is the geometrical mean of trap frequencies i.e $\bar{\omega} = \sqrt[3]{\omega_x\omega_y\omega_z}$. Below this

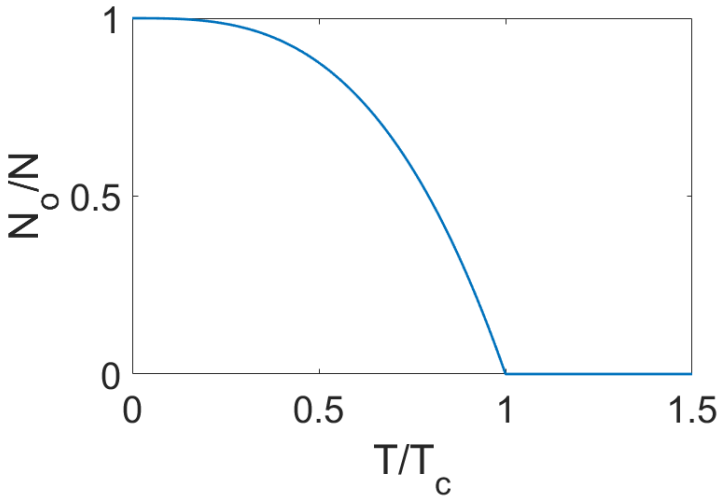

Figure 2.4: Ideal condensation fraction N_0/N as a function of T/T_c, resulting from equation 2.8.

critical temperature, a cloud of atom number N will condense. Condensation can also be achieved by increasing the density of atoms within a fixed volume as long as the temperature remains constant. This would then correspond to a critical density rather than temperature. One can derive scaling conditions between atom number and critical temperature. The elegant equation 2.8 is the result for atoms confined within a harmonic trapping potential. It relates the ratio between the temperature T of the cloud and the critical temperature T_c, to the ratio of atom number in the BEC N_0 and total atom number N, of the system (see figure 2.4),

$$\frac{N_0}{N} = 1 - \left[\frac{T}{T_c}\right]^3 . \tag{2.8}$$

2.2.1 Phase-space density

The phase-space density (PSD) is a useful quantity to characterise a cloud during evaporative cooling and can provide information on the efficiency of the evaporation. In order to calculate the PSD, we first need to look at the useful length scales in

the system - the deBroglie wavelength and the interatomic spacing. The deBroglie wavelength,

$$\lambda_{dB}(T) = \sqrt{\frac{2\pi\hbar^2}{mk_BT}}, \tag{2.9}$$

can become comparable to the interatomic spacing, $d = \bar{n}^{-1/3}$ [77] where $\bar{n}$ is the mean particle density. Once this happens, atoms can begin to condense into a single state. One can interpret the deBroglie wavelength as the length scale over which the wavefunction of an atom extends. It is then natural to quantify the overlap of wavefunctions between atoms within a particular volume as:

$$PSD = \bar{n}\lambda_{dB}^3. \tag{2.10}$$

The phase-space density, given in equation 2.10, utilises the three-dimensional volume that an atomic wavefunction occupies and the peak density of atoms in a cloud, to calculate an effective overlap between their wavefunctions. More rigorously, it can be described as the number of occupied quantum states per volume [120]. Due to the length scales at play, the phase-space density is required to be of unitary order for the creation of a BEC. From statistical mechanics in 3D, it has been evaluated that, at the transition point to a Bose-condensation in an harmonic potential, the phase-space density of a sample is 2.6 [122].

2.2.2 Atoms in a single ground state

In the situation where atoms are confined within a harmonic potential, the harmonic oscillator length becomes a relevant length scale for working with. It is given by

$$a_{ho} = \sqrt{\frac{\hbar}{m\bar{\omega}}}. \tag{2.11}$$

For atoms in a cloud at $T < T_c$ with relevant length scales described above, interactions between particles in this ground state become important. To better describe the effect of these interactions, we will look at the physics of interacting atoms in the ground state of a harmonic oscillator.

Up to this point I have described the thermodynamics of bosonic atoms being cooled until they undergo a phase transition and condense. To evaluate a complete description of the system in this ground state, we will account for the interactions between the atoms. The Hamiltonian for a system of interacting particles in a harmonic potential $V_{ext}(r)$ is given by:

$$H = \sum_{i=1}^{N} \left[-\frac{\hbar^2}{2m}\nabla_i^2 + V_{\text{ext}}(r_i) \right] + \frac{1}{2}\sum_{i=1}^{N}\sum_{j\neq i}^{N} V(r_i - r_j) \tag{2.12}$$

At $T = 0$, we assume all the atoms occupy the same quantum state with wavefunction $\Psi(r,t) = \sqrt{N}\prod_{n=1}^{N}\psi(r_i,t)$. By variational calculation it is possible to derive the time-dependent Gross-Pitaveskii equation [123]:

$$i\hbar\frac{\partial}{\partial t}\Psi(r,t) = \left[-\frac{\hbar^2}{2m^2}\nabla^2 + V_{\text{ext}}(r,t) + g|\Psi(r,t)|^2 \right] \Psi(r,t) \tag{2.13}$$

which describes the time evolution of the total wavefunction within an external potential V_{ext} with an interaction coefficient $g = \frac{4\pi\hbar^2 a}{m}$. The wavefunction $\Psi(r,t)$ can be normalised to the total atom number N, such that:

$$\int |\Psi(r,t)|^2 dr = N. \tag{2.14}$$

Independently, both Gross and Pitaevskii derived equation 2.13 in 1961 [124, 125]. They also both described the transformation to a static, time-independent potential in a mean-field approach. This is given by:

$$\mu\psi(r) = \left[-\frac{\hbar^2}{2m}\nabla^2 + V_{\text{ext}}(r) + g|\psi(r)|^2\right]\psi(r). \tag{2.15}$$

Equation 2.15 can be solved numerically and even in some simple cases analytically. An analytical solution can be derived by looking at the ratio between kinetic energy per particle and the interaction energy. For a large number of atoms in the same state, an approximation can be made between atom number N, scattering length a and harmonic oscillator length a_{ho}. If $Na/a_{ho} \gg 1$, then the kinetic energy term in equation 2.15 can be neglected. This is known as the Thomas-Fermi approximation. This approximation provides an analytical solution for equation 2.15. From this exact solution one can evaluate the parameters for which the particle density $|\psi(r)|^2 = 0$ with $V_{ext} = \mu$. This is the Thomas-Fermi radius and is given as:

$$R_{TF} = a_{ho}\left[\frac{15Na}{a_{ho}}\right]^{1/5}\frac{\omega_{ho}}{\omega_i} \tag{2.16}$$

where ω_i denotes the trapping frequency in x, y and z and provides a peak density $\bar{n} = \mu/g$. This is valid as long as the Thomas-Fermi approximation remains true. As soon as the kinetic energy starts to become relevant again, other methods are required to account for this in the equation. In our situation we assume that this is never the case and therefore can utilise the Thomas-Fermi radius as another useful length scale for our system. In our experiment we have interacting bosonic atoms in the ground state of a harmonic oscillator which we transfer into optical lattices. To further our understanding of the system we now need to look at the physics of atoms in optical lattices.

2.3 Atoms in optical lattices

2.3.1 Optical lattices

The optical lattice is a particular configuration of an optical dipole trap. An optical dipole trap provides a conservative trapping potential through the AC Stark shift and is dependent upon the intensity of the incident light field. These traps are far detuned from resonance, and depending on the detuning, atoms can be attracted (red detuned) or repelled (blue detuned) from regions of maximum intensity.

A standing wave can be created in 1D by two counter-propagating beams of the same wavelength λ overlapped, such that a varying intensity profile along x is created, with spacing $a_l = \lambda/2$. An optical-lattice potential $V_l(z)$, can be derived for alkali atoms inclusive of their hyperfine transitions, but for simplicity to have a simpler level scheme we only consider the D1 and D2 transitions here

$$V_l(z) = -\frac{\pi c^2}{2\omega_{\mathrm{D2}}^3 \Gamma_{\mathrm{D2}}} \left[\frac{2}{\Delta_{\mathrm{D2}}} + \frac{1}{\Delta_{\mathrm{D1}}}\right] I(z), \tag{2.17}$$

where $I(z)$ is the varying intensity profile. Γ_{D2} is the linewidth of the excited state on the D2 line with the detuning on this line being Δ_{D2}. The detuning on the D1 line is given by Δ_{D1}, with $\omega_{\mathrm{D1}} = \frac{2\pi c}{\lambda_{\mathrm{D1}}}$ for the D1 line and $\omega_{\mathrm{D2}} = \frac{2\pi c}{\lambda_{\mathrm{D2}}}$ for the D2 line of ^{87}Rb. The atoms in this experiment are held in a lattice of red detuned light which confines them to the antinodes of the standing wave, where they experience a conservative potential $V_l(z)$, which can be expressed as [126],

$$V_l(z) = V_0 \cos^2(kz). \tag{2.18}$$

The depth of the potential is given by V_0, where the wavenumber of the lattice is

$k = \frac{2\pi}{\lambda}$ [127]. A natural unit of energy when working with ultracold atoms in optical lattices is recoil energy, $E_R = \hbar k^2/2m$. For our system with 1064 nm lattice beams, $E_R \approx h\,2$ kHz. The axial lattice trapping frequency can be calculated from the trap depth and the lattice spacing through [128]

$$\omega_l = \frac{\pi}{a_l}\sqrt{\frac{2V_0}{m}} \tag{2.19}$$

where m is the mass of the trapped atom. For ^{87}Rb atoms trapped in a 1064 nm beam of $\approx$ 100 µm waist and $\sim$ 5 W of power, trapping frequencies on the order of kHz within each antinode of the optical lattice are achieved. This trapping frequency can be orders of magnitude larger than the axial and radial frequencies achievable in single-beam dipole traps.

2.3.2 Bose-Hubbard model

We now look at what happens when multiple, interacting ultracold bosons are trapped in an optical lattice. This configuration can be described by a many-body Hamiltonian [36].

$$\hat{H} = \int d^3r \left[\hat{\psi}^\dagger(r)\left(-\frac{\hbar^2}{2m}\nabla^2 + V(r)\right)\hat{\psi}(r) + \frac{g}{2}(\hat{\psi}^\dagger(r))^2(\hat{\psi}(r))^2\right] \tag{2.20}$$

where $\hat{\psi}(r)$ and $\hat{\psi}^\dagger(r)$ are the bosonic field operators which obey the canonical commutation relations. The interaction term $V_{\text{int}} = \frac{g}{2}(\hat{\psi}^\dagger(r))^2(\hat{\psi}(r))^2$ accounts for the atomic interactions and the scattering length. This Hamiltonian can be expanded for atoms that are in a deep optical lattice such that $\hbar\omega = 2\sqrt{E_R V}$ and the Bose-Hubbard Hamiltonian is reached as per the simplified derivation in [129], with a more in-depth

derivation being found in [130, 131]. In a deep lattice ($> 5E_R$), with all the atoms in the ground state, one can restrict the system to consider just the lowest energy band and ignore the rest.

The eigenstates of the periodic lattice potential have a generic form of a Bloch wave, which incorporates a Bloch wavefunction, with period a_l. By restricting them to the first Brillouin zone, this produces Bloch waves with quasimomentum between $\pm 2\pi/a_l$. Bloch wavefunctions are energy eigenstates and describe an atom that is fully delocalised across the whole lattice. A complementary and equivalent description of the state of the atoms can be given in terms of a localised wavefunction on an individual lattice site, i. Such wavefunctions are named Wannier functions $w_i(x)$ [45]. Wannier functions provides useful information regarding how an atom interacts with others on the same site.

The Hamiltonian in equation 2.20 can be simplified with the previously mentioned approximations to what is known as the Bose-Hubbard model

$$\hat{H} = -J \sum_{\langle i,j \rangle} \hat{b}_j^\dagger \hat{b}_i + \frac{U}{2} \sum_i \hat{n}_i(\hat{n}_i - 1) - (\mu - \epsilon_i) \sum_i \hat{n}_i. \tag{2.21}$$

The tunneling matrix element for atoms tunneling from site j to site i is given by J, and the annihilation and creation operators are $\hat{b}_i$ and $\hat{b}_j^\dagger$, respectively. The onsite number operator is given by $\hat{n}_i$, and U is the on-site interaction energy. The last term introduces the on site chemical potential, $\mu - \epsilon_i$, which is due to the external trapping potential of the lattice beams.

Both J and U are normally calculated numerically. The onsite interaction energy U is calculated based on the fact that two atoms on the same site are in the same state,

$$U = \frac{4\pi\hbar^2 a}{m} \int |w_i(x)|^2 |w_i(x)|^2 dx. \tag{2.22}$$

The scattering length of atoms with mass m, is given by a, where the integral of this equation accounts for the overlap of the density of both identical atoms on the same site - with $|w_i(x)|^2$ being the density of Wannier states [131]. The tunneling matrix element J looks at the energy cost for one atom tunneling between adjacent sites, i and j, with tunneling time $\tau = h/J$,

$$J(i,j) = \int dx w_i^*(x) \left[-\frac{\hbar^2}{2m}\frac{\partial^2}{\partial x^2} + V_0 \cos^2(kx) \right] w_j(x). \tag{2.23}$$

2.3.3 Superfluid-to-Mott-insulator transition

There are two fundamental ground states that occur in a Bose-Hubbard system. A superfluid exists when $J \gg U$, such that we can neglect the interaction term of 2.21. In this non-interacting limit, the atoms are delocalised across the full lattice, with the probability of finding n atoms on one lattice site being described by a poissonian distribution. This results in large on-site number fluctuations [132], with all atoms being phase-coherent with each other. This phase coherence was originally used to confirm superfluidity in an optical lattice and the existence of a Mott insulator by interference (or lack of) of ultracold atoms after releasing from a 3D lattice [43].

In figure 2.5 at zero temperature, the ratio between on-site interaction energy and the tunneling matrix element can be varied to force the atoms to undergo a quantum phase transition. As we start to increase the on-site interactions such that $J \approx U$, the fluctuations in on-site atom number start to decrease. The system passes through the quantum-critical point and the atoms undergo a quantum phase transition.

As the interactions are increased even more to a point where $U > J$, atoms become localised onto single lattice sites. The system can be characterised by looking at the relative strengths of μ and J which leads to the production of the quantum phase diagram seen in figure 2.6. Optical lattice beams with a flat intensity profile would

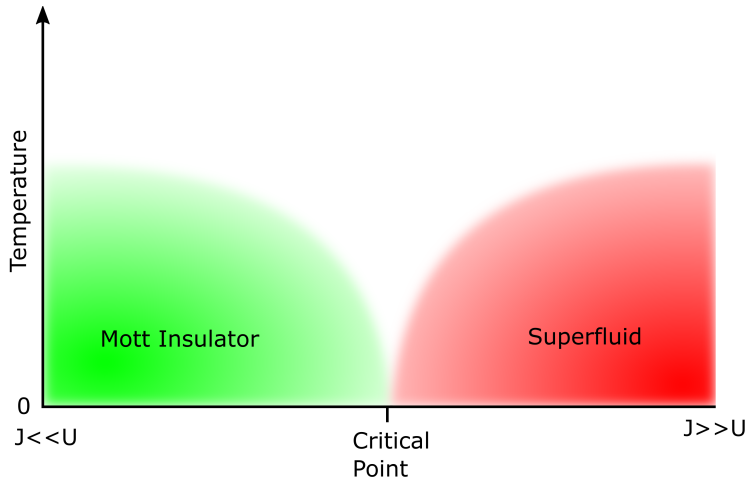

Figure 2.5: Quantum phase diagram inspired by [133]. The diagram presents two regions for ultracold atoms in optical lattices: a Mott insulator regime and a superfluid regime, with a quantum-critical point between the two. At a critical point for a particular value of $\frac{J}{U}$ at zero temperature, a quantum phase transition occurs. At this point atoms can be thought of as in neither a Mott insulator nor superfluid state. Atoms within the quantum-critical regime are tricky to describe properly.

allow for the system to be represented by a single point on the graph. Beams that have a Gaussian intensity profile can be represented by a straight, vertical line on figure 2.6 - as is the case in our experiment - with the top of the line representing the center of the trap and moving downwards represents a move towards the edge of the trap. This results in the cloud not being fully localised across the whole lattice: leading to a portion of the cloud which is superfluid and a portion which is experiencing Mott insulation, with the regions being separated spatially due to the intensity gradient of the lattice beams.

As $U \gg J$ and all the atoms become localised onto single lattice sites, the system is said to be Mott insulating and in the atomic limit. Here lattice sites have integer filling with the tunneling rate between sites being negligible. Unlike the superfluid state, there is no phase coherence between atoms which populate different lattice sites. The compressiblity of the gas is given by $\frac{\delta\langle\hat{n}_i\rangle}{\delta\mu}$ and when equal to zero is described as incompressible [1, 134]. This is one of the defining features of a Mott insulator [135].

Atoms in a Mott-insulating state are excellent for initialising quantum simulation

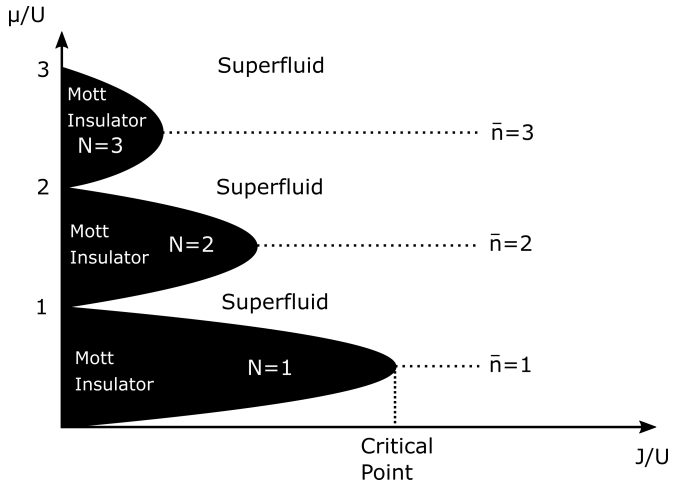

Figure 2.6: A phase diagram showing the variation in onsite atom number due to the positional dependence of chemical potential μ, inspired by [1] for a homogeneous system at commensurate density. For dense clouds μ is highest in the centre and decreases towards the edge. Thus moving outwards from the center results in moving down the y axis. Each region of Mott insulator has a particular μ due to the Gaussian profile of the lattice beams. This results in increasing integer on site occupation.

experiments, as preparing a sample within the lowest lobe of chemical potential provides close to unitary filling of the lattice within a deterministic state. From here any arbitrary atom number distribution of a 2D system can be realised, with the help of single-atom addressing (see chapter 6) or a spatial light modulator (SLM) [45].

Chapter 3

Experimental techniques for the creation of a Bose-Einstein condensate

The following section will describe the apparatus involved in the experiment. The chapter will begin with a description of the vacuum chamber and laser systems. The latter section of this chapter will cover the creation of a large, fast, all-optical Bose-Einstein condensate within the section of vacuum chamber that houses our 3D magneto-optical trap[1]. This chapter will provide a detailed overview of the capabilities of the current apparatus and some maximum experimental parameters, such as the speed of cooling and the cooling efficiencies.

[1]However, when single atoms are imaged, this condensate creation process is not performed in this section of the chamber. Therefore results seen at the end of this chapter will look different from the ones presented in chapter 4 and 5.

3.1 Experimental apparatus

3.1.1 Vacuum chamber

In order to work with ultra-cold atoms and observe them within a trap for long times ($>$ 1 s), heating through background collisions needs to be minimised and a vacuum chamber is utilised to achieve this. Our chamber consists of two sections: a high-vacuum and an ultra-high vacuum section. Pressures of 10^{-11}mbar are routinely achieved within the ultra-high vacuum section, and the high-vacuum section reaches a pressure of 10^{-8}mbar. The high-vacuum section is normally used to house an atomic source, as the residual pressure from the source will dominate. Trapping atoms within a chamber of ultra-low pressure dramatically increases the lifetime of the atoms within the trap to $>$ 1 min, as collisions with other atoms and molecules are reduced [136]. The rate of collisions between background atoms and atoms in the trap can be given by

$$N/\tau = (N\sigma)(n_b\bar{v}), \tag{3.1}$$

where the atom number in trap is N, the collisional cross section σ, the density of background atoms n_b and the mean relative velocity of the background atoms $\bar{v}$ - which is given by the temperature of the vacuum chamber [86].

The chamber is constructed from 316LN stainless steel and a full rendered 3D drawing is shown in figure 3.1. 316LN steel has low nitrogen content and has been specially vacuum annealed to 1000°C to remove as much residual embedded impurities as possible - most notably, hydrogen. As well as having a very low outgassing rate, this material also has low magnetic permeability [137]. This is crucial for quantum-gas experiments, as they need to be able to control the magnetic fields within the chamber very accurately and if the chamber was magnetically permeable, this would

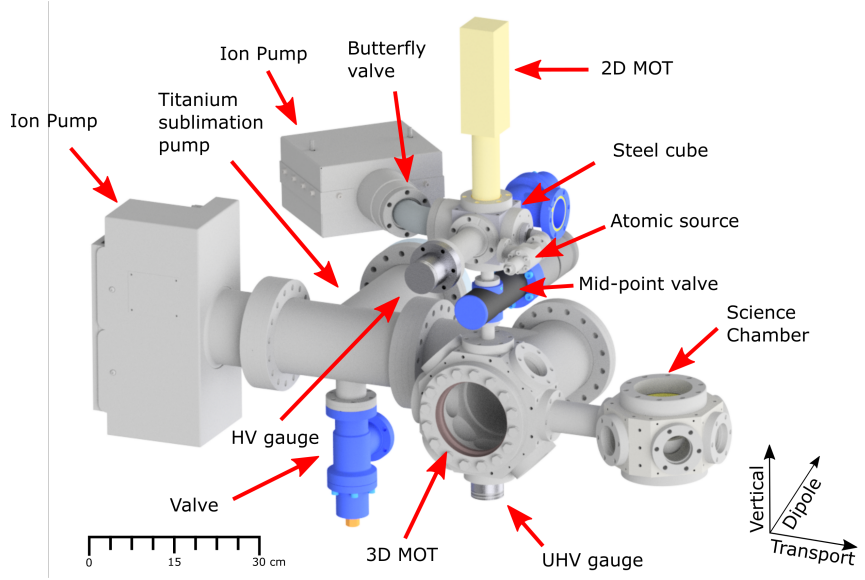

Figure 3.1: A rendered drawing of only the vacuum chamber components of the system.

create residual magnetic fields. The inner surface of the vacuum components have been electro-polished to provide a smooth surface free of defects where virtual leaks could originate. A virtual leak is a slow release of trapped gas within a vacuum chamber which can cause a persistent increase in vacuum pressure. The only part of the chamber which is not primarily made from stainless steel, is the glass cell required for the 2D magneto-optical trap.

The atomic source is a 1 g ampule of rubidium (Sigma-Aldrich 276332-1G) which is held within a small bellow attached to an all-metal valve, such that the amount of rubidium released into the chamber can be controlled. A heating tape is wrapped around the bellow holding the ampule. This tape can change the temperature of the bellow and allows for adjustments of the rubidium pressure.

In order to keep the low pressure within the high-vacuum regime for the 2D-MOT chamber, an ion pump (Agilent Technologies 8 l/s VacIon), encased in mu-metal, is connected to the chamber through a cubic section and a butterfly valve (o-ring removed), such that we can restrict the flow of Rb to the pump. The cubic section acts as an interconnect for all the elements of the high-vacuum section, including a pressure

gauge (Agilent Technologies 9715007). When operating the 2D MOT, we commonly use a pressure of 7×10^{-8} mbar.

The high-vacuum section is connected to the ultra-high vacuum section through a differential pumping tube. This tube is a solid round of 316LN steel, with length 211.5 mm, outer radius of 14 mm and an internal 4 mm hole for the atoms to be move through. The differential pumping tube has a conductance of 3.6×10^{-2} l/s and is compression fit into the 2D-MOT side flange, of an all-metal gate valve (mid-point valve), which acts as a separator of the two pressure sections. The differential pumping tube allows us to hold a three orders of magnitude difference in pressures between each section of the vacuum chamber, which is quite remarkable when considering that the tube is just compression fit into the top of the valve.

The ultra-high vacuum chamber is held at pressures of 10^{-11} mbar. To reach such low pressures two types of pumps are utilised. An active ion pump (Agilent Technologies Valcon 75 l/s), encased in mu-metal, is used to bring the pressure down to $10^{-9} - 10^{-10}$ mbar. To get even lower pressures, a titanium sublimation pump (Gamma Vacuum 360819) is used. A titanium sublimation pump works by passing high current (50A) through a piece of pure titanium to sublimate it into the vacuum chamber. The titanium then sticks to the walls of the chamber and acts as a pump for residual gases such as nitrogen, helium and hydrogen. The pumping efficiency is proportional to the surface area coated by the titanium. To maximise the surface area, we installed an ambient sputter shield (Gamma Vacuum G360190), which has an effective surface area of 167×10^{-3} m^2, which is 2.6 times larger than a conventional DN 100 tube with length 100 mm. Unlike the ion pump, which is permanently on, the titanium sublimation pump is only activated as required. This has only been performed once in four years and the pump was active for 30 minutes with a duty cycle of 1:9 minutes, at a current of 50 A. A pressure of $10^{-11} - 10^{-12}$ mbar is obtained. The pressure in this chamber is measured with a gauge (Leybold IONIVAC-Sensor IE 514) which is capable of measuring pressures as low as 2×10^{-12} mbar.

We commonly refer to the two main sections of the UHV chamber as either the 3D

MOT or the science chamber - as can be seen in figure 3.1. The 3D-MOT chamber is where the 3D magneto-optical trap is created but is also the location for the high-power optical dipole traps. This requires the windows in this section be very large (DN 100) to allow for excellent optical access. The science chamber is the smaller section which is added on to the side of the 3D MOT chamber. Here there are eight different access ports of either DN40 or DN80 in size. This section is placed far enough away from the other components of the system (mechanical translation stage, ion pumps) such that they do not magnetically interfere with the atom cooling and imaging process.

3.1.2 Sequence

It is useful to describe the experimental sequence that is responsible for the creation of a Bose-Einstein condensate. This is different from the sequence used for the creation of a 2D system of atoms but shall provide the reader with structure for the rest of the experiment.

3D magneto-optical trap

Both the 2D MOT and 3D MOT are turned on and a red detuned push beam moves atoms from the 2D to 3D MOT through the differential pumping tube. After loading the 3D MOT, the 2D-MOT lasers and magnetic fields are turned off, inclusive of the push-beam.

Magnetic compression

The quadrupole field responsible for the creation of the 3D MOT is increased while the 3D MOT laser fields are further red detuned.

Sub-Doppler cooling

The magnetic gradient is turned off and the atoms undergo red-molasses cooling. This is immediately followed by a grey-molasses cooling stage.

Crossed optical dipole trap loading

After cooling, two crossed dipole trap beams are incident on the cloud. After loading atoms into the dipole trap, the 3D MOT lasers and quadrupole field are turned off.

Zeeman sub-level pumping

Atoms are transferred to the $F = 1, m_F = -1$ state through an optical pumping pulse followed by a rapid adiabatic microwave transfer. Atoms in all other states are removed using resonant laser pulsed between each transfer stage.

Dimple trap

A tightly focused optical dipole trap ($\omega_0 = 47$ µm) is incident on the center of the cloud to act as a dimple trap and is solely to increase the trap frequency. After which, time is allowed to the atoms for rethermalisation. Later in the experiment this beam is also used to transport atoms to the science chamber and is referred to then as the transport trap.

Pre-evaporation

The crossed optical dipole beams have their power exponentially ramped down in preparation for further cooling the atoms in the combined trap. The dimple trap power is unchanged during this process.

Main evaporation

A joint evaporation of crossed dipole trap and dimple trap is performed simultaneously and a Bose-Einstein condensate is created.

3.1.3 MOT cooling lasers

The lasers required for the creation of a magneto-optical trap (MOT) will be briefly described here and provide the reader with the level structure of ^{87}Rb. A more detailed description of the optical setup can be found in the thesis of A. Ulibarrena [70].

For cooling atoms in a MOT, we require two lasers; one for cooling and one for repumping. The cooling laser is red detuned from the $F = 2 \rightarrow F' = 3$ almost closed cycling transition (red line in figure 3.2). A cycling transition is one in which an excitation is always followed by a decay back to the initial state [78]. The repumping laser is resonant to the $F = 1 \rightarrow F' = 2$ transition and ensures that atoms which decay to the $F = 1$ hyperfine ground state are returned to the cycling transition.

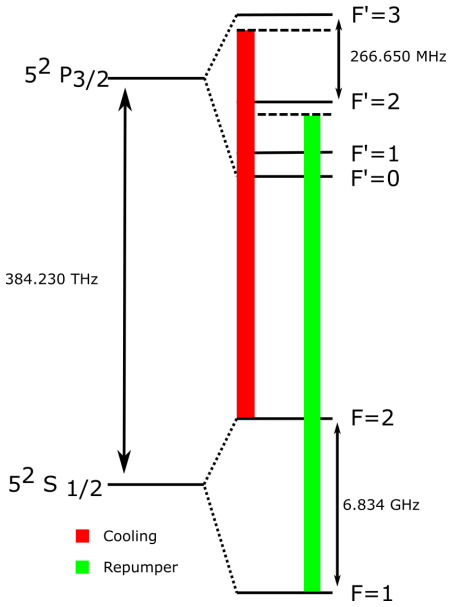

Figure 3.2: Level structure of ^{87}Rb showing the hyperfine structure of the D_2 line with cooling (red) and repumper (green) both red detuned from resonance, adapted from [2].

3.1.4 2D magneto-optical trap

The 2D magneto-optical trap is placed vertically above the rest of the setup in order to save space and increase optical access. The core of this is a 780 nm anti-reflection coated[2] quartz cell (JapanCell), with outer dimensions of 50 × 50 × 150 mm that is connected to a cubic steel cell shown in figure 3.1, where all of the supporting vacuum equipment is mounted. The supporting optics are built onto a breadboard around the glass cell and were pre-assembled and tested offline before being moved into place.

The 2D magneto optical trap is created by three counter-propagating beams in two axis with a quadrupole field in both those axis. A 3D model of this can be seen in figure 3.3. The two vertical towers that house the optics are responsible for the separation of the 1" beams into three paths. The single input beam has 220 mW of power before separation within the tower and is then split equally into the three beams. The beams are retro-reflected using another tower consisting of three mirrors and quarter waveplates. This setup was aligned offline with a 3D-printed mock chamber

[2]Only the external surface of the cell is coated.

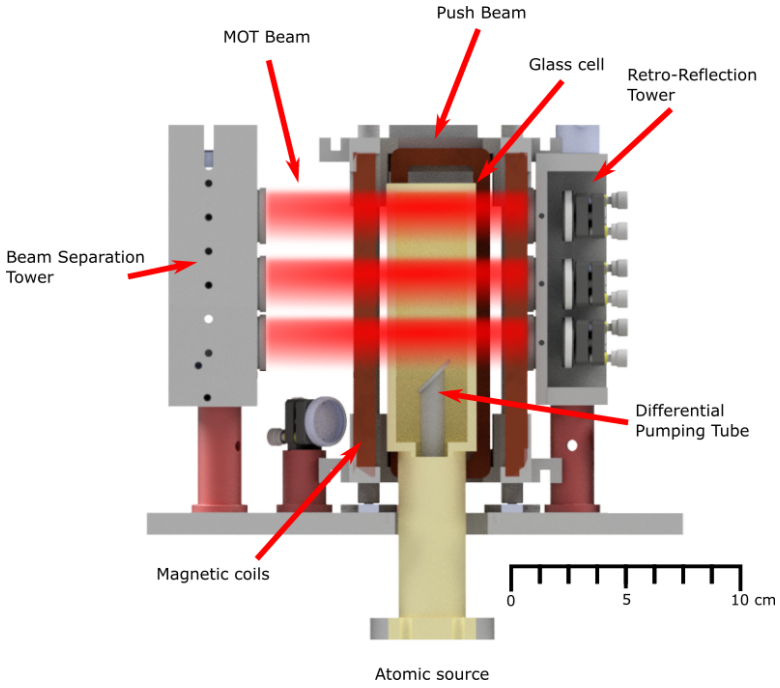

Figure 3.3: A 3D rendered drawing of a vertical cross section of the 2D MOT chamber. The atomic source is attached through the base of the glass cell via the steel cube seen in figure 3.1.

for reference. This provided such good initial alignment that a cooled cloud of atoms was obtained rapidly after mounting the optics to the chamber and optimising the magnetic fields. The quadrupole field is created through the use of four coils which were pre-wound on 3D-printed mounts and then placed into a 3D-printed holder around the glass cell. The material used for printing in this section was PLA, this softens at 60°C, which is hotter than the coils ever reach. The shim coils in the 2D MOT section are also wound around 3D-printed mounts which are then attached to the larger holder of the quadrupole coils. The magnetic gradient used in the 2D-MOT chamber was empirically optimised to 15 G/cm.

The 2D MOT lasers and magnetic fields are turned on for 1 s. The detuning of the cooling laser is $2.6\,\Gamma$ and the repumper is on resonance. During the cooling time, there is also a vertical beam incident on the atoms that acts as a push beam. This push beam is red detuned by $1.4\,\Gamma$ from the $F = 2 \rightarrow F' = 3$ transition. The push beam is aligned vertically downwards through the 2D MOT cell and pushes the atoms

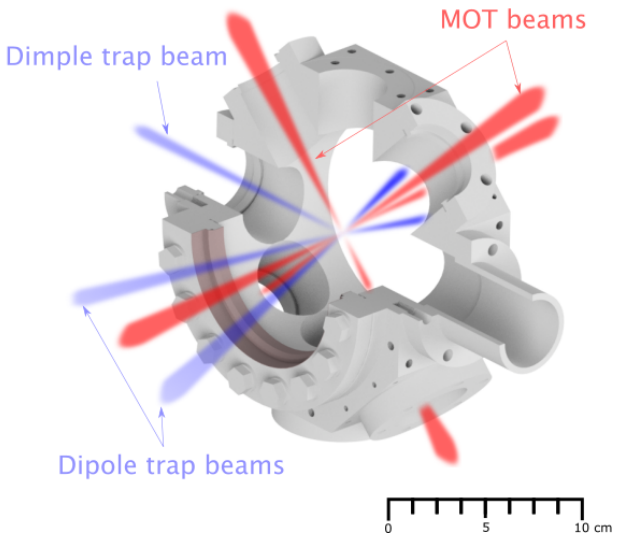

Figure 3.4: Cutout of the 3D MOT chamber with cooling beam paths shown. Note that the dimple trap also doubles as the transport trap later in the experiment.

through the differential pumping tube into the larger 3D MOT chamber. This provides an atomic beam to feed the 3D MOT.

3.1.5 3D magneto-optical trap

A 3D MOT is realised through three perpendicular pairs of counter-propagating beams (red beams in figure 3.4). These pairs of beams are referred to as the 3D-MOT beams and originate from a single home-built tapered amplified system, seeded by a commercially available external cavity diode laser (see [70] for further information). Each of these beams have a $1/e^2$ diameter of 1" and originate from a single fibre on the experiment table which provides 220 mW of power. This single beam is split into six different paths using a combination of polarising beam splitters and $\lambda/2$ waveplates to allow for 36.6 mW of power in each beam. The last element before the chamber in each beam is a $\lambda/4$ waveplate, to ensure the beams have a circular polarisation when incident on the atoms. A 1" repumper beam of 5 mW is overlapped with the cooling laser before it is separated into six beams.

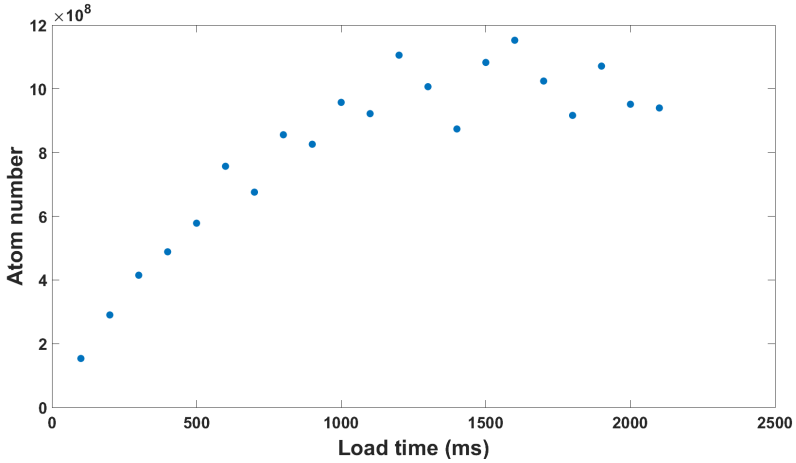

Figure 3.5: Atom number in the 3D MOT as a function of loading time.

All lasers responsible for the 3D MOT are incident for the same time as the 2D MOT and have similar detunings. The magnetic quadrupole field is ramped to 15 $\mathrm{G\,cm^{-1}}$ in 15 ms to provide the gradient responsible for the position-dependent restoring force. The 3D MOT is kept on for 100 ms longer than the 2D MOT. This is to allow any atoms that remained in the push beam to fall down into the 3D MOT beam path and to also ensure that the push beam is not distorting the shape of the 3D MOT before magnetic compression begins. It provides enough time for the 2D gradient field to be turned off, while ensuring that there are no remaining eddy currents from these coils affecting the system.

After 1.1 s of load time, an atom number of 1×10^9 is measured using absorption imaging. After a total load time of 1.5 s the MOT saturates and there is no gain in atom number for any increase in load time (see figure 3.5). A temperature of $\approx 200\,\mu\mathrm{K}$ can be inferred through time-of-flight imaging [138].

3.1.6 Magnetic compression

The cloud of atoms after the MOT stage is just over 1 cm in diameter, which is relatively large when considering the use of one inch cooling beams. This is too large for the efficient loading of the cloud into a crossed optical dipole trap and it needs to be

compressed. This compression is realised through the use of a large quadrupole field. The field is created by the same coils as those used for the 3D MOT. After loading of the 3D MOT is complete, the gradient field is ramped from 15 $\mathrm{G\,cm^{-1}}$ to 30 $\mathrm{G\,cm^{-1}}$ in 100 µs. During this ramp the cooling beam is further red detuned until it is a total of 50 MHz from resonance.

Once a magnetic field gradient of 30 $\mathrm{G\,cm^{-1}}$ is reached, it is maintained for 20 ms. During this compression stage there is negligible loss in atom number and-an order of magnitude decrease in cloud diameter. However this compression does heat the atoms to ≈ 300 µK. The rate of change of the large magnetic field also induces eddy currents in the vacuum chamber. These currents can interfere with sub-Doppler cooling - which require a zero magnetic field to efficiently work. The decay time for the eddy currents was measured to be 30 ms [70]. After compression, the cooling frequencies are detuned in 30 ms to provide enough time for the eddy currents to dissipate while not allowing the cloud to expand greatly.

3.1.7 Sub-Doppler cooling

Sub-Doppler cooling is performed in a two-step process; a 30 ms red-molasses cooling stage is followed by 1.5 ms of grey-molasses cooling. This two-stage process allows for 10^9 atoms to be cooled to 1.7(3) µK in 31.5 ms.

3.1.8 Red-molasses cooling

The beams required for molasses cooling are provided by the lasers which are responsible for the repumper and cooling of the 3D MOT. Following 30 ms of frequency changing and magnetic field decay, the cloud is allowed to undergo a further 30 ms of molasses cooling in a zero B-field. After this time the atom number is measured and time-of-flight imaging is performed to measure the temperature of the cloud. Figure 3.6 shows a typical temperature measurement in two axes for a cloud that has just undertaken red-molasses cooling. The z-axis temperature is measured to be 13.2(9) µK with the x axis

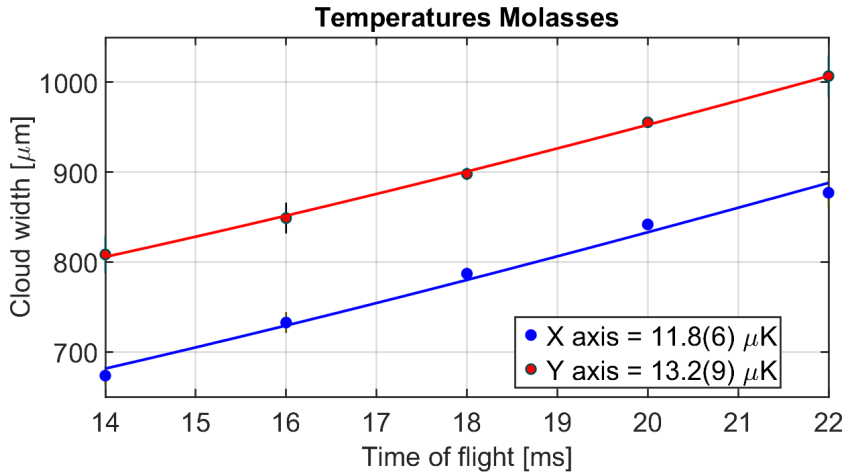

Figure 3.6: Temperature measurement in two axis after 30 ms of red-molasses cooling for a cloud of 1.4×10^9 atoms. A cooling laser detuning of $\sim 6\Gamma$ is applied and a mean measured temperature in both axis of 12.5(8) µK.

being 11.8(6) µK. This is for an atom number of 1.4×10^9. The temperature difference between the two axis is due to a combination of a small difference in the calibration of pixel size between the two axis and a small power difference in the horizontal cooling beams (along the x axis).

Around 5 µK is a typical temperature achievable with red-molasses cooling in cold-atom experiments. However, in our setup we aim to cool the cloud to lower temperatures with larger densities, as a colder, more dense cloud will enable more atoms to be loaded into a crossed optical dipole trap, which will benefit the BEC creation process.

3.1.9 Grey-molasses cooling

Grey-molasses cooling is often used in situations where the hyperfine splitting of an atom is small or there is no cycling transition to benefit from Sisyphus cooling. Grey-molasses cooling only works when there is more than one state in the ground state manifold [139] as there is a requirement to create dark states which the atoms can populate. Spending more of the cycle time in a dark state can in turn increase the phase-space density of the cloud by reducing the average temperature. This method

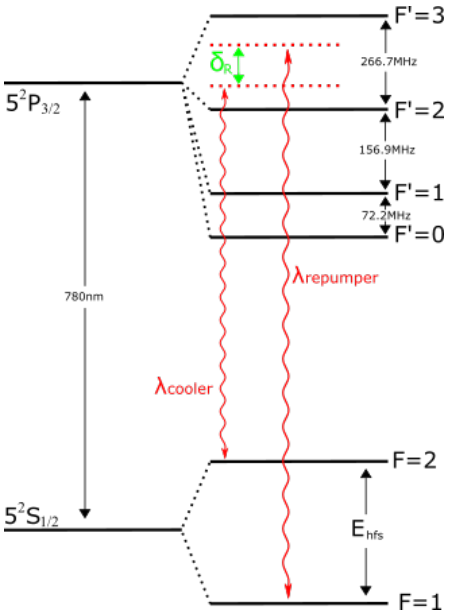

Figure 3.7: Level structure of ^{87}Rb showing the hyperfine structure of the D_2 line with transitions for grey-molasses cooling, adapted from [2]. The energy splitting of the hyperfine ground state is given by E_{hfs}, with the two-photon detuning between the cooling and repumper lasers being δ_R.

can achieve temperatures which are comparable to and even lower than red-molasses cooling [109]. Grey-molasses cooling also provides faster cooling times, of the order 1-3 ms, while still being capable of cooling large clouds of atoms.

The two cooling beams required for grey-molasses cooling are sourced from the same laser. A single beam is passed through a 6.8 GHz phase-modulating electo-optical modulator (EOM, Laser Components NIR-MPX800-LN-10-P-P-FA-FA). The input beam is blue detuned from the $F = 2 \rightarrow F' = 2$ transition (see figure 3.2 for the full level structure). Two frequency sidebands are created, each frequency shifted by $\pm$6.8 GHz from the carrier. This allows us to source both phase-coherent beams from the same laser and have them in the same path. The phase coherence is important for achieving lower temperatures and was experimentally investigated in 2018 by Rosi et al. [109].

The grey-molasses cooling and repumper beams are in the Λ-configuration seen in figure 3.7. The driving frequency for the EOM Δ_{RC}, can be related to the two-photon

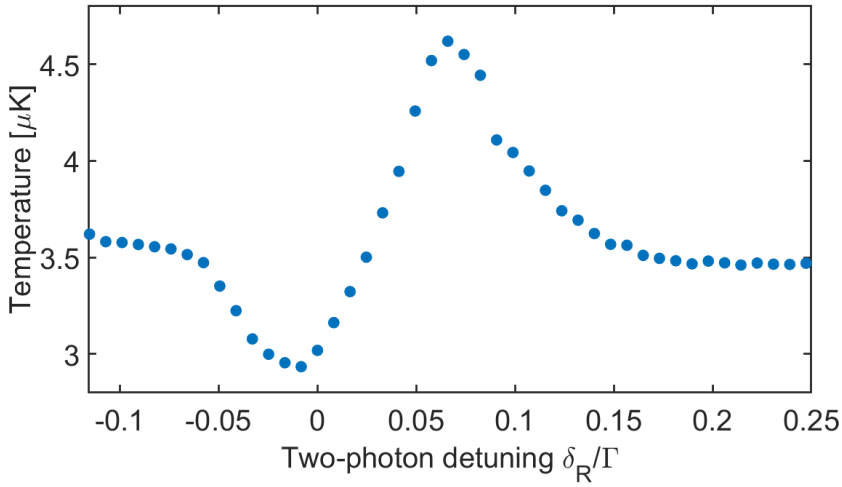

Figure 3.8: Cloud temperature as a function of two-photon detuning for grey-molasses cooling in a Λ-configuration. Data adapted from [70].

detuning δ_R, through [109]

$$\delta_R \equiv \Delta_{RC} + E_{\text{hfs}}/h, \tag{3.2}$$

where E_{hfs} is the ground state hyperfine splitting. The two-photon detuning should equal zero for the lowest achievable temperatures. However as can be seen from the Fano-like profile measured in figure 3.8, the lowest temperature is not reached at $\delta_R = 0$ but instead at $\delta_R = -40$ kHz. A number of experiments have noted the same offset and stated that this was due to a non-perfect cancellation of the stray magnetic fields [109, 140]. However our cancellation of stray magnetic fields results in a residual 2 mG still being present. For a Zeeman shift of 40 kHz, a residual magnetic field of ~ 60 mG is expected. Therefore we suggest that this shift is instead caused by a light shift of the states from the cooling and repumper beams.

Grey molasses relies on the ability to create dark states which the atoms can populate. On the D_2 line with cooler and repumper frequencies blue detuned from the $F = 2 \rightarrow F' = 2$ and $F = 1 \rightarrow F' = 2$ transitions respectively, a dark superposition

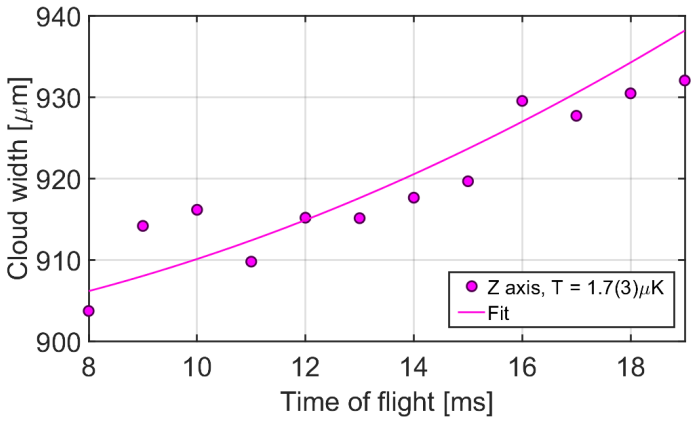

Figure 3.9: Cloud width as a function of time of flight for a cloud cooled by red-grey-molasses cooling, with a two photon detuning of $\delta_R = -40$kHz, a red molasses cooling time of 30 ms and a grey molasses cooling time of 1.5 ms. A temperature of 1.7(3) µK is calculated.

state is created between $F = 1$ and $F = 2$. If the intensity of the cooling beam is larger than the repumper, then the dark state primarily contains atoms which are in the $F = 1$ ground state and is said to be dominated by the $F = 1$ state [109]. Atoms cooled into this state do not experience the varying dipole potential which is responsible for Sisyphus cooling. The atoms remain in the dark state until they motionally couple [107] to a bright state which can then undergo Sisyphus cooling. The lifetime of atoms within the dark state varies with the square of the atom velocity [108]. Therefore, the longer the atoms stay in the dark state, the lower the overall temperature of the cloud, which increases the phase space density. The blue detuning of the light helps aid in the deceleration of the atoms when they are in the bright states. The velocity-selective trapping of the atoms is said to be driven by the Sisyphus cooling process combined with optical pumping to the dark state. In our experiment we have managed to cool 1×10^9 atoms to 1.7(3) µK (see figure 3.9) by utilising an additional 1.5 ms of grey molasses cooling on top of the existing red molasses cooling sequence.

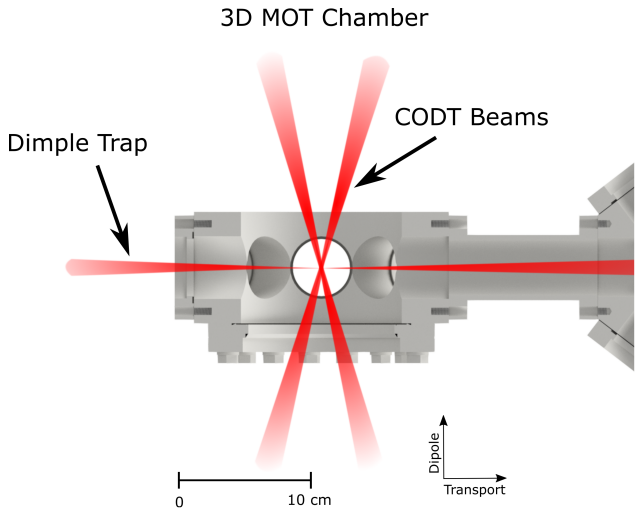

Figure 3.10: A top down view of the 3D MOT chamber with trapping beams for evaporation shown. The dimple trap beam doubles as a transport beam further in the experiment.

3.2 Creation of an all-optical Bose-Einstein Condensate

3.2.1 Crossed optical dipole trap

For the creation of a BEC in the 3D MOT chamber we perform the evaporation all-optically. This method of evaporation often leads to having a greater degree of optical access and without the need for magnetic fields, leads to better control over the residual magnetic field [141]. The one problem however is that the evaporation is performed by reducing the trap power, which in turn reduces the trap frequencies and leads to lower collision rates (see equation 3.4). Therefore, it would be favorable to have a larger starting atom number. To fulfil the goal of having a large atom number for evaporation, a large trapping volume and a large trap depth are required[3]. A large trap depth however can lead to an increase in atom temperature and requires further cooling.

[3]If both of these are met, then a large number of atoms can be initially trapped.

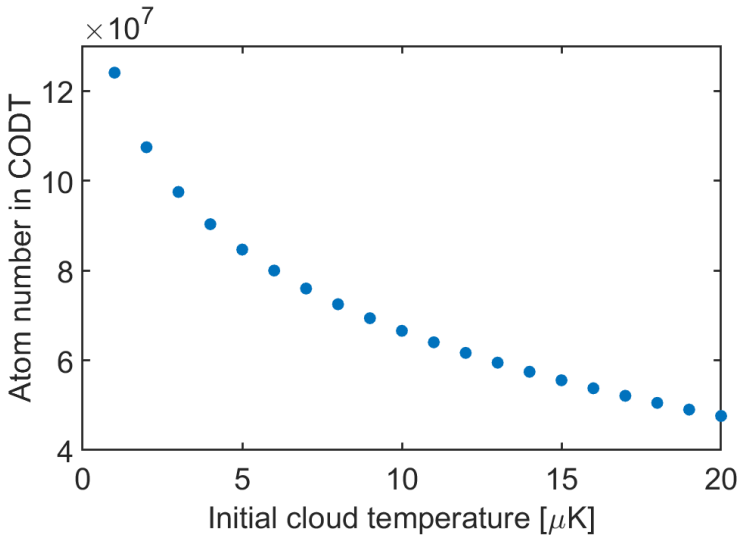

Figure 3.11: Calculation of the total number of atoms loaded into the CODT with varying initial starting temperatures for a cloud of atom number 1×10^9 and 1 mm width.

The lasers we use to create the dipole traps are two 1070 nm, 200W, amplified fibre lasers (IPG YLR-200-LP-WC-Y11). The beams have waists of 425(5) µm and are crossed at an angle of 17(1)°. At maximum power this produces trap frequencies in the vertical, dipole and transport axis of 114(2) Hz, 14(3) Hz and 106(3) Hz, respectively, and a trap depth for the same three axis of 19.2(1) µK, 0.3(1) µK and 16.5(1) µK.

We can calculate the total number of atoms transferred from a MOT into a CODT by comparing the kinetic energy of the atoms with the trapping potential. We first assume a spherical cloud at temperature T, is overlapped with a CODT such that the center of the cloud is at the crossing point of the two CODT beams. Within the overlap of the beams and the cloud, the position-dependent optical dipole potential U_d, is evaluated through,

$$U_d(r,z) = U_d \frac{\omega_0^2}{\omega_0^2(z)} \exp[-2r^2/\omega_0^2(z)] \tag{3.3}$$

where $\omega_o(z) = \omega_0\sqrt{1+(z/z_R)^2}$, characterises the change of the trapping beam waist

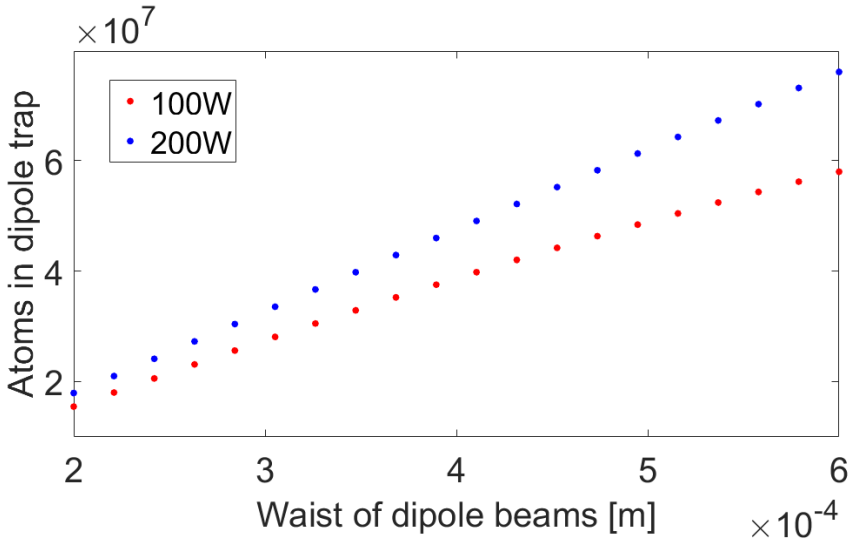

Figure 3.12: Calculation of the total number of atoms loaded into the CODT with varying CODT beam waists for an initial starting cloud of atom number 1×10^9 and width 1 mm at constant temperature.

ω_o, as a function of axial position z from the focus and the Rayleigh length z_R. The maximum trap depth, U_d, can be caculated from equation 2.17. Once a position-dependent optical dipole potential has been evaluated for the CODT beams, a Maxwell-Boltzmann distribution for a cloud of temperature T is calculated. All atoms which have a kinetic energy below the local trap depth can be considered trapped within the CODT [142]. Using this method of simulation, figure 3.11 was produced to show the relationship between starting cloud temperature and the number of atoms in the CODT. For this we start with a cloud of 10^9 atoms at 1.7 µK. The colder the initial cloud the more atoms which can be loaded into the trap. This becomes substantial when you are looking at the typical temperatures that both red and grey molasses can reach in our experiment, 5 µK and 1-2 µK, respectively.

The trapping volume is an important aspect for ensuring a lot of atoms are captured by the trap. Figure 3.12 shows that, the larger the volume, the more atoms can be trapped. This comes with an obvious stipulation: the power of the trapping beams needs to be adjusted to counteract the increase in beam size. If the waist of the beams keeps increasing with constant power, then the optical potential that the

atoms experience becomes shallower. This would lead to a reduction in atom number within the trap through equation 2.19. A "rule-of-thumb" value for the equilibrium temperature of the trap is $\sim 10\%$ of the trap depth. This means that if our trap depth is 300 µK, then we should expect to trap the majority of atoms which have an equilibrium temperature of 30 µK. We also have the possibility of increasing the waists of the CODT beams to 1 mm by removing the focusing lenses in the beam paths. This could theoretically double the atom number in the trap - as seen in figure 3.12.

The CODT beams are ramped on from zero to 100% power in 50 ms. A further 500 ms hold time is implemented after this to allow rethermalisation within the trap. A total of 3×10^7 atoms are routinely captured and their average temperature is 25(1) µK.

3.2.2 Optical Zeeman sub-level pumping

Atoms captured straight from molasses cooling are randomly distributed across both ground states and all Zeeman sub-levels. This is due to the molasses cooling process being undertaken in a null magnetic field. To evaporativly cool a cloud down to create a BEC, one needs all of the atoms to be indistinguishable and in the same state. Evaporative cooling of atoms in the same Zeeman sub-level reduces the number of inelastic collisions between atoms in other Zeeman sub-levels, which reduces the total losses from the trap. To circumvent this, atoms are pumped into a single Zeeman sub-level, $F = 1, m_F = -1$. Before any pumping can be undertaken, a small (0.1 G) magnetic-field offset is applied in the transport direction to set a quantisation axis. This allows us to maintain the atoms in the correct state while ensuring that our circularly polarised pump beams are driving the σ^- transitions.

The pumping is performed in two steps, an optical pumping stage followed by a microwave transfer - this is described in figure 3.13. During the first step two beams are incident on the cloud; a pump beam and a repumping beam. The pump beam is resonant with the $F = 2 \rightarrow F' = 2$ transition and is circularly polarised as to drive

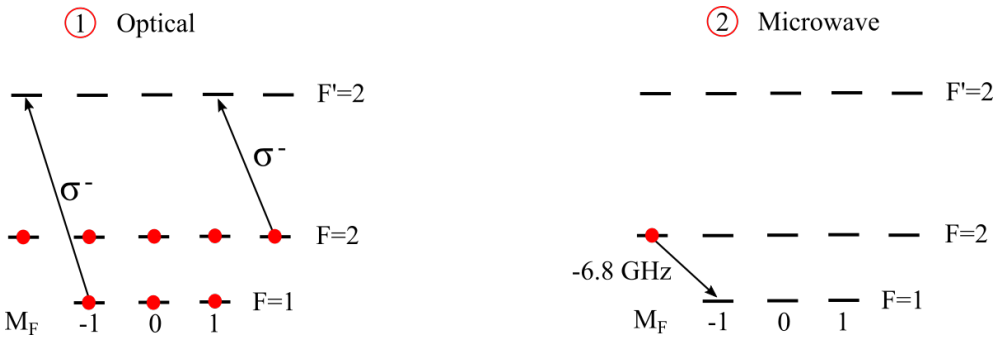

Figure 3.13: The Zeeman sublevels for the hyperfine groundstate of ^{87}Rb and the $F' = 2$ excited state. A two step process is undertaken to transfer the majority of atoms to the $F = 1, m_F = -1$ sub-level. The first step is all optical while the second is done through a rapid adiabatic passage utilising a microwave transition.

a σ^- transition. Atoms populate the $F = 2, m_F = -2$ state, which is dark to the σ^- polarised pump beam. The repumping beam is resonantly driving the $F = 1 \rightarrow F' = 2$, σ^- transition. This combination of beams transfers the population into the $F = 2, m_F = -2$ state in 17 ms. An extra 0.5 ms of repumping beam is allowed to ensure that there are no atoms in the $F = 1$ ground state. This effectively removes all atoms from the ground state with an efficiency of 99.9%.

The second pumping stage is a rapid adiabatic passage using a microwave transition from $F = 2, m_F = -2 \rightarrow F = 1, m_F = -1$. In a 0.1 G offset field, the transition frequency between the $F = 2, m_F = -2$ state and the $F = 1, m_F = -1$ state is Zeeman shifted by 300 kHz. A microwave pulse resonant with the shifted frequency will transfer only the atoms from the $F = 2, m_F = -2$ state to the $F = 1, m_F = -1$ state, with no atoms transferred from any other states. The microwave pulse is 10 ms long with a linear sweep of ± 80 kHz centered -302 kHz away from resonance. The sweep ensures that we transfer the maximum number of atoms to the desired state while being insensitive to noise and magnetic-field inhomogeneities. The frequency sweep is also narrow enough that it does not transfer between other Zeeman sub-levels.

The final stage is a "blow out" pulse, which is resonant with the $F = 2 \rightarrow F' = 3$ transition. This empties the $F = 2$ ground state with 99.9% efficiency but does cause a small proportion of atoms (1%) to decay into the lower ground state. To combat

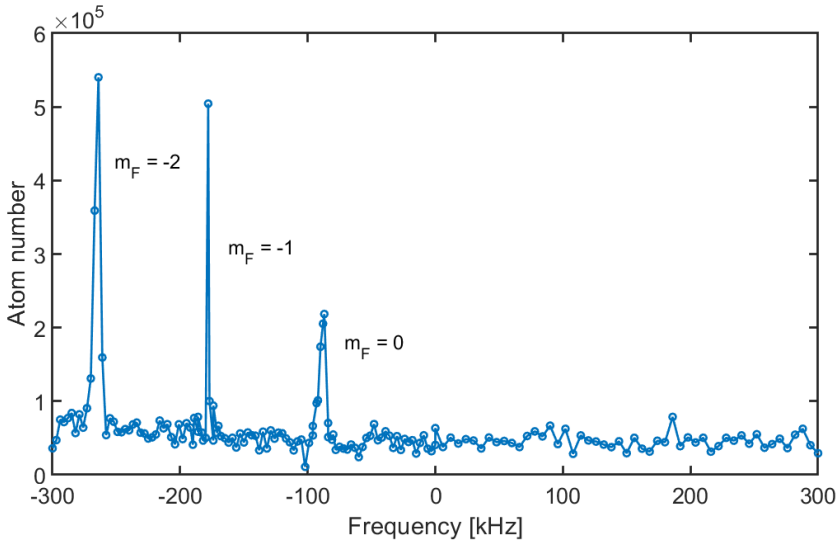

Figure 3.14: Microwave spectroscopy with atoms starting in $F = 1$ $m_F = -1$. Atoms are transferred to the $F = 2$ state with the three available Zeeman sub-levels being represented by each peak on the graph.

this issue, atoms in the desired state are transferred back the $F = 2, m_F = -2$ state and the microwave transfer process is repeated for another cycle, until the atoms are in $F = 1, m_F = -1$ again, with a combined population in all other states of $\ll 1\%$. The population in the desired state is confirmed through microwave spectroscopy as presented in figure 3.14.

3.2.3 Dimple trap

With atoms pumped into the correct state, the next natural step would be to start evaporation. However with just the CODT, the trapping frequency in the transport axis is 14 Hz, with the dipole and vertical axis being 116 Hz and 114 Hz respectively. The trap frequency in the transport axis is too low to efficiently cool a cloud to BEC in a fast time. In order to have a system which has high trap frequencies in all axis, an additional beam can be introduced which increases the trap frequency in the lacking axis (transport axis). This dimple trap can be seen in figure 3.10 and propagates along the transport axis. This beam is tightly focused compared to the CODT beams, with a waist of 47 µm and a Rayleigh length of about 9 mm. It has a maximum power of 25

W and is sourced from a 1064 nm, 50 W, single-mode fibre amplified laser (Azur Light ALS-IR-1064-50-A-CC) which is seeded by a 1 kHz linewidth laser (Coherent Mephisto 1000).

After 300 ms free-evaporation time in the CODT (at 100% power), the dimple trap - with focus in the center of the cloud - is ramped up to 12.5 W in 30 ms. The combined trap frequencies for the three beam trap are 552 Hz, 51 Hz and 561 Hz in the vertical, transport and dipole axis respectfully. These high trap frequencies are important for increasing the phase-space density of the atoms in the trap. Although, even with the dimple trap there is still one axis which is lower in trap frequency, this orientation of trap frequencies allows us to more dynamically control the evaporation ramps and ultimately leads to the creation of a BEC for a large atom number. If one was to evaporate the cloud by reducing the trapping potential, this would also directly reduce the collision rate of atoms in the trap through [128]

$$\gamma_{coll} \propto \frac{N}{\omega^3 T}, \tag{3.4}$$

where ω is the trap frequency. A smaller collision rate and a shallower trap would result in large evaporation times to achieve the required number of elastic collisions to efficiently cool the sample. A dimple trap overcomes this aspect by providing higher trapping frequencies. The increase in phase-space density from the higher trapping frequencies is essential to the production of a fast and large BEC [143]. Before detailing the evaporation process it should be noted that dimple traps can hinder the evaporation process through an increase in two-body and three-body losses. The latter of these become relevant when the density of a sample is $> 2 \times 10^{14}$ cm^{-3} [144]. This is one of the reasons for only using 12.5 W of the total 25 W available to the dimple trap. A maximum atom density of $8 \times 10^{13}\,\mathrm{cm}^{-3}$ was reached with 12.5 W of dimple trap power, while 25 W resulted in $5 \times 10^{14}\,\mathrm{cm}^{-3}$. High trap frequencies are also the reason why one might offset the focus of a dimple trap to increase the effective waist on the atoms. Displacing the focus of the dimple trap so that it is not in the center of the cloud but

instead a few Rayleigh lengths away can benefit the evaporation process. Starting the evaporation with a larger waist and then moving the focus back during the evaporation can provide a workaround for slow all-optical evaporation. This is indeed what we originally did to create a BEC [70]. Currently however, we no longer displace the focus of the beam but instead preform optimised power ramps to ensure we do not enter the three body loss regime.

3.2.4 Condensation through evaporation

The addition of the dimple trap produces a complex potential that the atoms feel. First is the tight central region which is created by the dimple beam and the second is the larger weekly confining region that is created by the CODT beams. If evaporation is not carefully performed, the cloud can become trapped within both potentials - reducing the overall phase-space density of the cloud. This means that atoms that are cold enough to be trapped in the dimple trap, may, after being expelled from the trap due to a collision, still be trapped in the CODT - this includes within the wings of the trap, in a region where the optical potential from the beams is still large enough to trap atoms, but not in the central overlap region of the beams. A calculation of the potential in all three dimensions (with gravity included) for each step of our evaporation is provided in figure 3.15.

The evaporation process is split into four sections; “initial loading”, “pre-evaporation”, “main evaporation one” and “main evaporation two”. Two important quantities to consider at this point are the phase-space density (equation 2.10) and the evaporation efficiency, which is given by

$$\gamma = \frac{ln(PSD'/PSD)}{ln(N/N')}, \tag{3.5}$$

where PSD and N are the phase-space density and atom number before the evaporation step, with PSD' and N' being the phase-space density and atom number after the

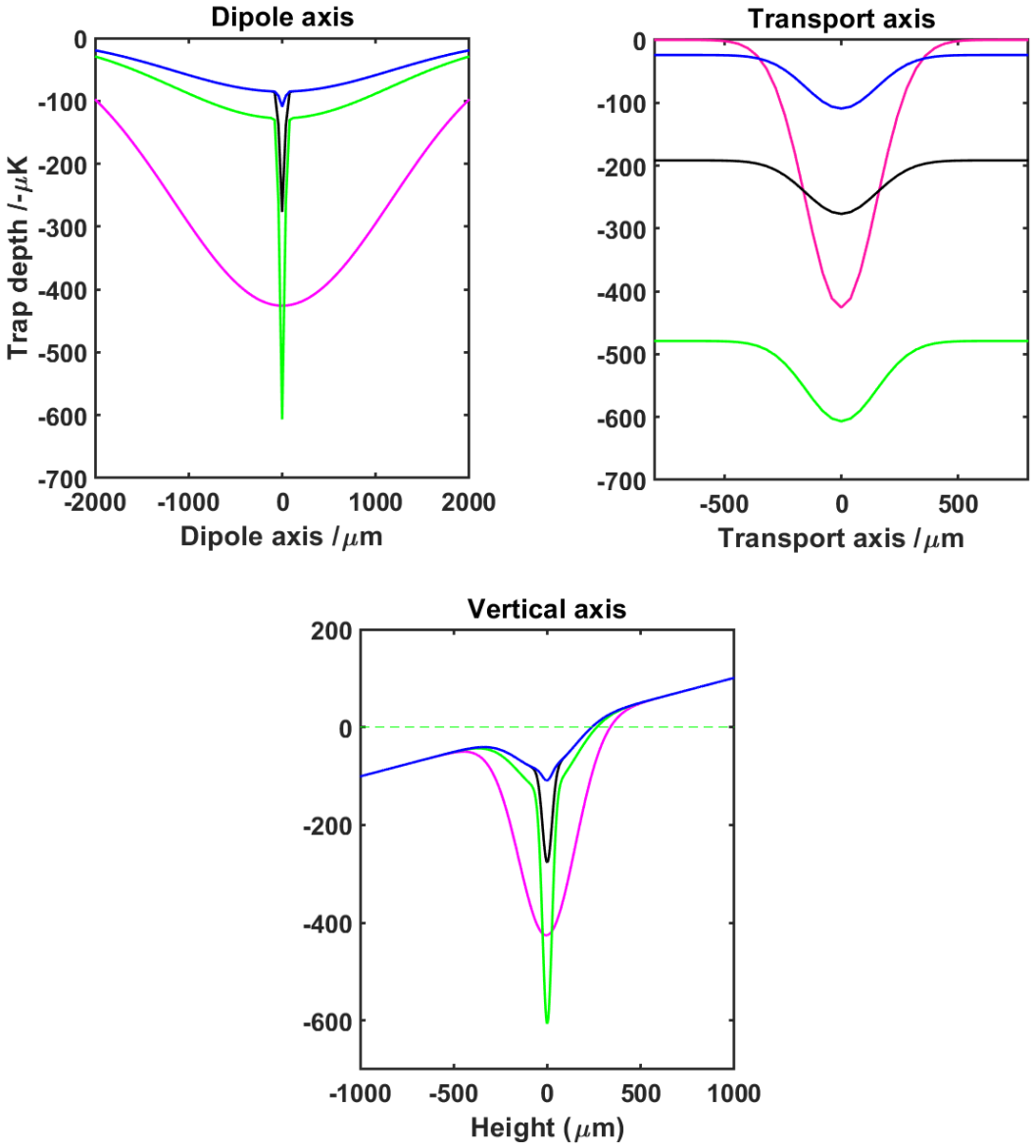

Figure 3.15: Evolution of the trapping potential during evaporation to BEC (gravity included). Pink: Atoms are loaded into the CODT with no dimple trap (initial loading). CODT beams at 200 W. Green: Dimple trap is on and CODT beams have been ramped to a lower power (pre-evaporation). CODT beams at 60 W, dimple trap at 12.5 W. Black: All traps have their powers reduced simultaneously ("main evaporation one"). CODT at 40 W, dimple trap at 0.625 W. Blue: After the final evaporation step, just above transition temperature ("main evaporation two"). CODT at 40 W, dimple trap at 0.25 W.

evaporation step. This can characterise the quality of the evaporation. An excellent number is $\gamma = 3$, which would mean that a gain of three orders of magnitude in phase-space density only resulted in a loss of one order of magnitude in atom number.

The four evaporation steps are provided below with a timing diagram and table of measurables given in figure 3.16:

Initial Loading

This is the stage described at the start of this section. Atoms are trapped within the CODT beams only and are given a free evaporation time. A cloud of $5(1) \times 10^7$ atoms is trapped with a temperature of 25(2) µK with trap frequencies in the vertical, dipole and transport axis of 114(2) Hz, 14(3) Hz and 106(3) Hz respectively, with a phase-space density of $5(2) \times 10^{-5}$. The dimple trap is incident onto the center of the cloud with a power of 12.5 W, which creates a combined trap depth of 606(8) µK. A 800 ms hold time is allowed to the atoms in order for a new thermal equilibrium to be reached.

Pre-Evaporation

After the thermalisation time, the CODT beams are linearly ramped down to 60 W in 400 ms. The dimple trap power is kept constant. An atom number of $1(1) \times 10^7$ is maintained within the cloud with a temperature of 11.7(2) µK. A phase-space density of $1.0(5) \times 10^{-2}$ is measured with larger trap frequencies of 552(4) Hz, 51(2) Hz and 561(3) Hz in the vertical, transport and dipole axis respectively. This provides an evaporation efficiency at this stage of $\gamma = 3.33$, which is very good. This orientation of traps still produces one axis which is lacking in trap frequency compared to the other two. However, this provides us with the dynamic control the trap frequencies in all axis and ultimately provides us with a better quality of evaporation throughout the full evaporation.

"Main Evaporation One"

During this stage, both CODT and dimple beams are ramped down in power. The CODT beams are reduced to 40 W while the dimple trap is reduced to 0.625 W. Both

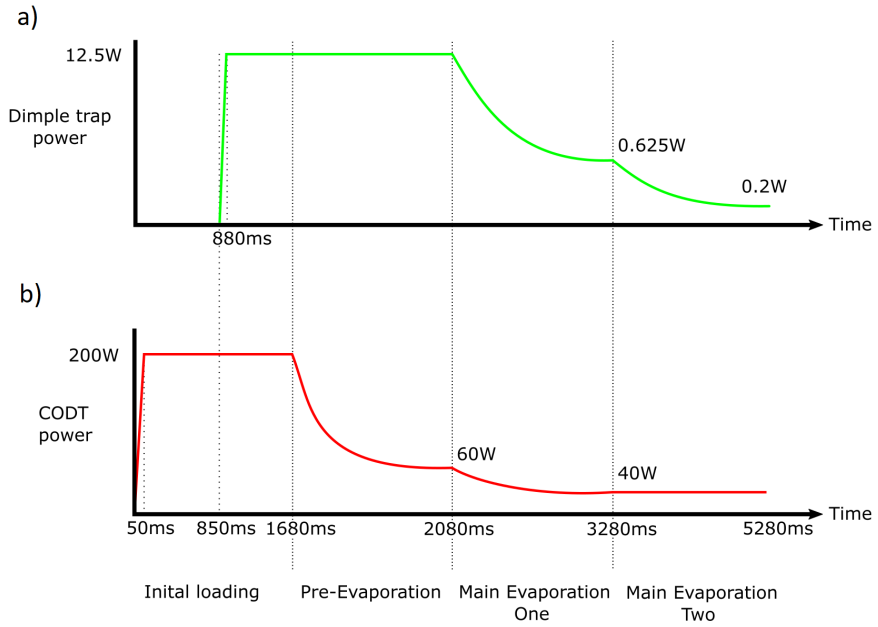

c)

	Initial Loading	Pre-Evaporation	Main Evaporation One	Main Evaporation Two
Dipole trap frequency [Hz]	14(3)	561(3)	366(5)	145(4)
Transport trap frequency [Hz]	106(3)	51(2)	30(2)	30(3)
Vertical trap frequency [Hz]	114(2)	552(4)	377(4)	108(3)
Atom number	$5(1) \times 10^7$	$1(1) \times 10^7$	$5(1) \times 10^6$	$1.0(3) \times 10^6$
Temperature [μK]	25(2)	11.7(2)	4.9(5)	0.45(8)
Phase space density	$5(2) \times 10^{-5}$	$1.0(5) \times 10^{-2}$	$2.0(5) \times 10^{-2}$	0.58
Evaporation efficiency	n/a	3.33	0.95	2.1

Figure 3.16: Timing diagram for evaporation to BEC. a) Dimple trap power. b) CODT trap power. c) Table showing the key values at each stage of evaporation.

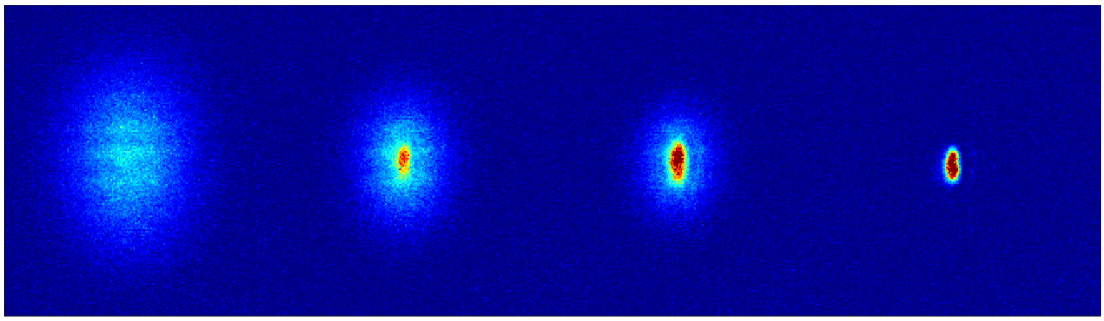

Figure 3.17: Evolution of a thermal cloud to BEC. This corresponds to a selection of final dimple trap powers for the "Main Evaporation Two" stage. Moving from left to right is lower dimple trap powers. Values start at 0.625 W on the far left and moving to 0.25 W, 0.225 W and finally 0.2 W on the far right, where a total atom number of 1.0×10^6 remain.

ramps are now exponential, with a total time of 1200 ms and an exponential time constant of $\tau = 300$ ms for both. The combined trap frequencies in the vertical, transport and dipole axis are 377(4) Hz, 30(2) Hz and 366(5) Hz respectively. After the evaporation there are $5(1) \times 10^6$ atoms trapped at a temperature of 4.9(5) µK. This corresponds to a phase-space density of $2.0(5) \times 10^{-2}$ with $\gamma = 0.95$. This evaporation efficiency is lower than we would expect for these types of ramps and is not efficient. One possible reason for this reduction in evaporation efficiency is the relatively quick evaporation time. We had noticed improvements when this time was increased but no further investigation of this was undertaken. Work to improve this step is currently underway with theoretical simulations being undertaken by a new student to better investigate the evaporation steps in the experiment and optimise them for future iterations.

"Main Evaporation Two"

The final evaporation step is the most crucial, it takes a thermal cloud and brings it to just above the transition temperature[4]. Here the CODT power is kept constant at 40 W while the dimple trap is reduced from 0.625 W to 0.25 W in 2000 ms with an exponential ramp ($\tau = 900$ ms). The measured trapping frequencies after this stage are 108(3) Hz, 30(3) Hz and 145(4) Hz in the vertical, transport and dipole axis respectively. A total of $1.0(3) \times 10^6$ atoms remain in the trap with a phase-space density of 0.58. The temperature of the cloud is 0.45(8) µK, with the critical temperature being caculated from equation 2.7 to be $T_c = 0.350$ µK. The evaporation efficiency is $\gamma = 2.1$. If the power is further reduced from 0.25 W to 0.2 W, a transition of the cloud to BEC is undergone, as can be seen in the far right image of figure 3.17, for a total atom number of 1.0×10^6. This is depicted in the absorption images of figure 3.17.

During the transition of the cloud to a BEC, a bi-modal profile is observed in the absorption images. This is present when there is still a thermal component of the cloud. This thermal region has a Gaussian profile in the atoms' spatial distribution. The condensed region originates from atoms in a single ground state and as such can be described with a Thomas-Fermi distribution. A description of the fit for the bi-modal

[4]The reason for being just above the transition temperature is so we can record useful measurements with the cloud and calculate the relative quantities.

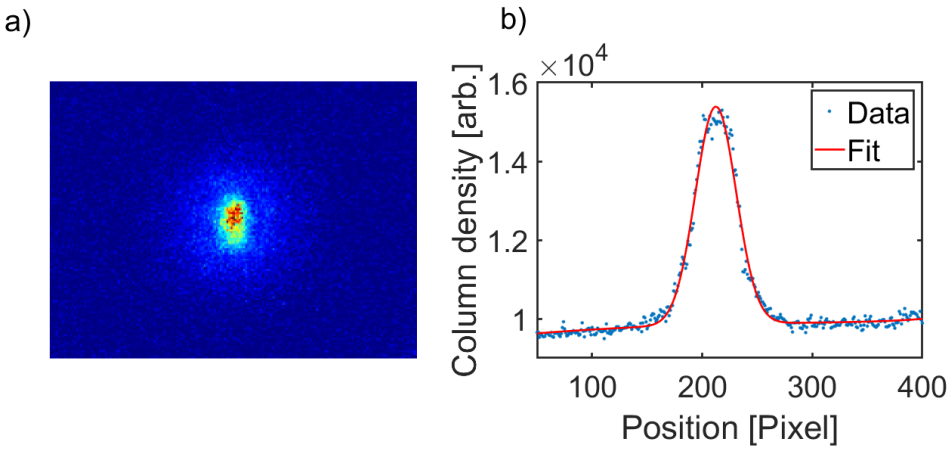

Figure 3.18: a) An absorption image of a BEC of total atom number 7×10^5 with a 40% condensate fraction. b) A column-density plot of a) with a bi-modal fitted function [145] that covers both the thermal and condensate regions of the cloud.

profile used in our fitting software can be found in [145] and it produces profiles as shown in figure 3.18.

A major goal of the experiment is to reduce the cycle time to around 10 s and the fast creation of a BEC helps enable that goal. Although the cycle time for the full evaporation presented here (4 s) is more than 1 s longer than that quoted in [70], we do not see this as a major issue at the moment. A number of additions were implemented (magnetic coils, microscope breadboard, optical lattice configurations) to prepare for future experimental steps and has resulted in an increase of the cycle time, primarily due to the optimisation of magnetic-field parameters and the readjustment of optical beam paths.

The fast creation of a large all optical BEC is a great achievement; however, this was performed in the same chamber that the 3D MOT is created in. There is no room around this section to fit any of the other apparatus that is required for the creation and imaging of a single 2D system of atoms. For this reason, atoms need to be transported

into the science chamber which has greater optical access. After transporting the atoms, the cloud is manipulated such that it populates only a single antinode of the vertical standing wave, which can then be imaged from below.

Chapter 4

Preparation of a 2D system of atoms

A high-resolution microscope capable of imaging single atoms often only has a depth of focus of around 1 µm [39, 45, 65]. Therefore to image a full system in focus, the atoms need to be confined within a single antinode of a standing wave. The selection of atoms in a single antinode is performed by means of a microwave transfer in the presence of a large magnetic gradient (100 G/cm) [45,146]. The antinode is within the focal plane of the objective which can then be imaged by the quantum-gas microscope. Being able to deliver a system capable of creating a 2D system of atoms is one of the goals of my PhD thesis. The following chapter will describe the process from a molasses-cooled cloud to a single antinode of a standing wave which is then imaged with a high-resolution objective. A single antinode containing atoms in a 2D system is referred to as a single layer of atoms.

4.1 Experimental Sequence

The following section will provide a brief description of each experimental step involved in the creation of a 2D system of atoms, with more detail being found in each named section. The beginning of the sequence is identical to the one used for the creation of

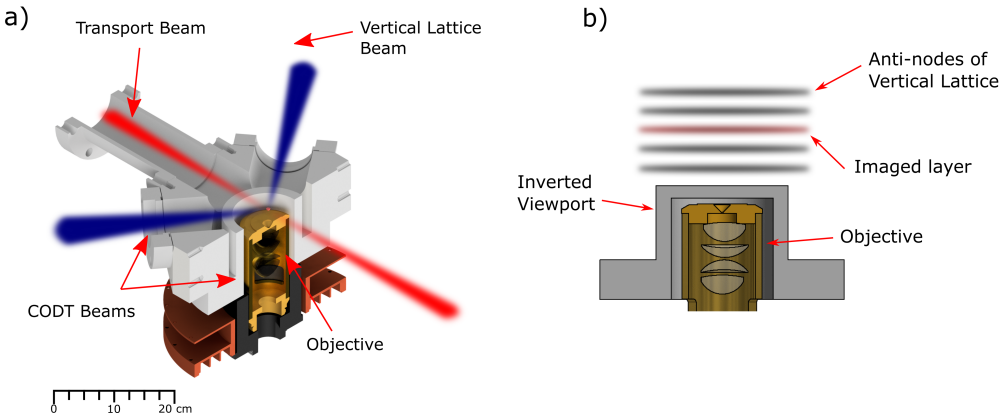

Figure 4.1: a) Cross section of the science chamber, with transport beam, CODT beams and vertical lattice beam. Note that the dipole beam mentioned previously doubles as the transport beam. Atoms are the green dot in the center with the microscope objective below. b) A 3D render of the objective with the antinodes of the vertical lattice (not to scale). Atoms are only contained within a single antinode and their fluorescence light is captured by the objective.

a BEC (section 3.1.2) with the exception that the power of the dimple trap has been set to 20 W when initially incident on the atoms. Therefore the description listed here will begin from after loading atoms into the transport trap.

Section 4.2: Atom transport

When the atoms are trapped in the combined CODT and dimple configuration, an evaporation of just the CODT beams is performed. A mechanical translation stage changes the path length of the dimple trap to transport the atoms between chambers. The moving of the stage is performed after the CODT beams have been disabled. During the move, the magnetic field along the transport axis is maintained by controlling the shim coils of both the science and MOT chambers in the transport axis, to provide a well-defined quantisation axis.

Section 4.2.4: Capture of atoms

After the atoms are transported between chambers, they are recaptured in a crossed optical dipole trap, which consists of the optical lattice beams with retro-reflections blocked. Only after the cloud has been moved over the full distance between the two chambers, are the CODT beams of the science chamber, ramped to full power in order

to recapture the atoms.

Section 4.3: Cooling of the cloud

Optical transport and recapture increases the temperature of the cloud by almost three fold. An evaporation process is required to reduce the temperature of the cloud and increase the phase-space density. Evaporative cooling is performed by reducing the intensity of the CODT beams. This lowers the temperature of the cloud before loading it into the vertical lattice.

Section 4.4.2: Loading of atoms into the vertical lattice

The cloud is transferred into the vertical lattice, which is created by retro-reflecting a laser beam from the bottom vacuum window. The beam is then ramped on and held at constant power for a period of time to allow for rethermalisation of the atoms. After this time, the quantisation axis is rotated by adjusting the currents in the compensation coils of the science chamber, such that it is in line with the vertical axis. The intensity of the CODT beams is then reduced until they are completely off. All of the atoms are then transferred with the aid of a microwave pulse to the $F = 2, m_F = -2$ state. Following this, the vertical lattice power is reduced to allow for atoms not in the layer of interest to be removed.

Section 4.5.1: Creation of a 2D system

A large quadrupole field is turned on. During the ramp-up time of this field, the current in the compensation coils is adjusted to align the center of the quadrupole field parallel with the center of the cloud. Simultaneously, an offset field is applied vertically, shifting the zero point of the quadrupole field below the cloud. For a microwave transition between $F = 2, m_F = -2 \rightarrow F = 1, m_F = -1$, the magnetic gradient from the quadrupole field separates each antinode of the vertical lattice in frequency space [45, 146]. Atoms in a single layer are addressed and all atoms in every other layer are removed from the lattice using a resonant laser pulse. To conclude, the quadrupole and offset fields are both ramped off.

Section 4.6: Cooling to superfluidity

This stage has still to be implemented, although the general idea will still be discussed.

A dimple trap incident on the atoms through the objective can lead to a more efficient evaporation by increasing the collision rates during the evaporation process [45]. This can lead to a faster evaporation and provide a greater level of control over the cooling process.

Section 4.7: 3D optical lattice

The CODT beams, which were originally used to capture the atoms from the optical transport, are retro-reflected onto themselves to create optical lattices and ramped to full power. Simultaneously, the vertical lattice is also ramped to full power. The single layer of atoms is now confined within a 3D optical lattice.

Chapter 5: Imaging and cooling

This section is discussed in detail within chapter 5 but will be briefly described here for completeness.

Atoms in a single layer are detected using fluorescence imaging by means of molasses cooling the cloud in 3D. Retro-reflected beams, red-detuned from the $F = 2 \rightarrow F' = 3$ transition, are incident onto the cloud, in the same direction as the three lattice beams. A repumper beam on the $F = 1 \rightarrow F' = 2$ transition is also incident onto the atoms. This forces the atoms to undergo Sisyphus cooling and emit light isotropically. Some of this light is captured using a high-numerical-aperture objective from below and then imaged on a camera. A more detailed analysis of the imaging process is provided in chapter 5.

All of this sequence has been implemented during my time in the lab, with the exception of the creation of the 2D superfluid. This was left till last as we could optimise the imaging system without a degenerate cloud. Akin to this, the laser system required for the dimple trap that passes through the objective has still yet to be built. Therefore all the data presented within this section is for that of a thermal cloud.

4.2 Atom transport

The dimple trap beam used for evaporative cooling is also used for the transport of atoms between each chamber and will be referred to as the transport trap beam in this context. During transportation we anticipate heating of the cloud through sloshing, intensity fluctuations and pointing instabilities. Therefore, to help ensure we minimise losses, we aim maximise the number of atoms in the transport trap while also initially cooling the cloud into the trap before moving between chambers. To evaporatively cool the cloud, the CODT beams in the MOT chamber are linearly ramped down to 30% of max power in 200 ms. This loads on average 1×10^7 atoms into the transport trap, which now need to be transported to the science chamber. Here we will describe the laser system required to transport the atoms, the characterisation of the movement of the translation stage and how we adjust the magnetic field during transport.

4.2.1 Laser setup for transport

The transport trap originates from a 50 W single mode fibre amplified laser system (Azur Light: ALS-IR-1064-50-A-CC), which has AOMs in the output path such that it is capable of fast switching without the need to turn the full laser system off and on[1]. This is the same beam as the one used for the dimple trap discussed in section 3.2.3. The laser outcoupler delivers 45 W of power[2] with a waist of 1.0(2) mm and is sent through two AOMs to create two separate fibre-coupled outputs (see figure 4.2 for a detailed schematic). A long, folding path length is used here to provide mode cleaning of the output beam from the amplifier. Azur Light recommends that 1.5 m of propagation distance is required to allow for all high frequency modes to be washed out. The beams are coupled into photonic crystal fibres (NKT Photonics LMA-PM-15 with

[1] Numerous elements in the beam path require heating up to an equilibrium temperature before stable output, with an intensity variation of $< 5\%$ can be achieved. Without this, the output power can vary by up to 5%.

[2] Although the fibre amplifier is advertised as a 50 W system, 10% of the power is lost in the sealed power head due to a large optical isolator and some beam shaping optics.

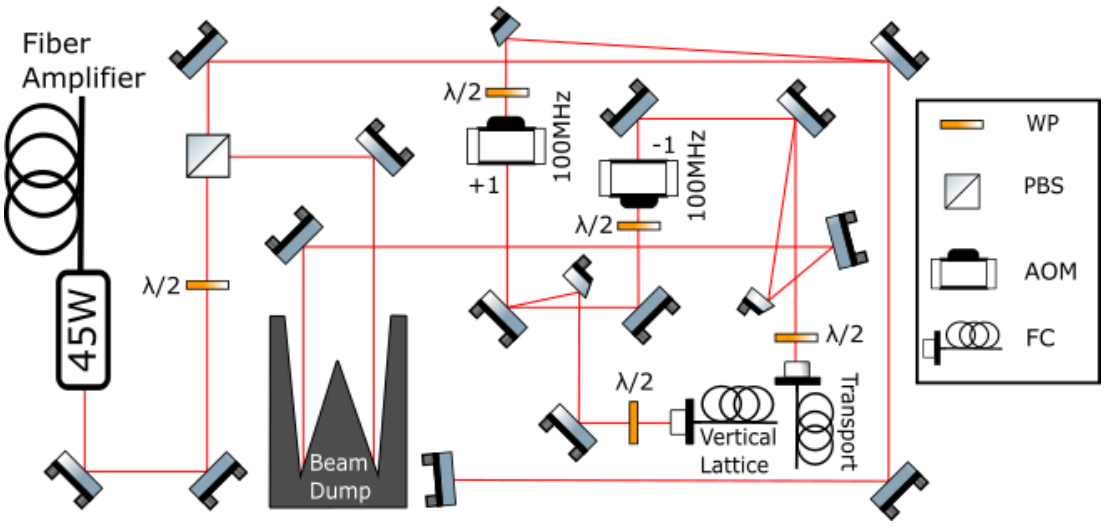

Figure 4.2: Schematic of the optics setup that is used to generate the transport and vertical lattice beams. The elements used are: Waveplate (WP), polarising beam splitter (PBS), acoustic optical modulator (AOM) and fibre couplers (FC) for both transport beam and vertical lattice paths.

high power end-caps and air-gapped FC connectors) that are capable of handling high powers. This cleans the spatial mode of the laser and allows for the safe transportation of high power beams around the optics table.

The lens of the fibre couplers can be a source of trouble when handling high powers. When active, each fibre path has $25-30$ W of incident power on the coupler. We choose a maximum incident time for the maximum power onto the coupler[3] is 5 s. During this time the lens of the coupler can heat up and alter the alignment of the beam into the tip of the fiber. This thermal drift can misalign the fibre coupling to a lower efficiency over longer exposure times. Even with excellent alignment the thermal drifts become a problem, especially if the experiment relies on a stable power for evaporation or trapping of atoms. To counteract the drift, we implement active intensity stabilisation through the use of a PI regulator, which keeps the power after the fibre constant. A logarithmic monitor photodiode (non shown in figure 4.2) on the output of the fibre is connected to the PI regulator which in turn controls the input voltage to the AOM driver and in turn the input RF power to the AOM. This system regulates the power

[3]This time was unfortunately experimentally evaluated and resulted in the accidental destruction of a fibre.

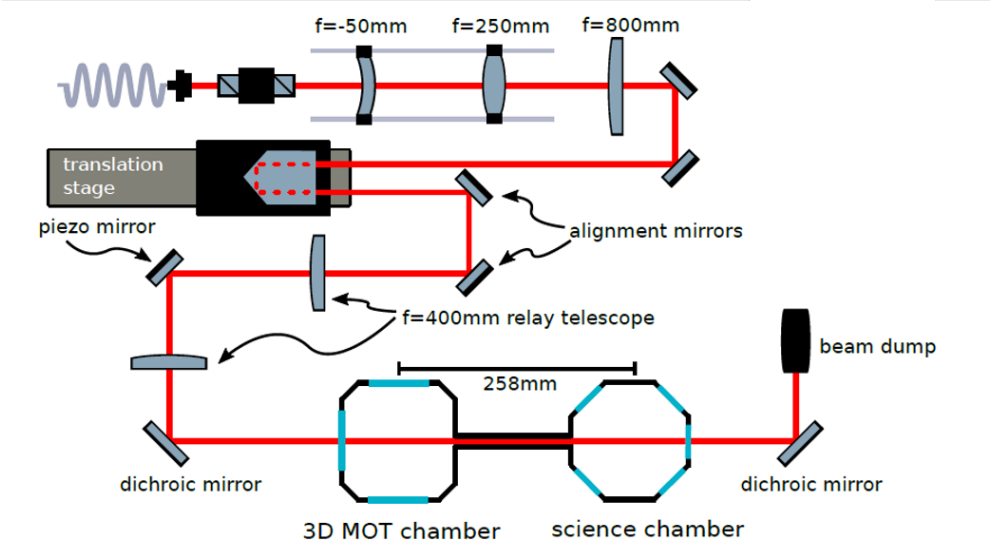

Figure 4.3: Schematic of the transportation setup with translation stage and vacuum chambers shown (not to scale). Taken from [147] with permission from the author.

with a bandwidth of 3.0(1) kHz and ensures that the incident power on the atoms is always the same. The bandwidth is important as it sets the upper limit for how long the power is allowed to drift from its set point before being readjusted. If this time was too long, then a varying intensity of beams can result in a varying AC Stark shift over time and force other light matter interactions to be less efficient. Intensity stabilisation is implemented for all optical lattice beams and the dimple trap beam.

The optical transport beam has its own path on the same setup. We couple about 70% of the 25 W of incident light into the fiber and then transport it one meter to the other side of the optics table (see figure 4.3). The beam exits the fibre with a waist of 1 mm and is expanded to five times this using an expansion telescope. It then passes through the primary $f = 800$ mm focusing lens before being reflected by a corner cube (Thorlabs: PS975M-B) which is mounted to a mechanical translation stage (Thorlabs DDS220/M). The beam is reflected from two alignment mirrors and passes through a set of relay lens before being directed towards the atoms (see figure 4.3).

The mechanical direct drive linear translation stage has a total translatable distance of 220 mm with a maximum translation speed of 300 mm/s and a maximum acceleration

of 5000 mm/s^2, respectively. The total internal reflection corner cube will reflect any input beam out at the same height, as long as the beam is parallel to the center axis of the cube. The translation stage and corner cube are responsible for changing the path length of the light after the focusing lens. This in turn changes the position of the focus.

A mechanical translation stage can cause issues for a cold-atom experiment because the movement of the stage can cause vibrations and the motor inside the stage can produce stray magnetic fields. To try and counteract these effects we place the stage more than a meter away from the chamber and mount it on vibration absorbing pads. This however results in the $f = 800$ mm focusing lens being too far away to focus the light onto the atoms in both chambers.

A set of relay lens allow the focus of the beam to reach the science chamber while still maintaining the quality of the beam. The distance between each chamber is 258 mm and this is also the distance between the two alignment mirrors in figure 4.3. When the translation stage is set to focus the beam inside the 3D MOT chamber, it is also focused on the lower alignment mirror. The relay lenses then invert this position and allows for the beam to be focused in the correct place within the chamber. By adjusting the alignment of these mirrors and by translating the stage a total of 129 mm, the final position of the beam in each chamber can be carefully adjusted. It should be noted that there is a piezo mirror in the beam path; this allows for fine adjustment of the beam location at each chamber. During the sequence this piezo is dynamically adjusted to control the final position of the trap.

4.2.2 Characterisation of translation

The transport stage can introduce unwanted heating of the atoms when moving through pointing-induced heating [148]. This heating arises when the temporal movements coincide with trapping frequencies and result in a heating of the cloud through parametric heating. The movement of the stage is described in terms of pitch, yaw and roll, with

a fourth metric resulting from the rate of change of force on the stage, known as jerk. If one was to think of a beam propagating along the x axis then the pitch of the stage is described as a rotation around the y axis with the yaw being a rotation around the z axis and roll being a rotation around the x axis. However, as a rotation around the x axis would have no effect on a Gaussian beam and its movement along that direction, this has been omitted from the analysis. Each of these displacements can result in a heating of the atoms within the trap. To measure the effect of the pitch and yaw when moving, a quadrant photodiode (Thorlabs: PDQ80A) is inserted into the beam path, 1 m after the translation stage and without any other optics in place. This allows for us to look at the beam's pointing stability as the stage is moving. The data sheet of the translation stage quotes the maximum pitch and yaw to be $\pm$175 µrad. Measured using the quadrant photodiode, we find that the stage has an angular displacement due to the pitch of $\pm$160 µrad with an angular displacement due to the yaw of $\pm$60 µrad. The improvement in the yaw is primarily due to the corner cube, as regardless of the input height of the beam into the cube, it will always reflect the beam out at an identical height, which reduces the overall displacement due to yaw. A comparison of the corner cube to a two-mirror setup was performed and although the displacement due to pitch in both cases was comparable, the displacement due to yaw in the two mirror setup was more akin to the data sheet values.

The quadrant photodiode provides information regarding the pointing stability of the beam during the movement. It does not however provide information on how the stage is moving and if it is displacing with the set parameters. To measure the characteristics of the stage during the motion from one chamber to another, a Michelson interferometer was mounted to the rear of the translation stage. The zero crossings from the interferometer signal can be counted and provides information on the distance traveled by the stage. This data can then be differentiated to the first, second and third order to provide information on the velocity, acceleration and jerk respectively - as shown in figure 4.4.

The total move is performed in 1.4 s, with a maximum velocity of 180 mm/s and a

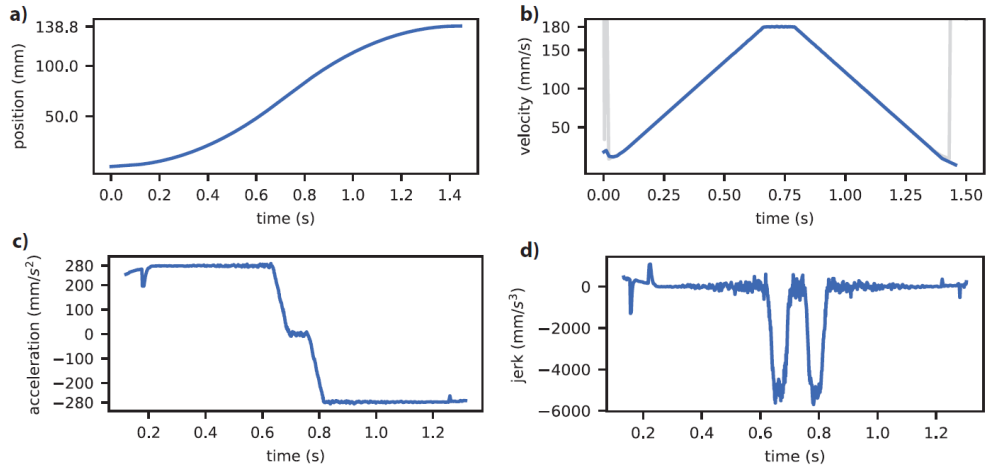

Figure 4.4: A single movement of the mechanical translation stage of 258 mm in 1.4 sshowing: a) Relative position. b) Velocity. c) Acceleration. d) Jerk (start and end points omitted). Adapted from [147].

maximum acceleration of 280 mm/s^2 clearly being reached. The magnitude of the jerk stays below 6000 mm/s^3 which provides sufficiently smooth acceleration and deceleration during transport. The level of noise seen in the jerk measurements are attributed to a measurement artifact due to the limited sampling rate and bit resolution of the oscilloscope used and the resulting errors due to the numerical differentiation. A more detailed analysis of the characterisation of the translation stage and the preceding measurements can be found in the report of Maximilian Ammenwerth, a summer student from the University of Bonn, who worked under my supervision [147].

4.2.3 Moving the atoms

The cloud is transported between each chamber in 1.4 s, with translation stage set parameters: maximum velocity 180 mm/s, maximum acceleration 280 mm/s^2 and maximum jerk of -6000 mm/s^3. The CODT beams are completely turned off as the movement commences. Figure 4.5 shows a top-down view of the vacuum chamber with beams after the atoms are transported to the science chamber.

In order for the atoms to maintain the same Zeeman sub-level during the full trans-

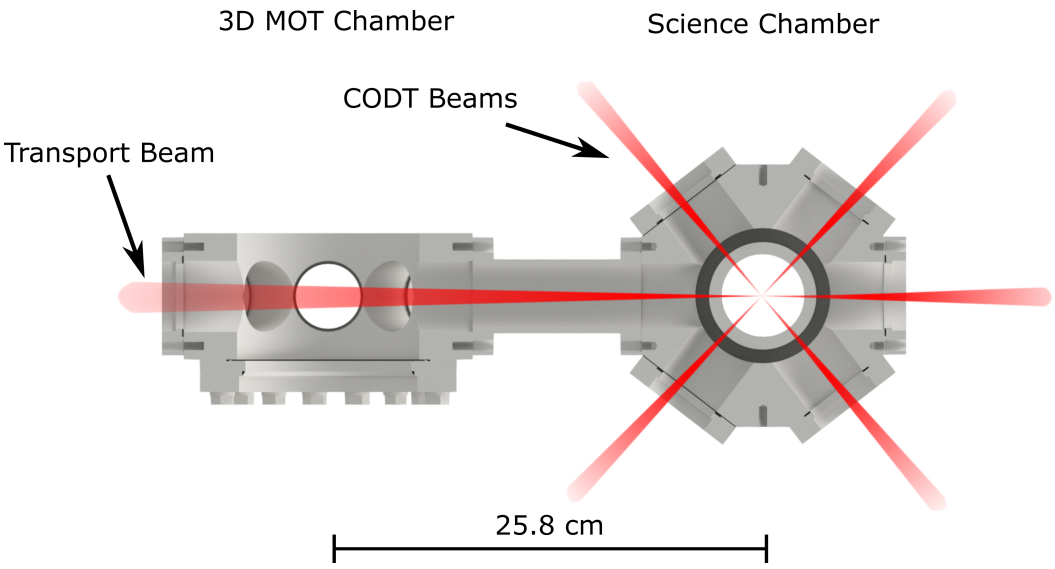

Figure 4.5: Top-down CAD drawing of the science chamber with CODT beams.

port process, a B-field is required along the full displacement of the cloud. This can be quite a tricky task as there are two sets of shim coils that the atoms pass through; one for the 3D MOT chamber and one for the science chamber. During transport of the atoms, the shim fields of both chambers are adjusted simultaneously so that the atoms continuously experience a B-field in the same direction, even if the overall magnitude of the field does change (it never falls below 0.1 G). This allows the atoms to remain in the same Zeeman sub-level and results in fewer sub-level-dependent collisions and an overall reduction in Majorana spin flips. The cloud now does not require another optical pumping and microwave pulses to bring it to the correct state. As well as keeping the atoms in the correct state, a uniform B-field with the same orientation ensures that the cloud does not experience a magnetic field gradient when being transported. The gradient can then exert a force on the atoms in the same direction as the transport, leading to heating of the cloud and losses from the trap.

4.2.4 Capture of atoms

Once atoms have been transported into the science chamber, they are recaptured within a CODT. This trap consists of two 1064 nm beams crossed at 90° in the horizontal plane.

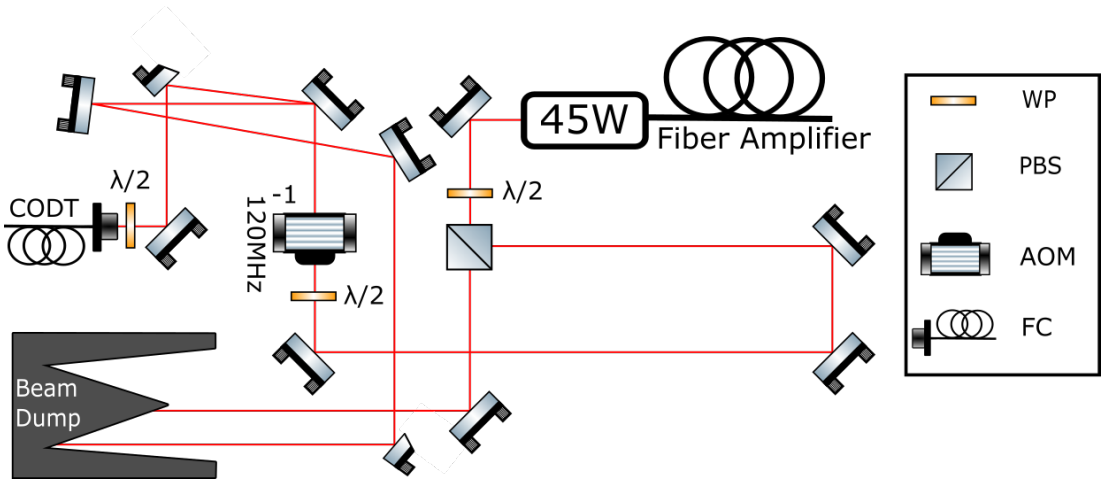

Figure 4.6: Schematic of the optical setup for the CODT beams in the Science chamber. The elements used are: waveplate (WP), polarising beam splitter (PBS), acoustic optical modulator (AOM) and fibre couple (FC) for the CODT beam path.

These beams are each sourced from individual single-mode, fibre-amplified systems, identical to the one used for the transport beam. The beam from each laser is passed through an AOM which controls the output power and allows for fast switching. A schematic of the two identical setups, one for each horizontal lattice, can be seen in figure 4.6.

The beam is coupled into a photonic crystal fibre (identical to the fibres described in section 4.2) and is then directed into the chamber through a number of optical elements. The exact setup is shown in section 4.7, where cooling and the creation of optical lattices are discussed. The two CODT beams are labeled “lattice 1” and “lattice 2”. The “lattice 1” beam has a maximum regulated output power of 23.5 W with a waist of 161(2) µm at the position of the atoms - see figure 4.8 for a parametric heating measurement and the context therein describing how a frequency is measured. The “lattice 2” beam has a similar maximum regulated output power of 22 W with a waist of 163(2) µm. The beams are orientated at an angle of 90° with respect to each other as shown in figure 4.5. The exact position of the transport trap after moving to the science chamber should be at the crossing point of the CODT beams.

After moving the transport trap, the CODT beams in the science chamber are

ramped up to 100% of their available power in 10 ms. This captures on average a total of 3×10^6 atoms at a temperature of 16.2(4) µK, out of a total of 1×10^7 atoms initially loaded into the transport trap. This results in a transport efficiency of 30%. After moving atoms between chambers, the population of atoms in the correct state is checked through microwave spectroscopy. A scan across all sub-levels finds that the population is still in $F = 1, m_F = -1$, with $\ll 1\%$ of the population in all other states.

4.3 Cooling the cloud

In order to increase the phase-space density of the cloud, evaporative cooling is performed before loading atoms into the vertical lattice. The powers of the CODT beams are reduced to 30% in a total of 500 ms, this cools the cloud of 1×10^6 atoms to 1.5(3) µK.

Forced evaporation reduces the temperature of the cloud and increases the phase-space density. The cloud could be cooled more efficiently through the introduction of a dimple trap to assist the forced evaporation after the creation of a single layer (see subsection 6.1). We have the knowledge of two previous iterations of gas microscope experiments within the group - Strathclyde [53] and Munich [26]. Both experimental groups found that a two-step evaporation process that involved a dimple trap incident on a single layer lead to larger phase-space densities in a faster time. Just like when we used a dimple trap to increase the trap frequency for evaporation, it is used in this context to increase trap frequency and overall reduce the area of the lattice in which the atoms can occupy. Combining an evaporation step before layer selection with a magnetic gradient-assisted evaporation of a 2D sheet of atoms contained within in a tight dimple trap provided much larger 2D superfluids - with larger phase-space densities as seen in 6.1.

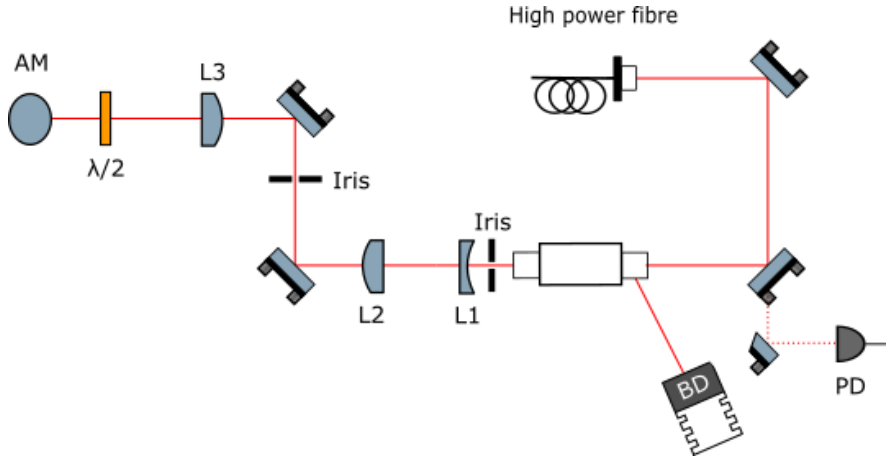

Figure 4.7: Schematic for the vertical lattice beam path. An expansion telescope is made up lenses L1 ($f = -150$ mm) and L2 ($f = 150$ mm). A final focusing lens (L3) of focal length $f = 300$ mm, is positioned before a half waveplate and a 45° angled mirror (AM) reflecting the beam into the plane. As the optics are mounted to a breadboard which is placed above the vacuum chamber, this mirror directs the light downwards to the vertical view port. A beam dump (BD) is responsible for capturing the retro-reflected beam from the isolator with a photodiode (PD) in place for intensity stabilisation.

4.4 Vertical lattice

The vertical lattice is probably the single most crucial laser beam in the experiment. It is responsible for setting the overall position of the cloud and separating the cloud into individual layers. We will begin by describing the optical setup for the vertical lattice, the process of loading a cloud into the beam and the process of rotating the quantisation axis such that it is aligned with the vertical lattice.

4.4.1 Optical setup for vertical lattice

Figure 4.7 shows the optical setup for the vertical lattice. The laser is passed through an optical isolator to ensure that any back reflected light is not fed back into the fibre which could damage it or alternatively pass all the way back into the amplifier. Therefore to align the lattice, we use two irises with a camera focused on each, such

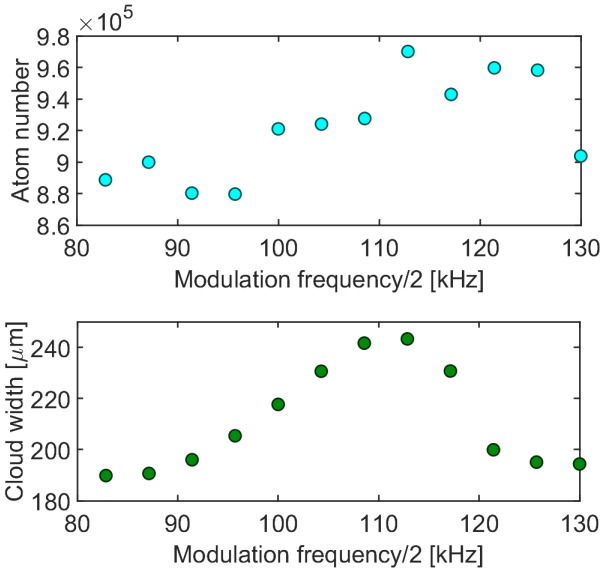

Figure 4.8: Measurement of the axial trap frequency via parametric heating for the vertical lattice, with a power of 3 W in the beam. Top graph shows the atom number for varying modulation frequency with the bottom showing cloud width for the same modulation frequencies. A trap frequency of 115 kHz is measured at half the modulation frequency.

that we can ensure that the beam passes through each iris with the retro-reflected beam not clipping either of the two[4]. An expansion telescope increases the size of the beam which is then focused onto the bottom vacuum window where it is retro-reflected to create a lattice, in a cat-eye configuration.

The axial trapping frequencies were measured using parametric heating of the cloud. This method involves modulating the trapping potential by modulating the intensity of the lattice with different frequencies until the cloud can be seen to heat. This heating happens at twice the trap frequency. Figure 4.8 shows a typical measurement, where, as double the trap frequency is approached, the temperature of the cloud increases while the overall number of atoms stays the same. The power used is this measurement was 3 W (maximum of 15 W available) and a measured frequency peak can be seen at 115(4) kHz. The trapping frequency can be converted into a trap depth through [128]

[4]An alternative way of aligning lattices is to not include an optical isolator and look at the light transmitted back through the fibre. When I worked in Kyoto within the group of Prof. Yoshiro Takahashi for three months, this was the method we used to align the lattices. It works very nicely for low power lattices but starts to feel intimidating when using 20 W.

$$U_t = \frac{M_{\mathrm{Rb}}}{2k_{\mathrm{B}}}\left[\frac{f\pi}{k}\right]^2, \tag{4.1}$$

where M_{Rb} is the mass of a Rubidium atom, f the trap frequency measured and k the wavenumber. A measured frequency of 115(4) kHz corresponds to a trap depth of $U_t = 20(2)$ µK with a waist of 130(3) µm. If this power is increased to the maximum output of 15 W, the trap frequency increases to 445(5) kHz with a trap depth of $U_t = 307(3)$ µK $= 3000E_r$.

The trap depth is an important factor for characterising the lattices. During imaging the cloud is cooled using molasses, which destroys the degeneracy due to scattering and eventual heating. Therefore, the potentials that the atoms see during cooling must be large enough in terms of recoil energy to prevent an atom from escaping the lattice or hopping between sites. In previous work at Munich and Strathclyde [45, 53] trap depths for the optical lattices of $3000E_r$ were used and we obtain similar values.

4.4.2 Loading into the vertical lattice

After a rethermalisation time of 100 ms in the CODT beams, the vertical lattice is ramped on to a power of 15 W in 100 ms. This combined trap now contains $\sim 5 \times 10^5$ atoms. A rotation of the quantisation axis is performed to ensure that it is parallel with the vertical axis and aligned on axis with the quadrupole field used for layer selection.

As long as the cloud does not pass through a region of null magnetic field, the atoms will remain in their current Zeeman sub-level. More strictly speaking, the rate of change of the vector field must be slower than the Larmor frequency in order for the atom's magnetic moment to follow the field adiabatically. In a region of very small magnetic field this results in "Majorana spin flops" [115]. Therefore, to rotate the quantisation axis vertically, the compensation coils in the vertical axis are ramped up to create a magnetic field of 0.1 G in 25 ms. Simultaneously, the compensation coils in the transport axis (which have been responsible for creating the quantisation axis in

the science chamber up till now) are ramped to a zero field value in 50 ms. This overlap in the timings of the two ramps ensures that there is always a well defined quantisation axis.

After the rotation of the quantisation axis, the CODT beams need to be ramped down to a lower power. This is essential for the layer selection process and for allowing the beams to switch from CODT to optical lattice configuration (further discussed in section 4.5). In a total time of 300 ms, the CODT beams are ramped from their maximum available power to their minimum, in a linear ramp. After this ramp the AOMs for each CODT beam are disabled to ensure there is no light incident on the atoms from the horizontal axis[5].

The atom cloud is now transferred into the vertical lattice with all atoms in the $F = 1, m_F = -1$ state. A 3D rendering of the chamber and the beams used for capturing atoms in the CODT beams and then transferring them to vertical lattice is displayed in figure 4.1. At this stage of the experiment, the cloud is contained within multiple antinodes of the vertical lattice with a Gaussian envelope, spread across a total width of 35(1) µm, ~ 70 vertical layers. However, we only need to keep the atoms of a single layer and remove atoms from all others.

4.5 Single-layer selection

Creating a single layer of atoms is not intuitive. The first step is having atoms in well defined layers in the vertical lattice. To address the layers, all atoms are first transferred to $F = 2, m_F = -2$. A large magnetic field gradient then provides a spatial dependence of the Zeeman splitting for a microwave transition between the states $F = 2, m_F = -2$ and $F = 1, m_F = -1$. A microwave pulse resonant on this transition selects a single antinode of the vertical lattice and transfers it to $F = 1$. A laser pulse with well defined circular polarisation is responsible for the removal of atoms in $F = 2$ from all other

[5] A very small portion of light still reaches the atoms from each CODT beam even when the AOM is off. This is due to a leakage of power through the AOM. For 45 W of incident power the leakage is around 1 mW.

layers. This whole process may be repeated to ensure that there are no atoms in any other layer.

The following section will describe the quadrupole field responsible for the creation of the large magnetic field gradient, the steps taken in the preparation of a single layer and the issues that need to be overcome in order to verify and ensure that only a single layer is present. A detailed description of the design of the magnetic coils can be found in appendix A.

4.5.1 Preparing atoms in a single layer

With atoms in the vertical lattice only, the power of the vertical lattice beam is reduced to 1 W ($30E_r$) in 140 ms before the quadrupole field is ramped up. The low trap power ensures that the potential from the other layers is small enough to prevent the recapture of atoms after they have been expelled from the trap using a resonant push out beam. An additional magnetic field is applied vertically to offset the center position of the quadrupole field so that the field lines produced by the quadrupole field are locally flat within the region of the atoms. This is essential for selecting only one layer and will be further discussed in this subsection. The offset field is linearly ramped to 9.5 G in 50 ms. Preceding this, the quadrupole field is linearly ramped to 100 G/cm in 200 ms and then held for a further 150 ms. Shim fields in the transport and dipole axis within the science chamber are now changed in 50 ms to horizontally align the quadrupole field.

The quadrupole coils are driven at 50 A and were designed to produce a magnetic field gradient on the atoms of 100 G/cm, leading to a spatially varying frequency shift of the microwave transition $F = 2, m_F = -2 \rightarrow F = 1, m_F = -1$, of 21 kHz/µm. This has been experimentally measured to be 24 kHz/µm through the use of spatial interrogation of the vertical layers, as presented later in this chapter (see figure 4.13). The transition width for the microwave transition is of the order of 100 Hz. With a lattice spacing of 532 nm, the frequency shift per antinode of the vertical lattice is

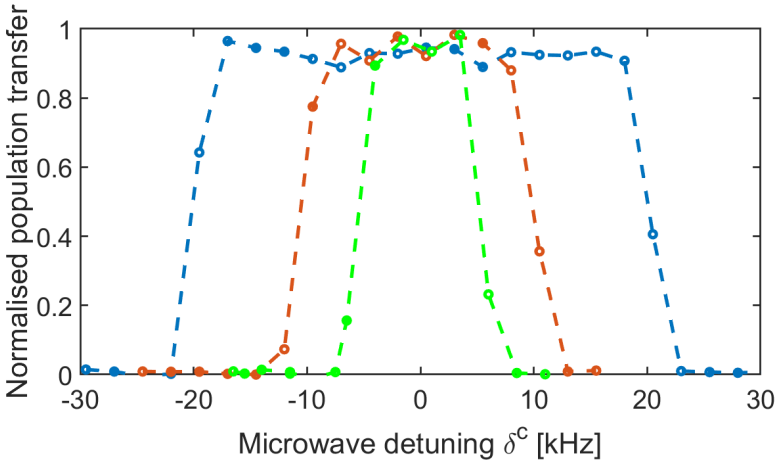

Figure 4.9: Flat-top microwave transfer profiles for a HS1 microwave pulse driving a transition between $F = 2, m_F = -2 \rightarrow F = 1, m_F = -1$ (see equation 4.2). The microwave pulse has a set frequency sweep size of $\delta^c = 10$ kHz (green), 20 kHz (red) and 40 kHz (blue), centred around the resonant frequency for the transition. An applied magnetic offset field of 2 G is used and the addressing is performed with the cloud contained within the vertical lattice only.

around 12 kHz.

All atoms trapped in the vertical lattice start within in the $F = 1, m_F = -1$ state. A full microwave transfer of the cloud to $F = 2, m_F = -2$ is performed in 10 ms without the large quadrupole field. After the gradient and offset field are turned on, hyperbolic secant microwave pulses (HS1) [149] transfers atoms within a single layer to the $F = 1, m_F = -1$ state. The Rabi frequency $\Omega(t)$, and detuning from resonance $\delta(t)$, are varied in time according to:

$$\begin{aligned} \delta(t) &= \frac{\delta^0}{2} \tanh(2t/\tau) + \delta^c, \\ \Omega(t) &= \Omega \operatorname{sech}(2t/\tau), \end{aligned} \tag{4.2}$$

as to drive an adiabatic passage [150]. The critical aspect for ensuring a large transfer efficiency is the correct choice for the frequency sweep width of the pulses, δ^0, and the pulse duration T [146]. The characteristic timescale τ, is adjusted to the pulse duration

with a ratio of $\tau/T = 1/5$ to ensure a smooth switch-on and maintain sharp spectral edges of the flat-top profile [150].

For the microwave transfer of atoms in a single layer, a frequency sweep width of 6 kHz is used with $\tau = 2$ ms and $T = 10$ ms. A peak Rabi frequency of $\Omega = 2\pi \times 5.8(2)\,\mathrm{kHz}$, is modulated with the same τ. Figure 4.9 shows a flat-top transfer profile in a magnetic offset field for different frequency sweep widths. This shows that we are able to transfer atoms uniformly from multiple layers (> 12 kHz) down to a single layer (12 kHz). The flat-top transfer profile ensures that we transfer the majority ($> 95\%$) of the atoms within the particular frequency range to the desired state. This is essential for maintaining high atom transfer rates while ensuring that no atoms are transferred from neighbouring layers. HS1 pulses are also less sensitive to frequency drifts or transition frequency fluctuations. In our experiment, the lowest frequency sweep width for which a flat top profile was still visible was 4 kHz. This is not shown in figure 4.9 due to the resolution required to present the the other three widths.

We use HS1 pulses to transfer atoms within a single layer in $F = 2$ to the lower hyperfine ground state ($F = 1$). After transfer, the remaining atoms need to be removed from the trap. To preform the removal, a "push-out" beam with circular polarisation is incident on the cloud (along the vertical quantisation axis), as to resonantly drive a σ^- transition on $F = 2 \rightarrow F' = 3$. Atoms in the $F = 2$ state are forced to cycle on this transition, which causes them to gain momentum and eventually be too hot to be trapped by the lattice. This process removes $> 99\%$ of atoms in the $F = 2$ state from the trap. Some atoms however, transition back into the $F = 1$ ground state. To overcome this, the process of transferring the full cloud to the $F = 2$ hyperfine ground state and then transferring just a single layer to $F = 1$ is repeated.

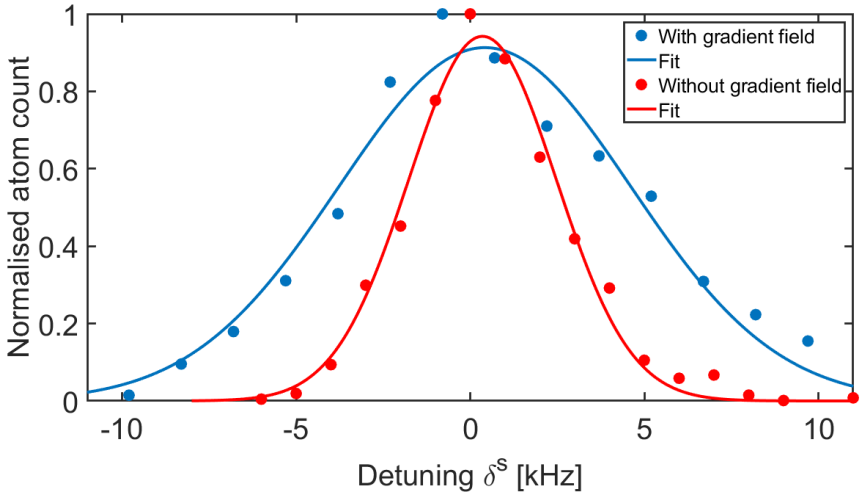

Figure 4.10: Microwave transfer probability as a function of detuning δ^s from $F = 1, m_F = -1 \rightarrow F = 2, m_F = -2$. Square pulses with constant power and short duration's (2 ms), were used to drive the population between states. Data is taken with (blue) and without (red) an external offset field of 10 G. The width of the fit with and without the offset field is 8.9 kHz and 4.4 kHz respectively.

4.5.2 Verifying single-layer selection

Our imaging system has a depth of focus of ≈ 1 µm, so at any one time we could be imaging three layers in focus and be unable to tell the difference between them. There is however a method of verifying that a single layer is created using fluorescence imaging. Using a frequency sweep of less than 10 kHz and by scanning the central frequency of the microwave pulse, one can probe spatially the layers of the vertical lattice and see regions with and without atoms. This will create a profile that looks sinusoidal, akin to the structure of the lattice.

Our first few attempts to see this feature were unsuccessful and troubleshooting the reason was a multi-week process. The reason this took such a length of time, was mostly because when taking fluorescence images, we could see a full cloud of atoms in the optical lattice, which were in focus. As the images were fully in focus we knew there must be a maximum of three layers occupied, as the depth of focus of the objective was 1 µm. Therefore, we found it pretty tough to work out where the issue was coming

from as there was no typical signs of issues. Our initial thought was that fluctuations and instabilities of the current flowing in one magnetic coil was producing an unstable magnetic field. We used microwave spectroscopy on the $F = 2, m_F = -2 \rightarrow F = 1, m_F = -1$ transition to probe the stability of each magnetic field of the science chamber by looking at the width of the measured spectroscopy peak. A magnetic field instability of ~ 3 mG would result in a broadening of the spectral width of the microwave transfer profile to 6 kHz. This could then result in atoms being transferred from different antinodes of the optical lattice when we would expect there to be none. We found that fluctuations of current in the compensation coils resulted in producing a spectral width of around 4.5 kHz (red in figure 4.10). This was the same width for when the offset field was used and was identical to the situation when no coils were on. To test the current instabilities of the quadrupole coils, they were wired in Helmholtz configuration and set to produce a magnetic field of 10 G. This produced a broadened spectral width of around 9 kHz when performing microwave spectroscopy (blue in figure 4.10), which corresponded to an external residual magnetic field gradient across the system of $\sim 5\,\mathrm{mG}$.

As well as measuring a broadening of the spectrum, we also found that the central frequency for all transitions was shifting by about $2 - 5$ kHz. To ensure a stable transition frequency we implemented two changes. First, an idle sequence is initiated to run in the background when the actual sequence is not running. This idle sequence has only the magnetic coils on for the same time as the running sequence. This allows for the coils to reach an equilibrium temperature after roughly 45 minutes. The second change was to add a 50 Hz AC line trigger. This trigger syncs the microwave pulses for layer selection to the 50 Hz power line. All microwave pulses can therefore be sent in phase with the power line, which when measuring the the spectral width of a microwave transition ($F = 2, m_F = -2 \rightarrow F = 1, m_F = -1$), with an incident 10 G magnetic field created by the quadruple coils in Helmholtz configuration, reduces the overall broadening of the peak. The spectral width of the peak without the line trigger was measured to be 9 kHz and was reduced to around 4 kHz with the line trigger.

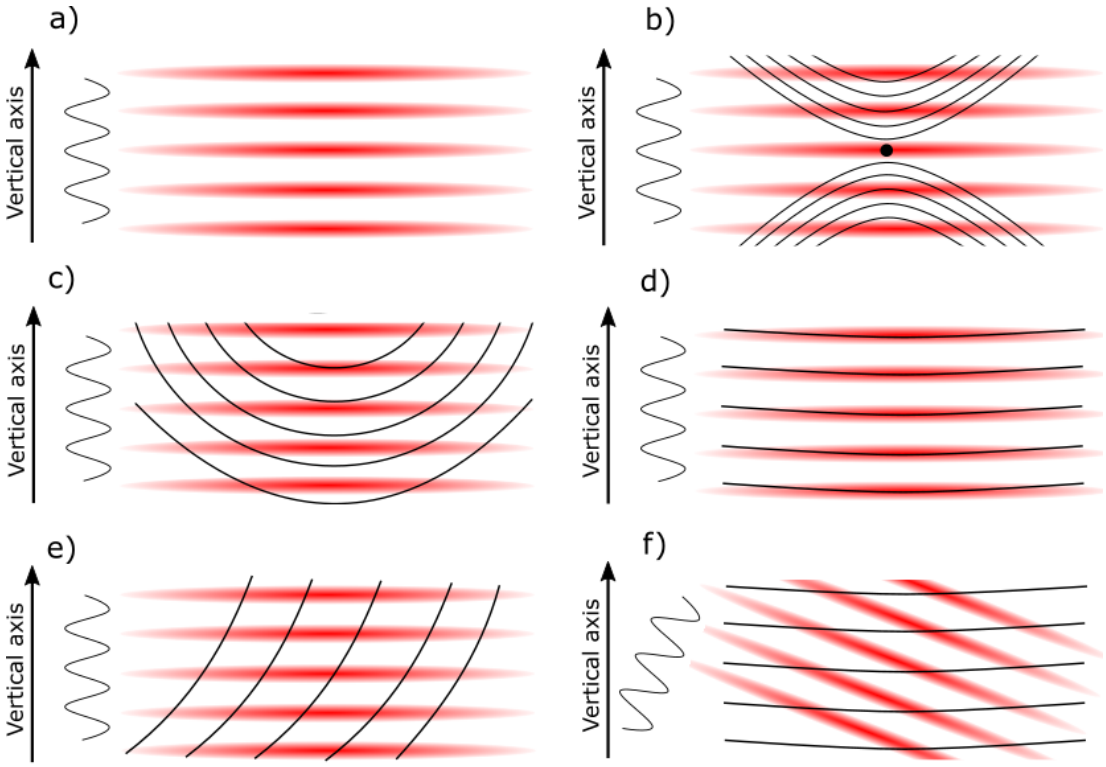

Figure 4.11: Multiple configurations in which a quadrupole field created by two coils can be aligned with respect to atoms in a 1D optical lattice. a) Atoms (red) are in a lattice which is aligned with the vertical axis and no quadrupole field is present. b) The center of a quadrupole field is incident on a single antinode of the optical lattice. The black lines represent the field lines of the quadrupole field. c) An offset field has been applied in combination with the quadrupole field to displace the quadrupole center. d) The value of the offset field has been increased further such that the field lines now look locally flat within the region of the atoms and parallel with each antinode of the lattice. e) The quadrupole field has been offset with a similar field to that of d) but has also been displaced horizontally by an external field. f) An offset field similar to d) has been applied to the system. The optical lattice is not aligned with the vertical axis and as such the field lines cut through multiple lattice layers.

Even with these new changes we could not see the sinusoidal profile that we expected. There are a number of scenarios where the quadrupole field for layer selection could itself cause the transfer of more than one layer. Figure 4.11 shows the most common situations for a large quadrupole field superimposed with a trapped cloud in a 1D optical lattice. When the quadrupole field center is incident on a single antinode of the optical lattice, the surface of the magnetic potential is extremely curved due to them being close to the center of the field (b) of figure 4.11) - with regions of equipotential following a curved path. An offset field can be applied vertically to displace the center of the quadrupole field perpendicular to the antinodes of the optical lattice (d) of figure 4.11). However, if the offsetting of the quadrupole field is not large enough then the magnetic field lines produced are no longer locally flat at the antinodes of the lattice (c) of figure 4.11). An external magnetic field can also displace the quadrupole field horizontally (e) of figure 4.11) and result in the field lines becoming more aligned with the vertical axis.

To better evaluate the orientation of the field lines produced by the quadrupole field, the layer selection process can be repeated but instead of completely turning off the CODT beams, they are changed into optical lattice configuration (see section 4.7) and kept at $\sim 100E_r$. This prevents the atoms from moving around the optical lattice during the layer selection and enables a way of visualising the magnetic field gradient [45, 146].

Taking fluorescence images of the atoms after holding them in the 3D optical lattice during layer selection provides the images seen in figure 4.12. By adjusting the position of the gradient field center so it lies directly below the atoms but aligned with the vertical axis and by changing either the dipole or transport shim fields by up to 1 G (moving the location of the centre of the field), multiple layers can be addressed and a rotation of the addressed layers can be seen. This rotation comes from a shifting of the gradient field centre and a change of curvature of the field lines passing through the lattice. In figure 4.12 layer selection when no additional compensation field has been applied (left-most images) shows discrete lines of atoms across the image. Each

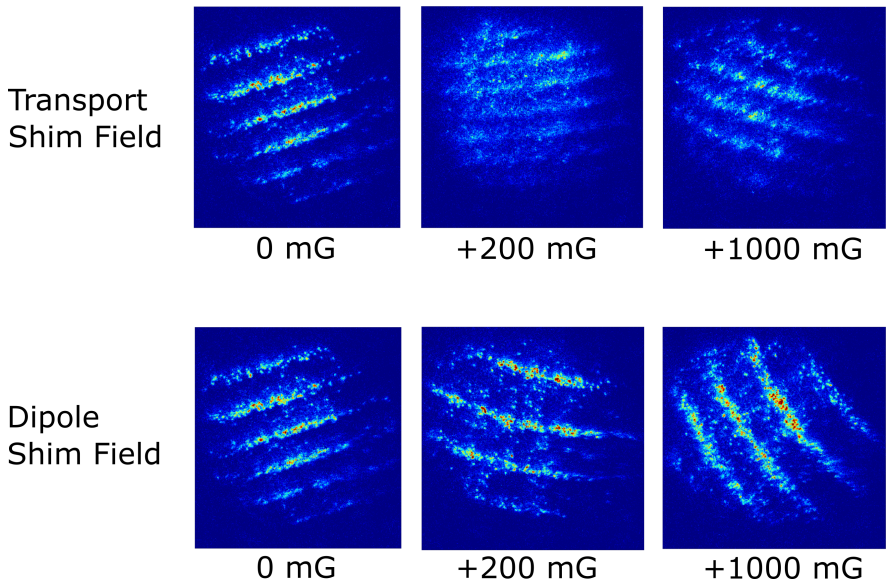

Figure 4.12: Top down fluorescence images of multiple layers being addressed. Each strip of atoms corresponds to regions in different layers which experience same magnetic field and are therefore resonant with the microwave pulse. The left hand most image is taken with no additional compensation field and the shim fields are adjusted as to see a rotation of the layers addressed.

line of atoms is a separate vertical lattice layer that has been addressed. The fact that multiple layers are being transferred indicates that the quadrupole field is in a configuration akin to either c), e) or f) from figure 4.11. The center of the quadrupole field is not initially aligned with the centre of the cloud due to mechanical tolerances of the coils and their mounts to the chamber (± 1 mm). To move the centre position, the horizontal shim fields in the science chamber can be adjusted. In figure 4.12 both dipole and transport shim fields are varied independently. If the centre of the gradient field is not offset from the atoms by a large enough distance, then the curvature of the gradient is significant enough that it can cut through multiple vertical layers of atoms. This results in florescence images which contain stripes of atoms. Each stripe represents a separate layer of atoms which experienced the same magnetic field. The selected regions appear thin, which would suggest that the field lines are still particularly curved in this region. However a positive sign is that the number of layers selected can be reduced by increasing the magnitude of the offset applied with the transport shim field. This means that there are two issues with the layer selection: the field lines from the gradient

are locally curved and there is an external offset which needs to be compensated.

To counteract the local curvature of the field lines, an additional 0.5 G offset is applied vertically to further displace the center of the quadrupole field. In combination with this, the external offset which could not be compensated by the science chamber shim fields[6] is counteracted by using the 3D MOT gradient field. This has reduced the number of layers visible to just a single one, which no longer appears as a strip of atoms but instead a round region.

Figure 4.13 shows the fluorescence counts while scanning the central microwave frequency during layer selection, using a frequency sweep of 8 kHz. As can be seen in figure 4.13(a), as the frequency passes through regions where there are no atoms, none get transferred. By varying the central frequency of the microwave pulse and monitoring the fluorescence from the atoms, the plot in figure 4.13(b) can be recorded. Here the sinusoidal feature of the optical lattice is clearly visible. Fitting a sine wave to this data, the separation between optical lattice layers in frequency space is measured to be 12(1) kHz. This is slightly larger than the caculated value of 10.5 kHz from section 4.5.1 and a larger separation is more beneficial, as it allows for single layer selection and transfer to be more forgiving to current instabilities in the magnetic coils. This results in a larger frequency region in which atoms from a single layer will still be transferred.

4.6 Cooling to superfluidity

Previously, we have created a BEC via all-optical methods [70]. Historically this was one of the ways to achieve a fast cycle time while requiring fewer magnetic coils. Presently however; this is often combined with an external quadrupole field to provide an increase in the phase-space density of a cloud. This results in fast creation of a high atom number BEC. This method involves vertically offsetting a large quadrupole field from the center

[6] This was a technical limitation provided by the power supplies used for the shim fields in the science chamber. They would not allow a current of > 4 A due to built in safety restrictions.

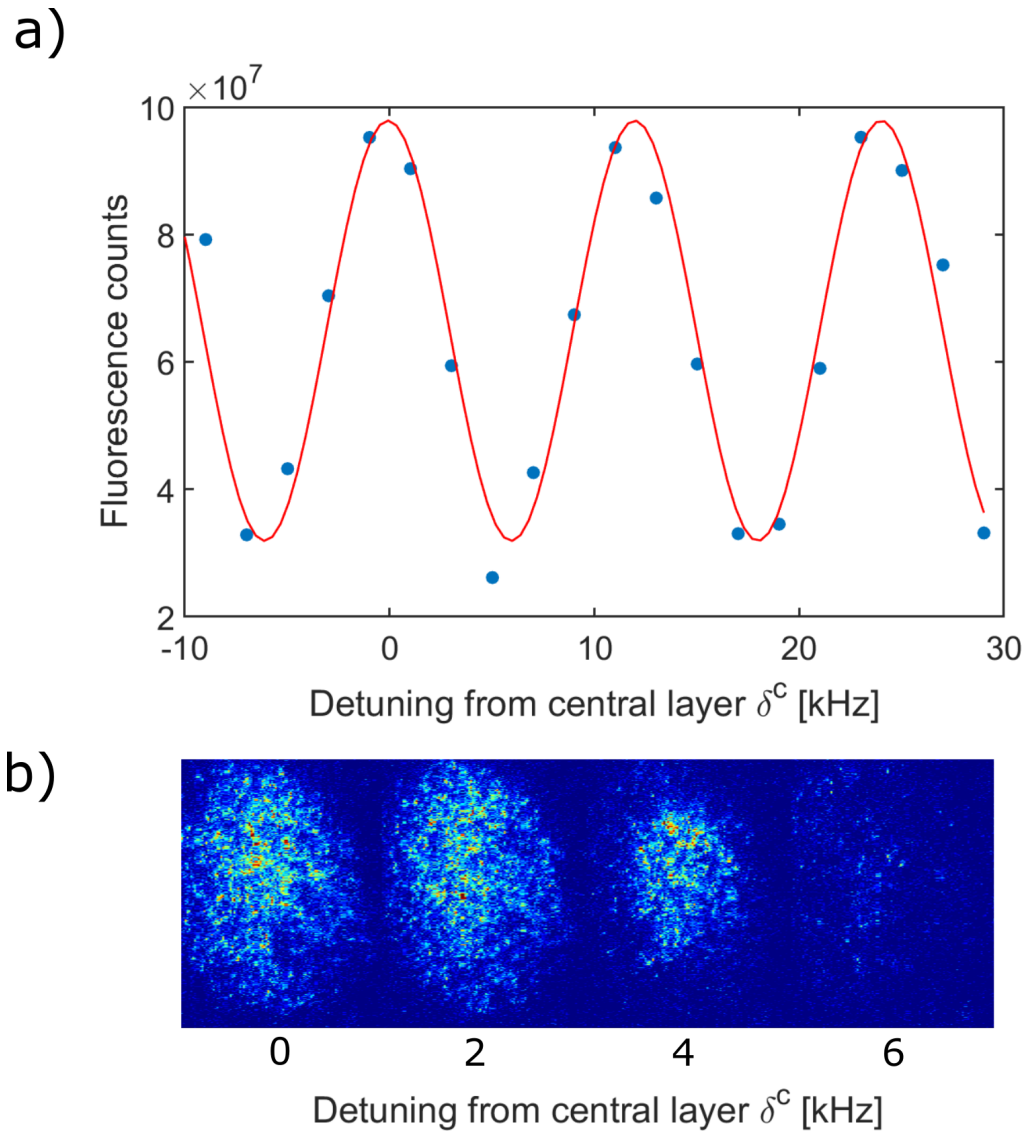

Figure 4.13: Single layer selection. a) Number of fluorescence counts when varying the central frequency δ^c, of a HS1 microwave pulse driving the $F = 2, m_F = -2 \rightarrow F = 1, m_F = -1$ transition, using a frequency sweep of width 6 kHz. A sine wave is fit to the data yielding a frequency of 12(1) kHz. b) Fluorescence images for different central frequencies of the microwave pulse away from resonance ($\delta^c = 0$).

of the cloud, allowing for the trapping potentials in the vertical axis to be lower. A uniform ramp of the gradient produced by the quadrupole field can lead to the hotter atoms escaping the trap, leaving only the cooler ones behind.

However, the trap depth provided by the vertical lattice beam at $30E_r$ are already pretty low (< 50 µK) due to the large waist of 130(3) µm and will only decrease further as the power is reduced for evaporation. A dimple trap can be implemented to provide larger trap depths and in turn larger trapping frequencies which can provide a greater level of control over the evaporation - analogous to what is described in section 3.2.3. The dimple trap in this case will propagate through the objective onto a single layer and result in a more efficient cooling process. This has yet to be implemented into our system, but the enhancement of cooling due the dimple trap in a similar system is described in detail within [3], with an overview for the implementation of such a system into this experiment being detailed in section 6.1.

4.7 Optical lattices

Once atoms have been prepared in a single layer, they need to be contained within a 3D optical lattice. The CODT beams used for the initial trapping of atoms in the science chamber can now be retro-reflected onto themselves to produce optical lattices in the horizontal directions. The optics responsible for the lattices are mounted on two identical breadboards positioned on opposite sides of the vacuum chamber. These breadboards contain not just the optics for creating the lattices but also those for cooling the cloud during fluorescence imaging with molasses and for absorption imaging.

The optical lattice beam is the red path in figure 4.14 and is delivered to the setup through a photonic crystal fibre (identical to the fibres described in section 4.2). The powers of all lattice beams are regulated to ensure constant lattice depths during all stages of the experiment. We actively stabilise the power of the lattice using a logarithmic photodiode which utilises light from a transmission through a mirror. The beam is focused down onto the atoms with a $f = 300$ mm lens (F1) to have a waist of

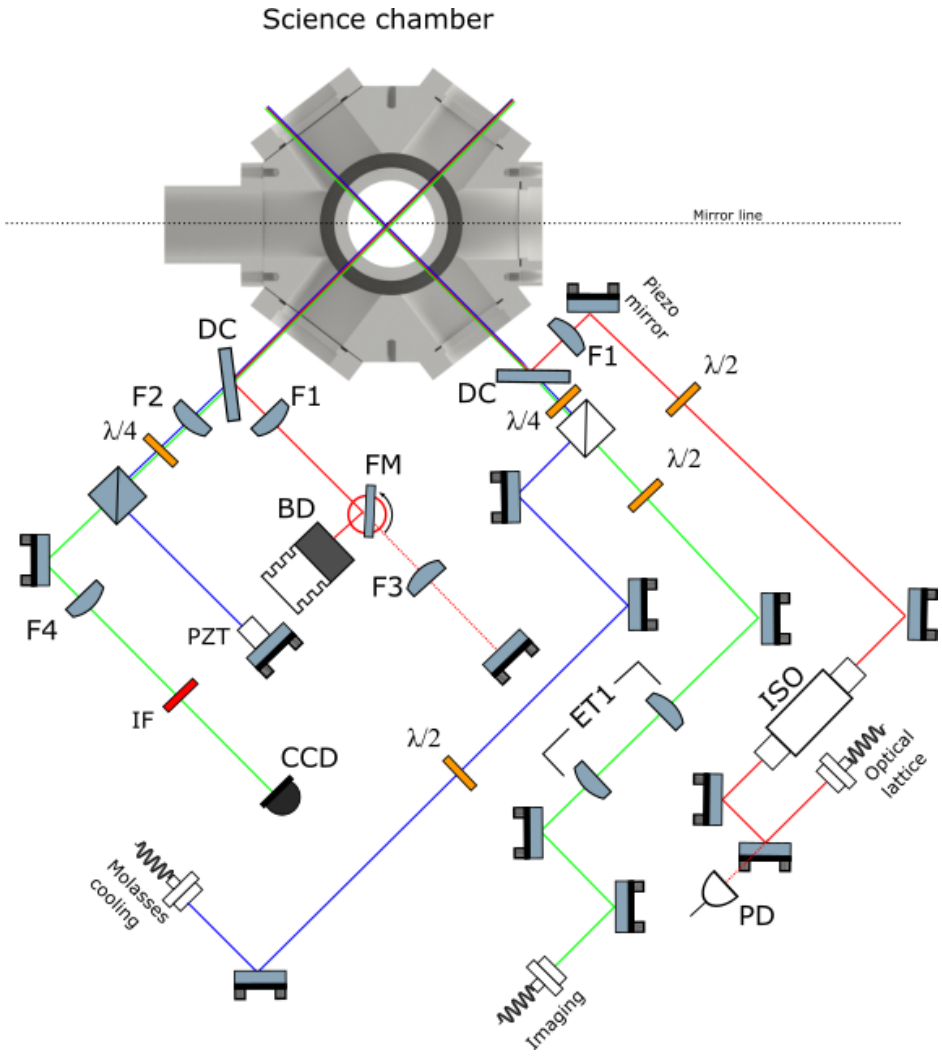

Figure 4.14: Optical setup for lattice 1. The design is symmetric, with a second identical setup for lattice 2 (not shown). Three beam paths are present. Red: Optical lattice beam path for 1064 nm light. Blue: Molasses cooling beam path using 780 nm light. Green: Imaging beam path of 780 nm with a 1064 nm interference filter (IF) positioned before the camera. Lenses are labeled F1-4 corresponding to focal lengths of 300 mm, 300 mm, 100 mm, 300 mm respectively. Light is directed into a beam dump (BD) when in CODT configuration, and a flip mirror (FM) changes the beam path to lattice configuration. An expansion telescope (ET1) increases the size of the imaging beam by a factor of two using $F = 50$ mm and $F = 25$ mm lenses. A dichroic mirror (DC) allows for combination and separation of the different beams. An optical isolator (ISO) is in the optical lattice path and a piezo actuated mirror (PZT) is in the molasses path to allow for translation of the molasses during polarisation-gradient cooling.

161(2) µm for the lattice 1 beam and 163(2) µm for the lattice 2 beam at the position of the atoms. The lattice beam is directed towards the chamber via a custom-made 2" dichroic mirror (DC) from Laseroptik, which has high reflectivity for 1064 nm light and high transmission for 780 nm.

In CODT configuration a mirror on a rotation stage ("flip mirror") directs the beam into a water cooled beam dump. In lattice configuration, the flip mirror is rotated out of the beam path and a $f = 100$ mm lens focuses the beam onto a mirror for retro-reflection. This creates a cat-eye configuration for the retro-reflected beam which is less sensitive to misalignment.

The maximum regulated power for lattice 1 and lattice 2 are 23.5 W and 22 W, respectively. Through parametric heating of the cloud, the trap frequencies of each lattice beam are measured. This is a similar measurement to the one shown in figure 4.8 and allows for the calculation of the trap depths through equation 4.1. At maximum regulated power, lattice 1 has a measured trap frequency of 455(5) kHz and a trap depth of 307(3) µK. Lattice 2 has a trap frequency of 460(4) kHz and a trap depth of 313(3) µK. This puts all three lattices well within the regime of $3000E_r$ and should adequately hold the atoms in place during imaging. Logarithmic photodiodes are used for intensity regulation such that all three lattices can comfortably reach a trap depth range of between $3000E_R$ and $5E_R$. The possibility to regulate powers which are below $20E_r$, is of particular importance when trying to transition between a superfluid and MOT insulator and performing quantum-simulation experiments.

Before imaging a single 2D superfluid of atoms, all three lattices need to be quickly ramped to maximum power[7]. Within 2 ms, the horizontal lattices are ramped from zero to 100% of their regulated power. In the same time, the vertical lattice is also ramped back to its maximum power.

The optical setups for the lattice breadboards contain two other beam paths: an absorption imaging path and a molasses-cooling path. The imaging path is use for absorption imaging with the light causing a shadow of the atoms which is collimated

[7]This is performed using linear ramps.

using a $f = 300\,\text{mm}$ (F2) lens and then imaged onto a CCD camera. The imaging beam is resonant with the $F = 2 \rightarrow F' = 3$ transition. The molasses beam, which is red-detuned from the same transition has a simpler beam path. It is retro-reflected onto itself by a $f = 100$ mm lens (F3) and a piezo-actuated mirror. Oscillating the piezo mirror allows for the standing wave created from the molasses to move through the lattice, to account for the fact that the 1064 nm lattices and the 780 nm cooling beams are incommensurable. This helps ensure a more uniform cooling for all atoms and allows for a more uniform fluorescence per atom.

4.8 Conclusion

This chapter has described the process of taking a cold cloud of atoms and manipulating it such that a portion of them are contained within a single antinode of an optical lattice. It should be noted that the layer selection is very dependent on the temperature of the apparatus, as temperature changes can physically move the coils by a few µm. Therefore, every morning an experimental sequence was ran for 1.5 hours, which brings all of the coils and the chamber to an equilibrium temperature. This time has since been reduced to 45 minutes, through a more aggressive ramping of the current through the magnetic coils and an overall decrease in the dead time of the experiment[8]. Without this, the central frequency for the layer selection constantly drifts, resulting in noticeable changes in atom number. The next experimental step is to image the atoms with the high-resolution objective. During the imaging process, the atoms need to be cooled such that they are not lost from the lattice while also releasing enough fluorescence photons to be imaged on an EMCCD camera.

[8]Dead time is any block of time in a sequence where a delay is added. This delay may be for shutters opening, the camera exposing or fail safes for the coils and fibres. This time can all be removed for the heating sequence.

Chapter 5

Single-atom imaging

Being able to image a 2D system of atoms with single-site resolution is challenging. Although, fluorescence imaging was not the intuitive first choice for imaging atoms in the Mott insulator regime, absorption imaging [151] and scanning electron microscopy [152] were initially successfully implemented, with the former being able to resolve atoms in a lattice of 600 nm spacing. However the detection rates in scanning electron microscopy are below 50% and absorption imaging has still yet to reach the single-atom sensitivity. Single-atom-resolved fluorescence images of MOT insulators with high signal-to-noise where first independently achieved at both Harvard [153] and the Max Planck Institute of Quantum Optics [154]. Although both of these experiments had an imaging resolution slightly above the lattice spacing, having knowledge of the lattice structure can allow for correct reconstruction of the atom distribution [155]. To be able to image the atoms, one needs to align the height, the tilt and the position of the objective, to allow the atoms to be imaged in focus and in the centre of the field of view. Slight deviations of these parameters can skew the point-spread function of the atoms and alter the quality of the imaging and atom identification process.

The initial part of this chapter will describe the hardware used for the imaging system with the key element being a high-numerical-aperture objective. We will discuss how this objective is mounted, how it is adjusted and more crucially how it was calibrated offline, in a test setup, before being built into the real apparatus. This chapter

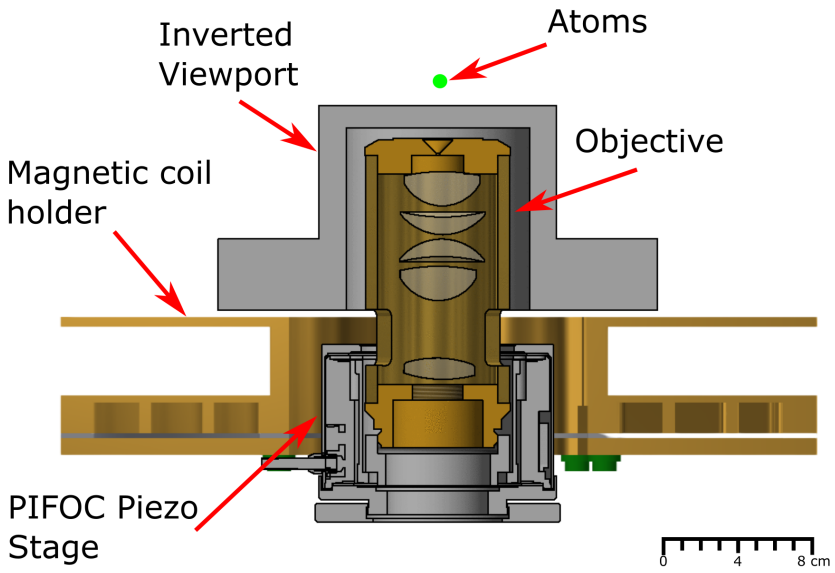

Figure 5.1: 3D render of the objective within the inverted view port with brass coil holder shown.

will conclude with presenting our first single-atom images and a brief discussion of the parameters required for the deconvolution algorithm.

5.1 Imaging setup

The core of the imaging system is a high-numerical-aperture objective, manufactured by Leica Microsystems. This objective is mounted into an inverted view port (objective held outside the vacuum) - see figure 5.1. The numerical aperture of the objective is $NA = 0.68$ for 780 nm light with a focal length of $f = 5.19$ mm (working distance of 12.8 mm). Conceptually, the Strehl value of the objective quantifies how well a given imaging system compares to an ideal imaging system by looking at the transmitted wavefront error produced by the objective. Mathematically can be defined through,

$$S = exp\left[-(2\pi\sigma)^2\right], \tag{5.1}$$

where the combined RMS wavefront error of the optics in the system is given by σ and the maximum wavefront error allowed is 0.2 [156]. In our system, we have a Strehl value of 0.97 and as such, our imaging system can provide us with diffraction-limited images. The objective is paired with an achromatic focusing lens of $f = 400$ mm, which together provide a magnification of $M = 77$. This magnification is smaller than the one ($M = 144$) used in both [45] and [3]. The smaller magnification will enable us to image 100×100 sites, rather than $\sim 50 \times 50$ µm, as performed in the previous experiments [3, 45].

The objective is encased in a brass housing with a threaded bottom section for mounting into a single-axis piezo translation stage (Physik Instrumente PIFOC P-726.1CD). The piezo stage allows for a 100 µm travel range with a minimum step size of 10 nm and a repeatability of ±3 nm, which allows for the focus of the objective to be adjusted. Appendix A contains information on the precise dimensions of the objective while figure 5.1 is provided as a rough reference. The objective is positioned 1.6 mm away from the glass window, which has a clear aperture of 40 mm, is 6 mm thick with a flatness of $\lambda/4$ and is surrounded by a water-cooled magnetic coil used for preparation of a single 2D system (see section 4.5). The clearance between the objective and the coil mount is 7 mm, while the clearance between the piezo stage and the coil mount is 1.5 mm. The flange with window was attached to the chamber with annealed copper gaskets and tightened to a precise torque as to avoid bowing of the window.

The objective is mounted to a breadboard assembly underneath the vacuum chamber (a CAD drawing without any optics is shown in figure 5.2). The piezo stage is mounted to an off-the-shelf breadboard which in turn is mounted to an aluminium board of the same size (see figure 5.2). This board is then separated from a 40 mm thick aluminium base via four heavy-duty micrometer screws (Newport BM30.10) mounted in aluminium brackets and pushing on sapphire pads. Tension is applied between the two boards through eight sets of springs connected to each board. This prevents the board from moving or sliding when the micrometers are being adjusted.

The micrometer screws allow for precise control over the tilt of the objective. This

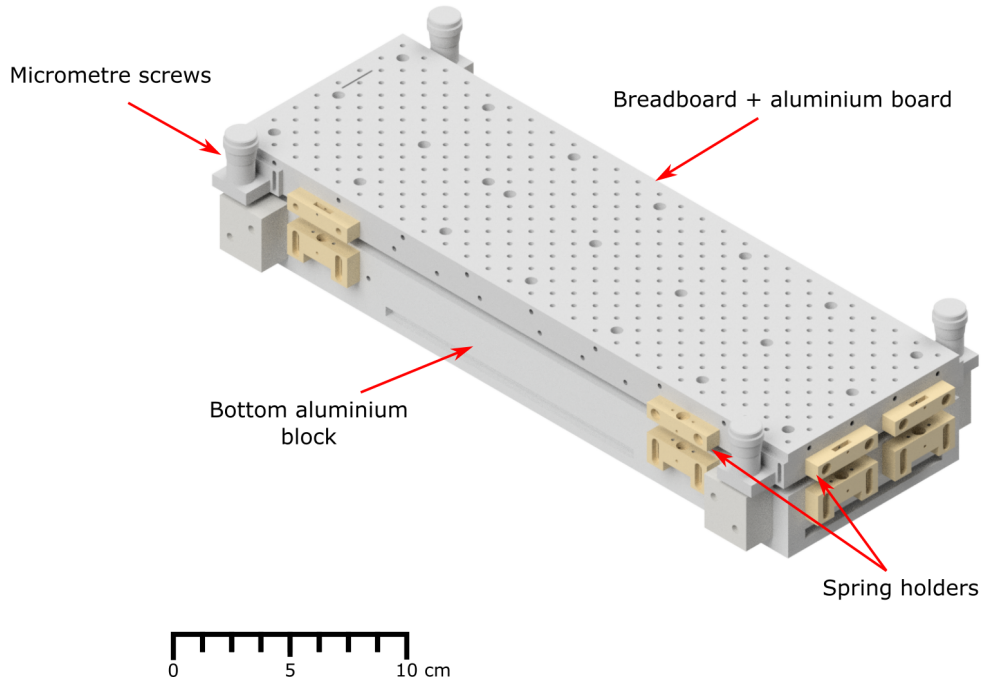

Figure 5.2: 3D CAD drawing of the microscope board without optics.

is crucial, as the objective is external to the vacuum chamber and the fluorescence from the atoms has to pass through a vacuum window. If the objective axis is tilted with respect to the glass window, it will result in an aberration of the point-spread function of the atoms. The fluorescence images of the atoms will look stretched and acquire comatic aberrations, favouring a particular direction (see section 5.4) - which is in the direction of the tilt. The point-spread function of the imaging system will be analysed later in this chapter (section 5.3.1).

The height and tilt of the objective can be adjusted through the aid of the piezo stage and the micrometer screws, respectively. However, this does lead to two problems. As the micrometer screws also adjust the height of the breadboard, when one is changed to account for an angle deviation, all of the screws need to be readjusted to account for the new height. While the breadboard is extremely stable, it is difficult to translate on the optics table. Therefore to move it below the atoms the breadboard needs to be pushed or pulled into place. For slightly finer movements mirror mounts were mounted

to the side of the board to allow a small push. However, as the board weighs more than 20 kg, small mirror mounts can not always apply a uniform force across the full board.

5.2 Microscope breadboard

The optics on the microscope breadboard contain eight different beam paths. The following section will discuss each beam path, starting with the two responsible for the fluorescence imaging. Before we built the objective into the main system, a test setup was assembled to characterise the image quality of the system, while also being capable of evaluating the best methodology for moving the breadboard into place below the atoms. A full diagram of all the beam paths on the board is presented in figure 5.3.

5.2.1 Imaging optics

The imaging path (red in figure 5.3) is akin to a conventional two-lens imaging setup, with the objective acting as the first lens. The objective captures photons from 13% of the solid angle and then collimates the light leaving the objective. The light is then reflected at 45° using a silver-coated mirror and passes through a dichroic mirror (DC1). The dichroic mirrors characteristics are: 99% reflection for 1064 nm, 50% reflection for 850 nm, 96% transmission for $770 - 780$ nm and 97% transmission for 420 nm. A $f = 400$ mm achromatic lens is used to focus the image onto a electron-multiplying CCD camera (EMCCD, Andor iXon 897).

The EMCCD camera has a pixel size of 16×16 µm, which, when scaled to the imaging plane, results in a size of 208×208 nm per pixel - this is below the separation between the atoms (532 nm). In front of the EMCCD camera are three interference filters - two are identical (Semrock FF01-780/12-25) and are placed perpendicular to the beam with one (Semrock LL01-780-25) mounted at a 31° angle to the beam. These filters block all wavelengths other than 780 ± 0.5 nm. For 1064 nm and 850 nm, the

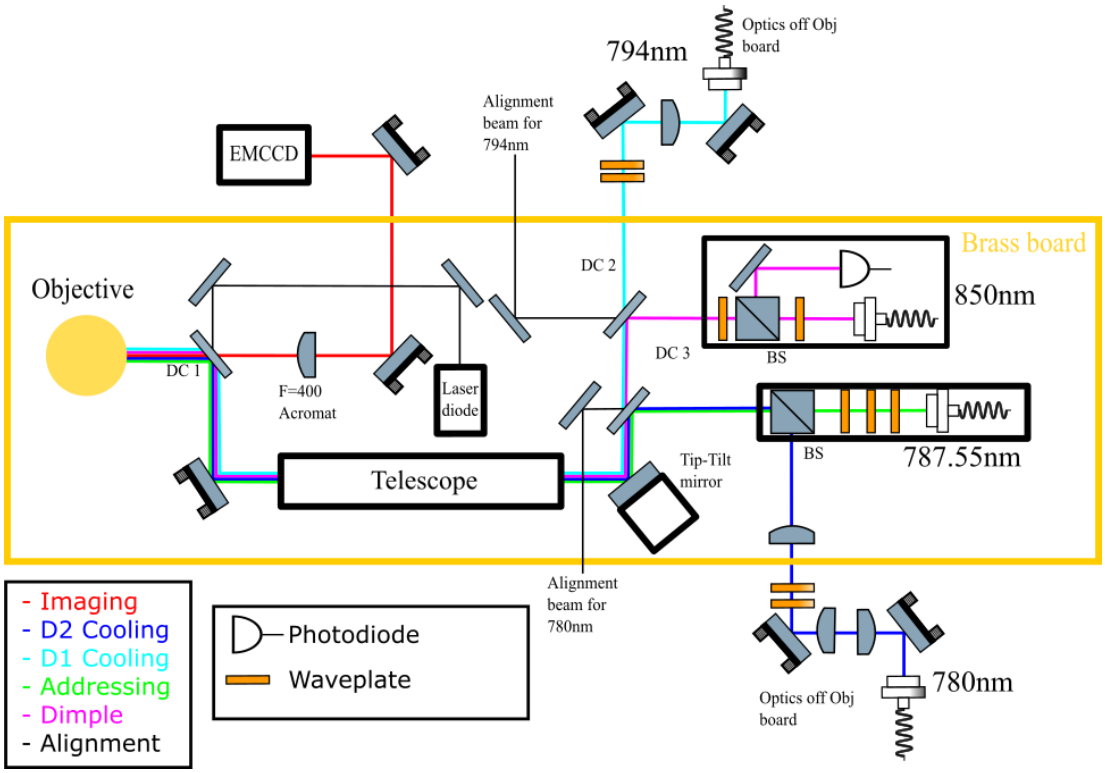

Figure 5.3: Microscope breadboard with beam paths. Three dichroic mirrors are DC1, DC2 and DC3. Red beam path: 780 nm imaging with an $f = 400$ mm focusing lens. Green beam path: Addressing beam for single-atom addressing and removal. A stack of waveplates allows for the polarisation change from the optics to be compensated with a beam splitter (BS) being used to combine beams. Dark and light blue path: Molasses cooling on both D1 and D2 transitions (only cooling on the D2-line is implemented at the moment). Pink beam path: Dimple trap of 850 nm which can be used during evaporation to a superfluid. Black beam path: Alignment beams for the molasses and dimple traps. A small laser diode is mounted to the board to aid with aligning the EMCCD camera for fluorescence imaging.

Element	780 nm light remaining after element [%]
Solid angle of microscope objective	13.0
Vacuum window coated side	99.6
Vacuum window uncoated side	96.0
Objective	91.0
Silver mirror	95.5
Dichroic mirror	96.0
Lens	99.6
Mirror	99.8
Mirror	99.8
Filter 1	98.6
Filter 2	96.0
Filter 3	98.6
Camera window	99.8
Quantum efficiency of EMCCD	83.0
Total 780 nm light to EMCCD	8

Table 5.1: Table displaying the percentage of 780 nm light remaining after propagating thorough each element in the imaging beam path.

effective optical density of the filter stack is 23 and 21, respectively.

Optics in the imaging beam path are optimised for high transmission of 780 nm light. Table 5.1 lists the total percentage of light remaining in the beam after propagating through each element in the imaging beam path. The objective collects photons from a fractional solid angle of 13% and the quantum efficiency of the EMCCD camera at 780 nm is 83%. Therefore, the maximum total percentage of fluorescence photons per atom that we could collect, accounting for all optical elements in the path, is about 8%.

To test the the microscope, an offline setup was assembled that had the same dimensions as the real chamber and included an identical inverted vacuum window (under vacuum) with the same coating and flatness as the window currently in the vacuum chamber of the setup. The flatness of the window is of particular importance. Unlike limited spherical aberrations which can be accounted for by refocusing the objective, a non-uniform flatness of the window will cause a distortion of the point-spread function across the image which is not easily corrected. An acceptable flatness across the

whole surface of the window for which diffraction-limited images can still be obtained is $< \lambda/4$. The window in our experiment has a flatness of $< \lambda/8$[1] and is anti-reflection coated for 1064 nm (external side uncoated).

5.2.2 Optics for single-site addressing

The addressing beam is responsible for the single-site selection of atoms in the optical lattice and will be at the "magic" (tune-out) wavelength of 787.55 nm [45]. An incident laser on an atom at this wavelength will produce a state-dependent differential light shift but only on one particular state. For instance, when looking at two particular hyperfine ground states of ^{87}Rb ($F = 1, m_F = -1$ and $F = 2, m_F = -2$), an incident laser of "magic" wavelength, which is circularly polarised as to drive σ^- transitions, produces a light shift only of the state $F = 2, m_F = -2$. Therefore atoms within this state, which are illuminated by such a laser, can be transferred between hyperfine ground states via a microwave field, without affecting neighbouring atoms (as long as the laser beam is contained within a single site [45]). The addressing beam path (green) is shown in figure 5.3. It is combined with the vertical molasses path on a 50 : 50 beam splitter and is reflected by a long-pass dichroic mirror (Thorlabs DMLP805) before being incident on a tip-tilt mirror and further expanded through a 4 : 1 telescope towards the atoms. This high-quality telescope takes a collimated input beam and expands it with near perfect wavefront quality, as long as the input requirements are met - input beam waist of 8.0(3) mm and the input angle of $\leq 3°$.

The element before the telescope is a two-axis piezo mirror (Physik Instrumente S-335K007) of 0.5 inch diameter. The piezo mirror provides a way of steering beams in the object plane. It has a maximum beam deflection of 120 mrad (6.8°) and is responsible for changing the angle of the input beam into the telescope. The angle deviation will cause a tilt of the beam wavefronts out of the telescope, which are then focused onto a different position in the object plane by the objective.

[1] Measured with a Fizeau interferometer.

To produce a diffraction-limited addressing beam, a low wavefront error is required ($< \lambda/4$). The wavefront error of the beam was checked in two ways. A shear-plate interferometer was inserted into the beam path after the expansion telescope, which had an added benefit of providing information on the collimation of the beam. A shear-plate interferometer does however, not provide very precise information on the wavefront error, as all of the information is obtained by looking at the curvature of the interference lines produced. A Shack-Hartmann wavefront sensor was inserted into the beam path before the expansion telescope, which allowed for precise analysis of the beam's wavefront. Using this, an RMS wavefront error of 63 nm was measured, that corresponds to an error of $< \lambda/12$, which is well below the $< \lambda/4$ requirement. This value is true for all beams which meet the input requirements for the expansion telescope.

5.2.3 Vertical molasses beam

When imaging atoms in the real setup, we require a cooling beam in the vertical axis. This vertical molasses beam is red detuned from the $F = 2 \rightarrow F' = 3$ transition (D2) and follows the dark blue path in figure 5.3. It is combined with the addressing path on a 50 : 50 beam splitter before being directed towards the atoms.

For a beam to be incident on more than a single site, it has to diverge as it enters the telescope. This is achieved by focusing the molasses beam onto the tip-tilt mirror such that it diverges with a 3° angle (to match the maximum acceptance angle of the telescope) and results in a larger beam size in the object plane. Our cooling beam is expanded with a telescope comprising of a $f = -25$ mm lens and a $f = 300$ mm lens. Another $f = 300$ mm lens is used to focus the beam onto the tip-tilt mirror[2]. This expansion and then focusing method allows for us to expand our cooling beam waist on the atoms to ~ 50 µm radially.

A larger beam is great for cooling more atoms but also provides more back-scattered

[2]The focus is actually 3 mm before the tip-tilt mirror to allow for an even larger cooling beam.

light into the camera. For every other beam in the experiment this is not a major issue as either the cameras filters block it or its not near the imaging axis. However, the vertical cooling beam is the same wavelength as the imaging light and counter-propagating with the imaging path. Therefore, the light needs to be aligned through the objective in such a way that it does not result in too much background light, which can originate from the objective optics or the uncoated side of the vacuum window.

5.2.4 Dimple trap and D1 cooling

As can be seen from figure 5.3, there are two additional paths on the microscope breadboard: 850 nm and 794 nm. The 850 nm beam path will be used for a dimple trap propagating back through the objective. The beam path consists of two $\lambda/2$ waveplates and a PBS cube[3] which creates a pick off for intensity regulation. The beam is overlapped with the addressing beam by two dichroic mirrors, DC2 (LaserOptik: custom coating[4]) and DC3 (Thorlabs: DMLP805). The implementation of this dimple trap is currently underway and potential results are discussed in section 6.1.

The 794 nm beam path is intended to be utilised for grey-molasses cooling on the D1 line of ^{87}Rb. Grey molasses is normally implemented for cooling atoms in which the hyperfine transitions are poorly resolved, such as on the D1 lines of lithium [157] and potassium [158]. The methodology can also be applied to the D1 line of ^{87}Rb [159], even if the separation between the two hyperfine excited states of $5^2P_{1/2}$ is > 800 MHz. One could conceive of a cooling method for a 2D layer of atoms trapped within a 3D optical lattice using D1 cooling for one axis and D2 cooling for the other two. The difference in wavelengths (14 nm), would make blocking the cooling light possible and leave the imaging (D2) light unaffected - therefore producing images with excellent signal to noise.

[3] All fibre out couplers have a PBS cube as the first element to ensure a clean polarisation and as such, have been omitted from all schematics.

[4] High transmission $405, 767, 780$ nm and high reflectivity 1064nm.

5.3 Imaging test setup

5.3.1 Measuring the point-spread function

The linear response of an imaging system to light from a point source produces an intensity profile in the image plane [160], which is known as a point-spread function and for an aberration-free system, is diffraction limited. A diffraction-limited point-spread function has a bright central region that decays outwards and forms an interference pattern which can be theoretically described by an Airy function [161],

$$I(x) = I_0 \left[\frac{2J_1(x)}{x} \right]^2, \tag{5.2}$$

where I_0 is the peak intensity of the pattern and J_1 being the first order Bessel function, with,

$$x = \frac{q\,3.795}{q_1}. \tag{5.3}$$

Where q is the radial distance with the normalised radius of the first minimum (first dark ring) of the function q_1, also known as the Rayleigh resolution, being expressed through [162]

$$q_1 = 1.22 \frac{\lambda}{2NA} \tag{5.4}$$

and is only related to the numerical aperture of the objective and the wavelength of the imaging light. Imaging using 780 nm light with $NA = 0.68$, the first minimum is at $q_1 = 700$ nm. At first this would suggest that single-site-resolved imagining is

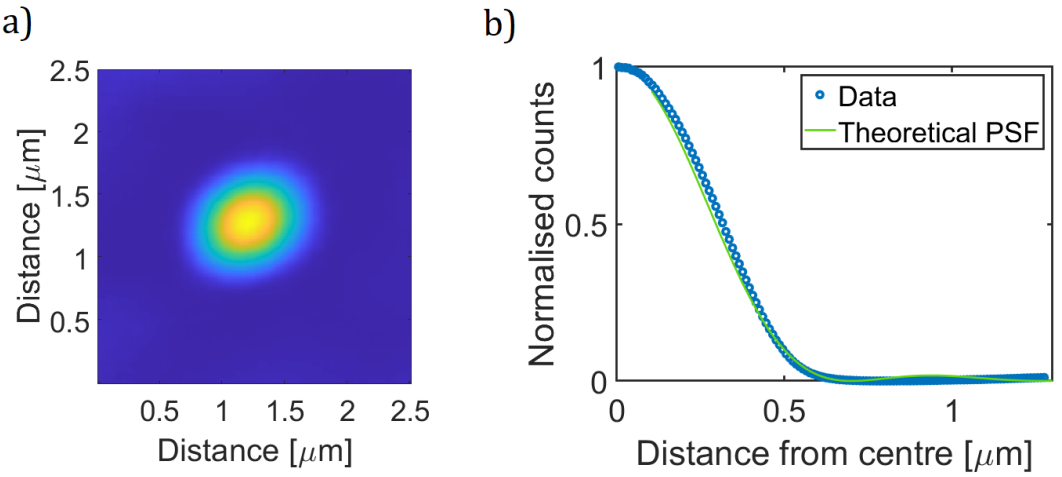

Figure 5.4: Point-spread function of the objective in the test setup. a) An average fluorescence image of forty point sources. b) Radial average of a) (blue data points), with a calculated point-spread function from equation 5.2 (green line) for the imaging system.

not possible according to the Rayleigh criterion. It states, that in order to distinguish two point sources, the central intensity peak of one source must lie outwith the first minimum of the other. Two atoms in neighbouring lattice sites would be separated by 532 nm and as a result, neighbouring atoms are closer than q_1 with respect to each other and would not be resolvable. Although this imaging system on its own would not be able to distinguish two atoms on adjacent sites, it could tell if there is an an empty site between two atoms [45], as they are then separated by larger than 700 nm (see figure 5.9). This methodology only works if prior knowledge of the lattice structure and point-spread function of a single atom is known. This ultimately results in a system with sub-resolution single-site imaging, without having an imaging system that can achieve that on its own.

To measure the point-spread function of the imaging system, it was placed into the test setup. This setup is identical to the real system with the atoms being replaced by holes in the reflective coating of a glass plate ("star test"). The holes are $100 - 300$ nm in size and distributed randomly across the coating to ensure that any Talbot effects are suppressed. The light that is transmitted through the holes approximates a point

source and the imaging system can be aligned by minimising the point-spread function from the holes. Figure 5.4 shows an average of 40 such point sources and the associated point-spread function for the radially averaged image. The point-spread function has excellent agreement with the theoretical one calculated from equation 5.2. We are not able to view the second peak of the function in any of the images for either the test setup or the real system thus far.

5.3.2 Pre-alignment of the microscope breadboard

Multiple aspects of the imaging system required some practicing with the test setup to gain a better understanding of the best methods: finding the centre of the field of view, ensuring the objective could focus properly and visually checking that the addressing beam could be seen and moved using the piezo mirror. We also provided alignment aids which help find the camera's position, along with the tilt of the objective axis with respect to the bottom vacuum window. Figure 5.5 show multiple images taken with the test setup, where every circle is a point source from the "star test".

The field of view can be found more easily by replacing the focusing lens in the imaging path with a $f = 100$ mm lens [figure 5.5a)]. The images of the point sources can be seen to stretch at the edge of the field of view in each image. All of the stretched profiles point in the same direction, which is away from the centre of the field of view. Once the field of view has been aligned onto the centre of the camera, the $f = 400$ mm lens is placed into the system [figure 5.5b)].

The addressing beam incident on the "star test" plate produces a reflection that is captured by the objective and as such, the addressing beam can be seen in the imaging path (central dot with halos in c) of figure 5.5). As this is a different wavelength from the imaging beam (787.55 nm), it appears out of focus while the system is focused on the point sources. When addressing is required for real atoms, the objective piezo stage will be adjusted to allow the addressing beam to be focused. The beam was also translated across the full field of view by using the maximum control voltage range of

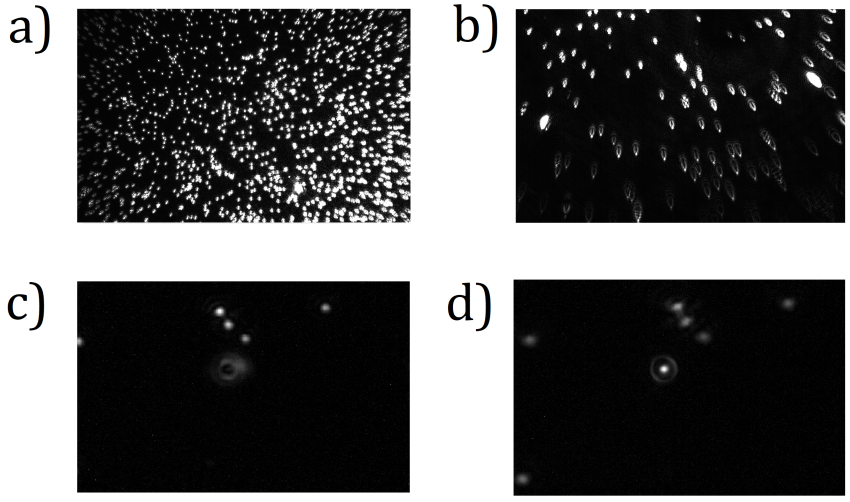

Figure 5.5: A selection of microscope images from the test setup involving the "star" test. a) Image is taken with a $f = 400$ mm lens in the imaging path but with the camera positioned away from the center of the field of view. b) Image is taken with a $f = 100$ mm lens in the imaging path. c) Image is taken with a $f = 400$ mm lens in the imaging path with the addressing beam being incident on the "star" test plate. The objective is focused on the point sources. d) Is the same as c), although the objective is now focused on the reflection from the addressing beam.

the tip-tilt mirror and visually verified to be working correctly.

Alignment aids are required in order to find the right location of the camera and the right tilt of the objective when placed into the real setup. The integration of the microscope board into the experiment would be extremely difficult without these aids[5]. To help fix the camera position, a laser diode is mounted to the microscope board. This beam is then overlapped with the imaging path and acts as a positional reference for the centre of the imaging system.

The tilt of the objective relative to the chamber is something that can be quite tricky to align without some sort of aid. Once the microscope breadboard is aligned in the test chamber, a small piece of glass was permanently glued to the side of the objective[6]. A beam passing through the top window and reflecting from this glass would result in two reflections: one from the uncoated side of the vacuum window and

[5]When asked by a theoretical colleague how hard a task this was, I responded with: "you would essentially be looking for a needle in a stack of needles, but in the dark".

[6]This piece of glass is a broken microscope slide and is glued onto the top of the PIFOC stage.

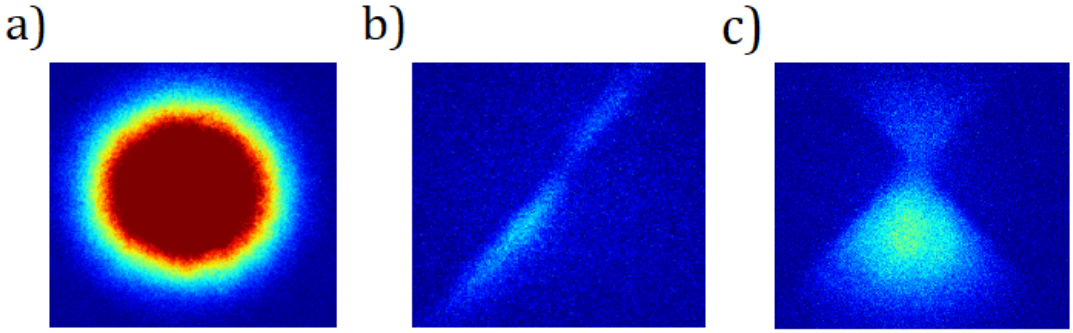

Figure 5.6: Side on absorption imaging with repumper light passed through the objective. a) A cloud is released from the CODT in the science chamber and imaged with absorption imaging with imaging and repumper in the horizontal plane. b) The same as a) with the exception that the repumper light for imaging is passed through the vertical molasses cooling path. c) The same as a) but the repumper light for imaging is passed through the addressing beam path.

one from the uncoated glass. A beam is aligned such that it is parallel to the vertical axis and then reflected from the glass plate. The resulting reflections are overlapped after a total travel of 3.5 m. Repeating the alignment after the breadboard had been placed into the real setup provided us with a very good initial tilt of the objective axis with respect to the vacuum window.

5.3.3 Implementation into the real system

The addressing beam itself can act as a reference for aligning the position of the microscope breadboard. Repumper light was shone through the addressing beam path to find the position of the objective with respect to the atom cloud[7]. Figure 5.6 shows absorption images of clouds released from the CODT beams in the science chamber with repumper light in either the addressing beam path or the vertical molasses beam path. As can clearly be seen by b) of figure 5.6, the path for the vertical cooling beam is very angled when compared to the addressing beam path. The purpose of this was to reduce the amount of back reflection from the cooling beam to the camera. Image

[7]Swapping fibres at the output can misalign beam paths. To prevent this, but allow for quick swapping of beam paths, intermediary fibres are used as a type of "middle connection" which can be easily swapped and connected through fibre-fibre connectors.

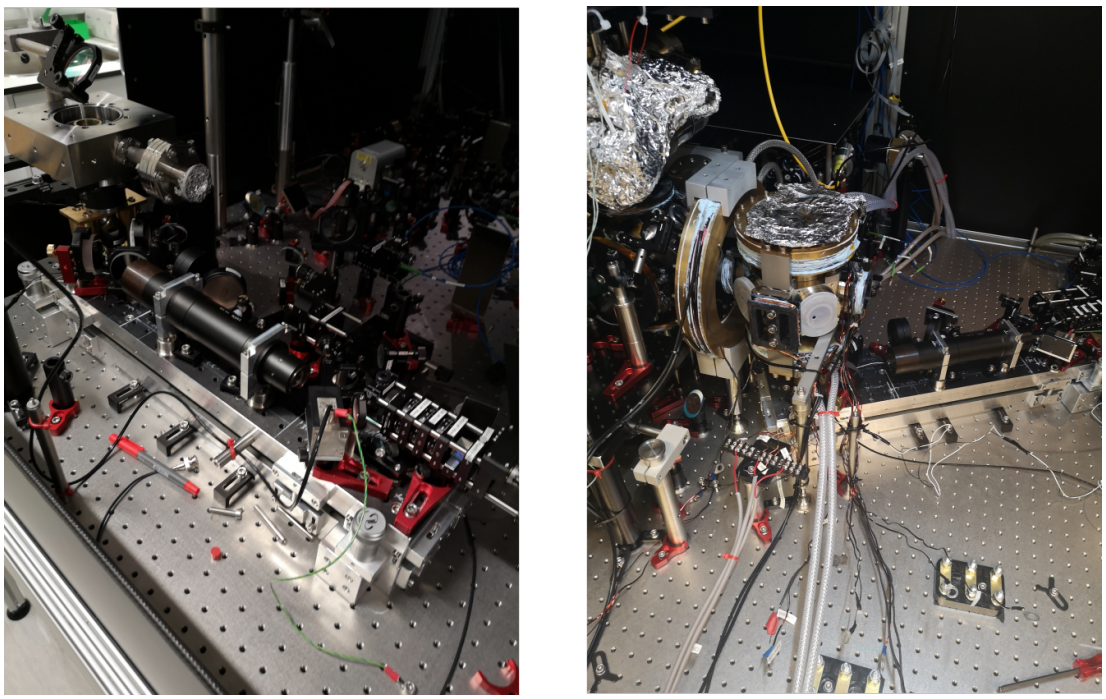

Figure 5.7: Photographs of the microscope breadboard. Left is the breadboard in the test setup and right is the breadboard in the real chamber.

c) from figure 5.6 shows repumper light in the addressing beam path with very good alignment onto the cloud. As the addressing beam has been pre-aligned with the center of the field of view, we now have a way of aligning the full system with the objective at the heart.

One notable issue that arose from installing the microscope breadboard into the real setup was an alignment mismatch that originated from the objective piezo stage. The piezo stage is connected to a controller through a 1.5 m cable which has an extruding metal protector from the housing. Looking at the design of the quadrupole coil holders, one can notice a split in the holder - see appendix A. Originally, this is to prevent the build up eddy currents in the mounts, but a slightly deeper grove has been cut to allow space for the piezo-stage cable connector. This connector should therefore align perfectly with the grove and situate the board parallel to the transport axis. However, the coil holders were mounted to the board in such a way that that this grove was required to be rotated by $25 - 30°$. As a result, the full objective board needed to be

rotated, as can be seen in figure 5.7[8].

5.4 Alignment of the microscope objective

To calculate if a particular lattice site is populated, one must know the point-spread function of the atoms, the angle between the lattices and the separation between atoms. All three of these points are reliant on the system being correctly aligned and for that reason, a lot of effort went into ensuring that the objective axis is perpendicular with the bottom vacuum window surface.

After the imaging system had been installed into the real setup, the alignment of the microscope breadboard was initially done using parameters from the test setup; however, further alignment was required before single-atom images could be taken. The light for imaging is produced by molasses cooling the cloud for the duration of the exposure time, using a vertical molasses beam and two retro-reflected horizontal molasses beams. All three of the molasses beams beams originate from the same source, which can result in an interference profile being created across the cloud. This profile can lead to regions of higher and lower intensities and in turn lead to a non-uniform fluorescence from the atoms (as seen in [45]). To prevent this, a relative frequency detuning of $-100, 0, 100$ Hz is applied to the molasses beams in lattice 1, lattice 2 and the vertical axis respectively. This is performed by means of a direct digital synthesizer, which controls the frequencies of the respective AOMs. In addition to this, the retro-reflection mirrors for the horizontal molasses beams are mounted onto piezo actuators. This allows us to move the polarisation gradient created by the molasses beams and results in a more homogeneous cooling, which is required as the lattice and molasses beam wavelengths are not commensurable.

Figure 5.8 is one of the first single-atom images we took with the objective. It can

[8]There is a large magnetic coil placed between the two chambers which has yet to be mentioned. This Feschbach coil will be used in the future to create the large magnetic fields responsible for the evaporation of ^{85}Rb. However, in the future it will be impossible to place a coil in that location without major disruption to the experiment. Therefore it has been implemented now.

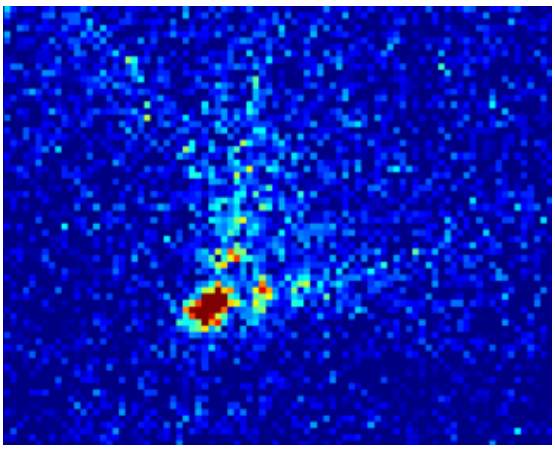

Figure 5.8: One of the first single-atom images taken.

clearly be seen that there are two additional intensity maxima to the right of the main peak. The additional maxima have a tail like effect which points in the same direction as the tilt of the objective relative to the glass window. This is of particular use to know when alignment of the objective is required. When the relative tilt between the window and objective becomes small and one can no longer tell by eye if there is a tilt, a quantitative measurement of the tilt is required (computational analysis).

An example of the analysis process (which is performed after every realignment when the relative tilt is small) for single atom images is presented in figure 5.9 when the system was tilted [a)] and then correctly aligned [b)]. Thirty fluorescence images similar to figure 5.10 are taken of a dilute cloud of atoms. For the misaligned situation, 68 single atoms were selected that had a radial separation of at least 10 pixels from another. A radial average is obtained by first overlapping each identified atom (left images of figure 5.9) and then calculating an average around a circle, centered on the intensity maximum, with varying radii and averaging these results. This produces a point-spread function which is plotted in terms of real sizes - right images of figure 5.9. The theoretical point-spread function can be calculated using equation 5.2. In an ideal situation, the averaged image would be perfectly radially symmetric and be described by an Airy function; however, a double Gaussian can approximate the point-spread function as well [160]. A double 2D Gaussian for fitting the point-spread function is defined by [45],

$$PSF(x,y) = C\Big[(1-a)\exp(-0.5(x^2+y^2)/\sigma_1^2) + a\exp(-0.5(x^2+y^2)/\sigma_2^2)\Big] \tag{5.5}$$

where C is the peak fluorescence, a describes the relative amplitudes and σ_1, σ_2 are the widths of the two Gaussians. An additional maxima can be seen in the left image of figure 5.9a). The feature is due to the objective still being slightly tilted with respect to the vacuum window while also having the imaging system out of focus [160]. The difference in tilt between the objective and vacuum window contributes the largest effect to the point spread function. For the tilted objective (a) of figure 5.9), the measured point-spread function differs substantially from the theoretical one, such that the first minimum q_1, extends well beyond two lattice sites.

After accounting for the tilt of the objective, a selection of images was taken. Figure 5.9b) shows the averaged image of 64 single atoms in focus, along with an average point-spread function. It can be clearly seen that the point-spread function is now symmetrical around the central intensity peak. When comparing it to the theoretical point-spread function (equation 5.2), we find that these are now in good agreement. Although the position of the first minima is slightly offset, this is because of the residual Airy disk that is slightly visible in the image and may be a result of a very small defocusing of the objective ($< \lambda$)

As well as a tilt, the imaging system being slightly out of focus would result in a reduction of the total fluorescence counts on the camera. We can estimate the total fluorescence rate per atom through the scattering rate [2]

$$R_{sc} = \left(\frac{\Gamma}{2}\right)\frac{(I/I_{sat})}{1+4(\Delta/\Gamma)^2+(I/I_{sat})}, \tag{5.6}$$

where the total intensity of the cooling beams is $I = 0.1I_{sat}$, in the current setup. The

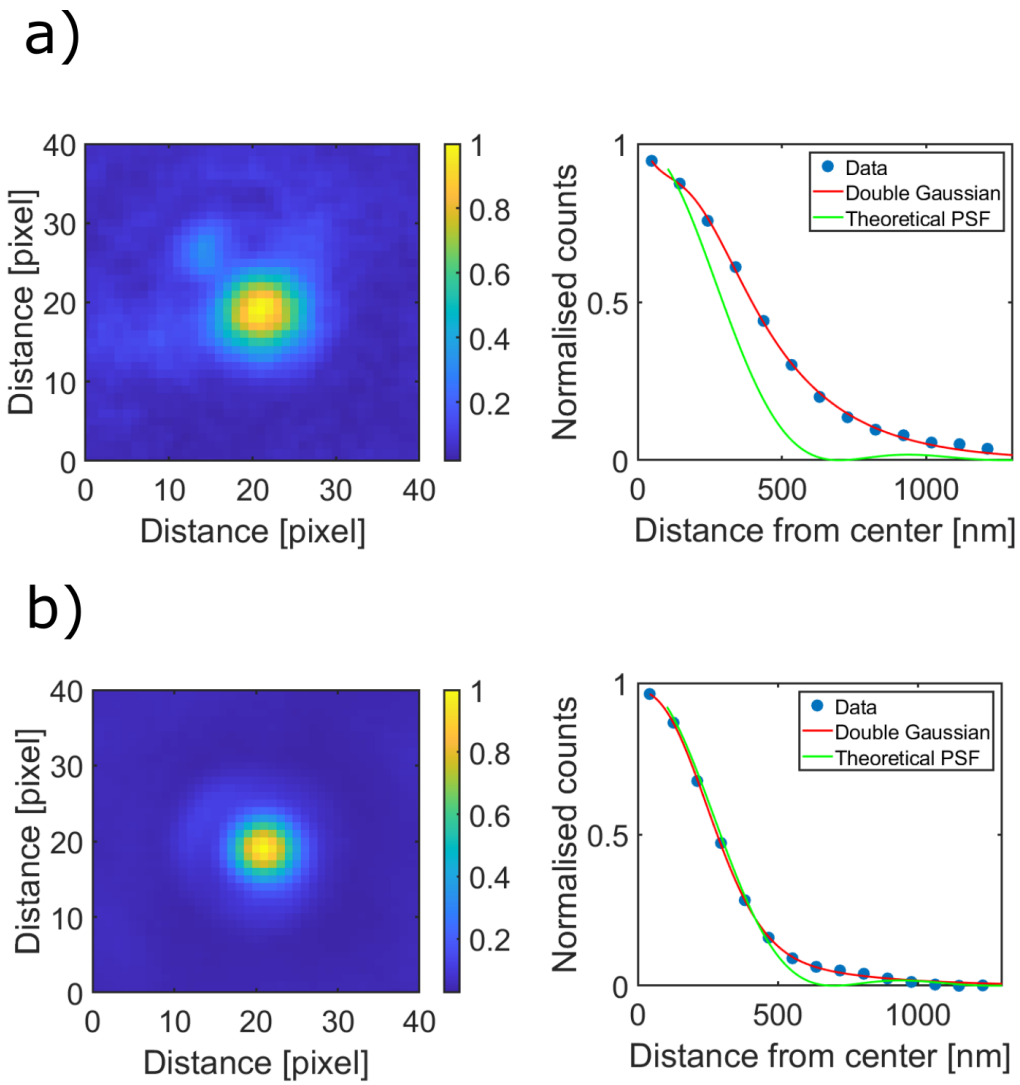

Figure 5.9: Point-spread function before [a)] and after [b)] alignment. a) Left shows an averaged fluorescence image of 68 single atoms. Right shows the radial average of the same 68 single atoms before alignment, with a double Gaussian fit and the caculated point spread function. An exposure time of 800 ms and an EMCCD gain of 400 was used. b) Left shows an averaged fluorescence image of 64 single atoms with the right graph showing the radial average after alignment for the same 64 single atoms, with a double Gaussian fit and the caculated point spread function. An exposure time of 400 ms and an EMCCD gain of 100 was used.

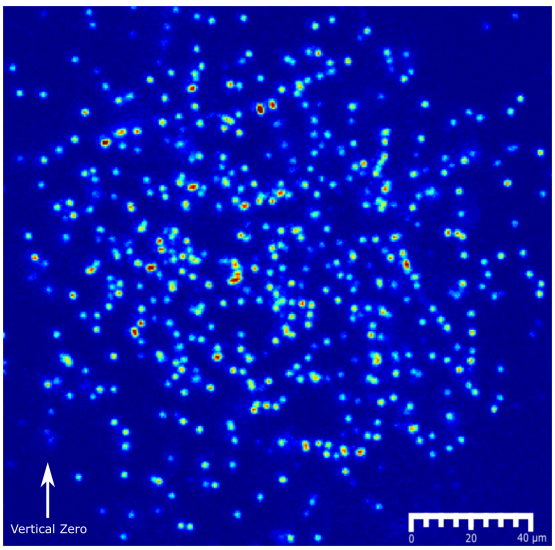

Figure 5.10: Fluorescence image of single atoms.

imaging path should allow the capture of around 8% of total light from the atoms (5.1). During an imaging time of 400 ms, with a cooling laser detuning of 46.5 MHz, each atom should emit around 500 photons. This would result in a total number of fluorescence photons on the camera of roughly 40 and readjusting this for the gain of the camera (100), means that around 4000 counts per atom should be imaged. When comparing this to the measured peak counts per atom for the tilted objective of 2000(250) - as taken from a) of figure 5.9 (adjusted for the same gain and imaging time) we see that the peak number of photons per identified atom is $\sim 50\%$ of the expected value. Although the total number of photons that reach the camera from the atoms is mostly constant, a tilt of the objective with respect to the vacuum window will change the point spread function and in turn spread the total photon number across a wider area. This means that peak photon count per identified atom can be used as an indicator that the objective is still tilted with respect to the glass window. We estimate this tilt to be at least 4 arcminutes by comparing the point-spread function to a data sheet of simulations performed by Leica Microsystems [163].

We present four of the data-sheet simulated images[9] alongside a real atom picture from our experiment [figure 5.11a)]. For the simulated images, the angle between the

[9]Provided by Leica Microsystems

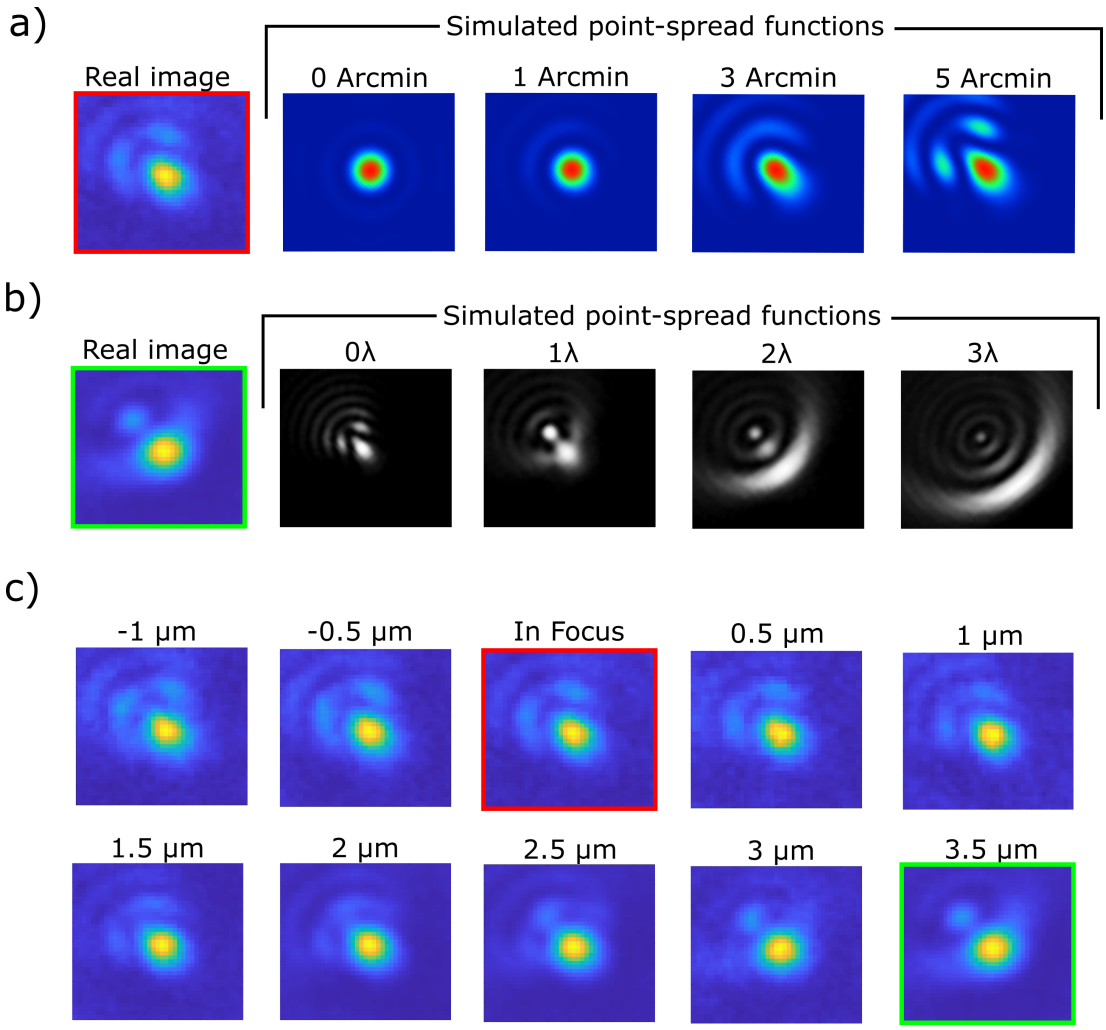

Figure 5.11: Point-spread function analysis. a) The real image in focus is compared to a number of simulated point-spread functions for different tilt angles of the objective axis. Data acquired from Leica Microsystems [163]. Each image corresponds to a degree of tilt between the glass window and the objective in units of arcminute. The images have been orientated to align with the real image. b) A real image but out of focus is compared to a number of simulated images for an objective that has been tilted by 5 arcminutes [160]. Each image is a step of one wavelength from the focus. c) Each image contains an averaged point-spread function of > 50 single atom images for varying focus positions of the objective. The red highlighted image is at the focus, with the green image being 3.5 µm closer to the atoms and as such, out of focus.

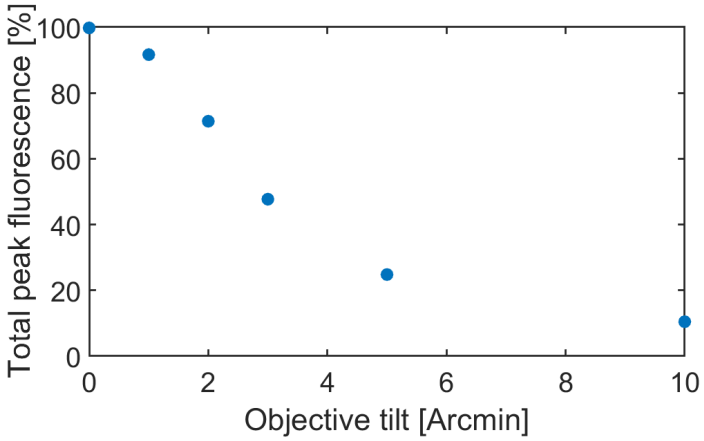

Figure 5.12: Total simulated peak fluorescence from a point source for varying the angle of the objective axis relative to a glass window [163].

glass window and the objective is varied between $0 - 5$ arcminutes, with the images being orientated to align with the real image[10]. The additional intensity peaks tilt in the direction that has the smallest distance between the glass window and the objective. After a large enough tilt ($\approx$ 5 arcminutes) the intensity profiles are separated into distinct regions, with the central spot becoming stretched. A tilt of the objective axis relative to the glass window would also result in a reduction of the peak fluorescence. Figure 5.12, which has been adapted from our Leica Microsystems data sheet, presents the simulated peak fluorescence when varying the tilt of the objective axis. If we assume that our system initially had a tilt of 3 arcminutes, then this would result in a reduction in the peak fluorescence of $\sim 50\%$ - which is what we initially observed. However, when looking at the in-focus peak fluorescence (b) figure 5.9), we find an average of 3600(300) counts per atom for an exposure time of ~ 400 ms and a EMCCD gain of 100. Comparing this to the theoretical value of 4000 counts per atom previously calculated for the same exposure time and EMCCD gain, we find that there is a good match between the two.

To look at how defocusing of the objective can affect the point-spread function, figure 5.11 b) uses simulations of the point-spread function (images taken directly from [160]) for an objective which has been tilted by 5 arcminutes in relation to a glass plate.

[10]The total transmission has been normalised in each image.

As the imaging system is brought out of focus, fine details of the Airy disks are lost and they blend into larger features. These features eventually look like "round" disks and can mislead one into thinking the images may be in focus[11].

To better evaluate the tilt of the objective, a selection of averaged point-spread functions for different focus positions are given in c) of figure 5.11. The point-spread function created by the atoms can be seen to change as the focus of the objective is changed. Scanning the objective through the focus allows for a more uniform understanding of where the focus is and how severe the tilt is.

Currently the back reflection of imaging light produces a speckle-type pattern on the camera. A quick solution to account for this is to take a background image with the speckle pattern but with no atoms and subtracting it from the single atom image. The background image in this case is produced by taking an average of more than 30 background images[12]. This washes out any fluctuations that arise during imaging. However, if the cooling light in the imaging axis was not the same wavelength as the imaging light then the background counts could be very low and a simple one time average of a bulk of images would suffice for creating clean images. A future option is to implement D1 cooling of ^{87}Rb [159] in a 3D optical lattice which would avoid cooling light being captured by the camera and improve the quality of the background.

5.4.1 Determine lattice angles and spacing

One last measurement which can be performed to provide further information for a deconvolution algorithm, is to determine the lattice angles and spacing. The angles allows the algorithm to calculate where each lattice site is in relation to the image and then calculates the separation between each atom which provides an image magnification. This is performed independently of measuring the point-spread function.

To calculate the lattice angles, images of dilute clouds (similar to figure 5.10) are

[11] As was the case with us for a period of time.

[12] A more pragmatic approach is to take more than 30 background images and then update this average with a new background every cycle.

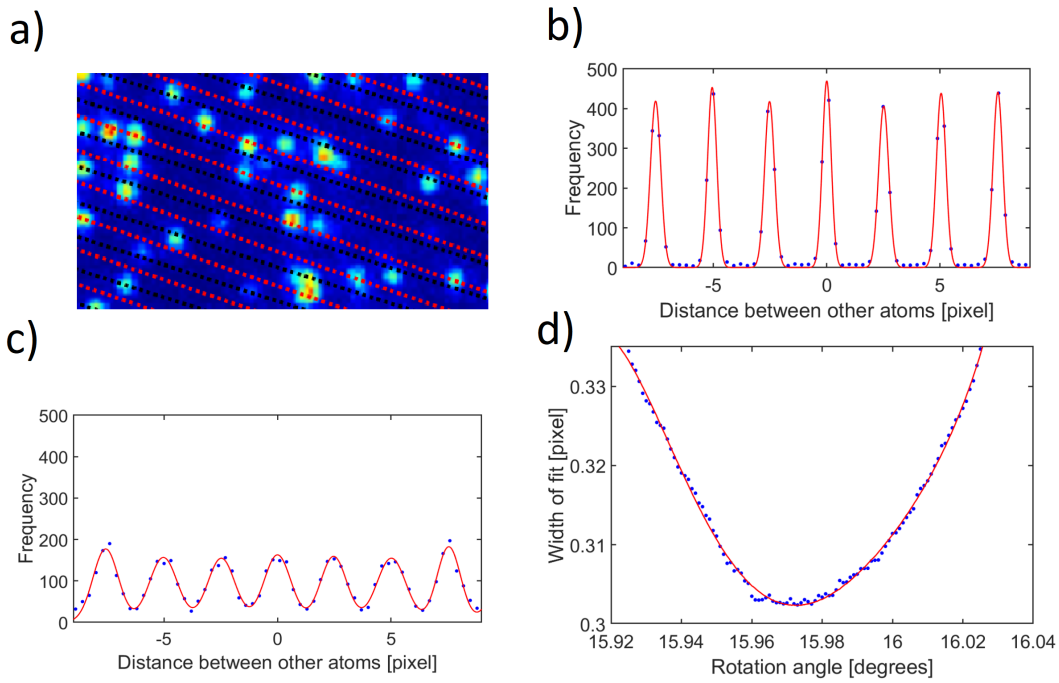

Figure 5.13: Measurement of the lattice angle for lattice 1 [45,143]. A similar process is repeated for lattice 2. a) A florescence image is shown on lattice angles of 15.972°(red) and 15.700°(black) layered on top. b)
For lattice angle 15.972° the maximum points of plotted histograms are shown (without bins visible) to display the frequency of an atom appearing at a particular distance - in pixels - from another atom. A multi-order equidistant Gaussian is fitted to the plot. All data is an average of 21 fluorescence images. c) The same as b) but with a lattice angle of 15.700°. d) A selection of lattice angles are probed between 15.925° and 16.025° with a resolution of 0.001° and the width of a Gaussian fit from the histographic plots is recorded. A polynomial fit is applied to the data. The minimum of this fit would correspond to the narrowest, most uniform structure for the atoms and in turn, the correct lattice angle. The lattice angle is found to be 15.972(8)°.

analysed. An algorithm identifies single atoms and then for a particular angle, overlaps a set of parallel lines [figure 5.13a)] and counts the total florescence counts on those lines [see figure 5.13b) and c)]. A histogram is created with the number of florescence counts along a particular line and a set of equidistant Gaussians is fit to the data. This process is repeated for a full range of angles. A graph showing fitted Gaussian width per lattice angle being presented in figure 5.13d). A minimum width of the fitted Gaussian will correspond to the correct lattice angle [26, 45]. We obtain lattice angles from the image shown in figure 5.13 for lattice 1 of $15.972(8)^\circ$ and $90^\circ + 19.593(8)^\circ$ for lattice 2. This provides a crossing angle of $93.621(8)^\circ$. The distance between atoms in each axis is 2.52(1) pixels and with a lattice spacing of 532 nm, this corresponds to a measured magnification of 75.8(3).

As a final observation, we did manage to observe single atoms without using any EMCCD gain. For an imaging time of just 400 ms and a molasses detuning of 45 MHz, we were able to capture the image shown in figure 5.14. Although the signal to noise of the image is very low (below 2), single atoms can still be seen even for such a small exposure time. This is quite an interesting result and reinforces the idea that our imaging system is very well aligned such that we maximise the peak fluorescence captured per atom.

5.5 Conclusion

This chapter has described the setup used for single-atom imaging, the method of imaging and the steps required to reconstruct the position of single atoms within an optical lattice. There is the possibility to add a number of improvements to this system. To reduce the amount of back-reflected light on the atoms from the vertical cooling beam, cooling on the D1 transition of ^{87}Rb could be used [159]. This would allow a cooling beam to pass on axis through the objective while the narrow-band filters in front of the camera would be able to block the light. The magnification of the imaging system can also be changed by swapping the focusing lens in the imaging path, if required.

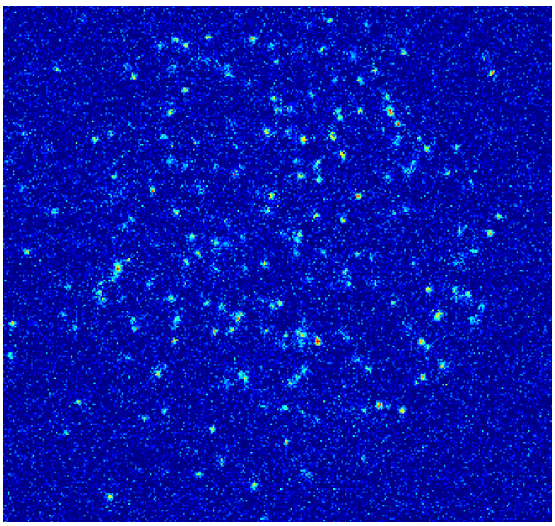

Figure 5.14: Fluorescence imaging without any EMCCD gain with only a 400 ms exposure time and a molasses detuning of 45 MHz.

For quantum-simulation experiments custom potentials created by light are useful to the realisation of complex systems. A spatial light modulator (SLM) can be utilised to reflect light towards towards the objective and impart a particular phase profile on the light, which the objective can focus down and transform into custom potentials. The experiment has been designed with all of these extensions in mind and the useful hardware is already in place for the majority of it.

Chapter 6

Outlook

Providing an apparatus that is capable of imaging ultracold single atoms with single-site resolution is a great stepping stone towards the creation of a complex quantum simulation machine. We were able to create a single layer of ultracold atoms trapped within a 3D optical lattice; however, during my time working on the experiment, we were not able to create a single superfluid layer. Shortly after leaving the experiment, superfluidity and Mott insulation of single atoms in a single layer were achieved. This chapter will start by discussing the progress made towards creating a superfluid layer during the course of my PhD while showing promising new results. The chapter shall conclude with a brief description of the future plans for the experiment. Most notably, the development of the apparatus into a dual-species device and the ability to create optical lattices with more complex configurations.

6.1 Vertical dimple trap

Cooling a single 2D sheet of atoms to degeneracy poses a number of challenges in our system. The most notable of these is a result of the forced evaporation in the vertical lattice after the preparation of atoms in a 2D layer. During this process, the vertical lattice potential is reduced to $30E_r$. Therefore, any forced evaporation will work poorly due to the low trap frequency and atom density within the trap. The

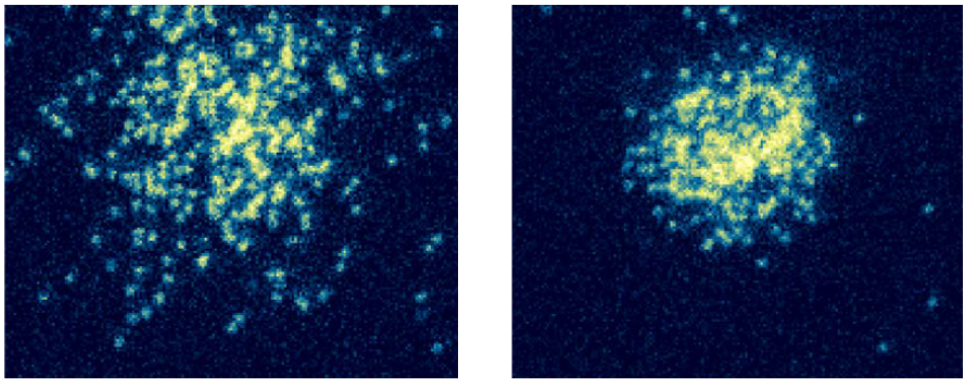

Figure 6.1: Fluorescence images taken from [3] showing the effect of the vertical dimple trap. The left image shows a 2D layer after forced evaporation in the vertical lattice without the dimple trap. The right image shows the same evaporation but with the dimple trap present during the evaporation.

problem is identical to the one described in section 3.2.3 and the solution in this case, is to also to use a dimple trap (that propagates through the objective). This however, is not critical for the creation of a superfluid but provides a greater level of control over the evaporation process.

As mentioned in section 5.2, the microscope breadboard contains an beam path for the dimple trap ($850 - 852$ nm). The wavelength of this beam was chosen not only because it is far enough detuned from any transition, but also because it is a wavelength that works with our dichroic mirrors - even if the transmission is only $\sim 30\%$. The dimple trap beam is passed through the high-quality telescope on the microscope breadboard and then through the objective and incident onto the atoms. Just like the vertical molasses beam, the dimple beam needs to diverge when entering the telescope in order to have a larger than single site width in the object plane but still be smaller than the vertical lattice beam. A tighter trap for performing forced evaporation will provide larger trapping frequencies and can lead to the faster creation of a superfluid. Unfortunately, at the time of writing this thesis, the dimple trap is still being setup and no data is currently available. However, a vertical dimple trap was implemented in the first quantum gas microscope experiment at Strathclyde and the effect it had on a single layer during evaporation can be seen in figure 6.1 [3]. We hope

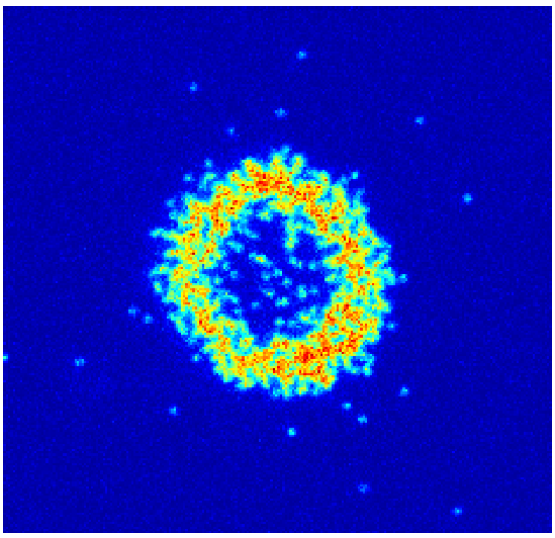

Figure 6.2: Single atom florescence image of a dense Mott insulator as taken with our machine. A continuously varying chemical potential (as described by section 2.3.3) is created due to the Gaussian profile of the optical lattice beams. This leads to discrete atom numbers per lattice site, which can be visualised through the parity of the imaging method [26] and creates an apparent hole in the cloud.

to have the same improvement over the confinement of atoms in the 2D layer.

The introduction of a vertical dimple trap will allow for a more controlled creation of a 2D superfluid cloud. The transition to a Mott-insulating state is relatively straightforward when compared to some of the previous experimental steps. To go from a superfluid to a Mott insulator, the cloud is localised onto individual sites by increasing the trapping lattice potential, reducing the tunneling rate [43, 164]. A Mott insulator was recently created in the lab by first creating a 2D superfluid contained within the vertical lattice. Figure 6.2 shows a preliminary image of this Mott insulator taken at Strathclyde, showing well-defined shells of chemical potential as described in section 2.3.3.

6.2 Alternative lattice potentials

With single-site addressing, one atom at a time can be addressed and removed from the optical lattice. If starting with a fully populated square lattice, one could imagine with

enough removal steps, any arbitrary 2D atom distribution could be achieved. Ideally one would like a system where a number of complex atom distributions and potentials could be utilised to study such physics as transport dynamics [165], edge states [166] and local entropy [26]. A spatial light modulator (SLM) can allow for the creation of complex 2D [61] and 3D [62] atom distributions and also provide a way to eliminate the continuously varying chemical potential created by the Gaussian trapping potential. An SLM can shape the phase front of an input beam and project a potential onto the atoms if passed back through a focusing lens. This has been using to create a variety of 2D atom distributions, most notably in thermal atom systems with separation distances of a few µm [61].

Realising novel potentials with atoms in an optical lattice provides a reconfigurable test bed for quantum-simulation experiments. Another technical improvement of our machine is the ability to change lattice configurations, from square to triangular. Triangular lattices are of a particular interest as they open up the possibility of studying frustrated systems [167–169]. Triangular lattices also allow for the possibility to create kagome lattices [170], which opens up the possibility to study complex physics such as, the ground state kagome antiferromagnet, crystalline ordering and quantum spin liquids [171, 172]. A key aspect of our quantum-gas microscope is the ability to change the experiment dependent on the physics that is wanting to be investigated. This will be primarily achieved by the customisable trap potentials which are created by an SLM and allow us to probe a huge range of parameters for essentially the same experimental apparatus.

6.3 Dual species

One of the main long term experimental goals, is the implementation of a second atomic species into the experiment, ^{85}Rb. Two-component bosonic systems can result in fascinating physics, even for atoms just in the Mott-insulating regime [173]. These

systems[1] can then be used to study such complex fields as quantum magnetism [174], quantum-phase transitions [175] and even spin-charge separation in effective 1D systems [176]. To describe such systems one can assume the atoms are cold enough to be trapped within the lowest Bloch band of the potential wells created by the optical lattices and the dynamics of the system can be described through a two-component Bose-Hubbard model, given by [173],

$$\begin{aligned} H = -t_a \sum_{\langle i,j \rangle} (\hat{a}_i^\dagger \hat{a}_j + \text{h.c}) - t_b \sum_{\langle i,j \rangle} (\hat{b}_i^\dagger \hat{b}_j + \text{h.c}) + U \sum_i (\hat{n}_{ai} - \frac{1}{2})(\hat{n}_{bi} - \frac{1}{2}) \\ + \frac{1}{2} \sum_{i\alpha=a,b} V_\alpha \hat{n}_{\alpha i}(\hat{n}_{\alpha i} - 1) - \sum_{i\alpha} \mu_\alpha \hat{n}_{\alpha i}. \end{aligned} \tag{6.1}$$

The nearest neighbour sites are denoted by $\langle i, j \rangle$ with the spin states of the different component bosons being denoted by a, b. The annihilation and creation operators are given by $\hat{a}_i, \hat{b}_i$ and $\hat{a}_i^\dagger, \hat{b}_i^\dagger$ with the boson occupation number for each species on site i being $\hat{n}_{ia}$ and $\hat{n}_{ib}$. The spin-dependent tunneling matrix elements are $t_{a(b)}$ with the on-site interaction energy U, while the inter-species interaction is given by $V_{a(b)}$. Unlike in a single-component system where one can control the interaction by tuning the depth of the potential, a two-component system needs to be able to control the intra-species interaction. Feshbach resonances between the two components can be utilised to control the scattering lengths of each component [177] and probe new, exciting physics.

Implementation of a second species into the existing experimental setup would have been almost impossible without design and planning before the experiment was built. The atomic source used in the experiment is that of natural rubidium, so it already contains each species. All of the laser systems required for the cooling and trapping of ^{85}Rb have been planned to propagate in the same paths that exist for the current cooling and trapping of ^{87}Rb - saving space and ensuring the same alignment for the

[1] It should also be noted that a dual species system that traps atoms within triangular lattices is the perfect platform for exploring frustrated systems [167] and the complex dynamics behind spin impurities [50].

second species. The main challenging issue when implementing ^{85}Rb, is the need for additional magnetic coils which are responsible for the creation of the large magnetic fields required to reach Feshbach resonances. For ^{85}Rb-^{85}Rb, there are three resonances within a "reasonable" magnetic field regime[2] where both atoms are in $F = 2, m_F = 2$ state - 165 G, 171 G and 369 G [178]. For a mixture of ^{85}Rb-^{87}Rb, there are two resonances which can be accessed when ^{85}Rb and ^{87}Rb are in states $F = 2, m_F = -2$ and $F = 1, m_F = -1$ respectively - 271 G and 382 G [179]. The requirement of large magnetic fields require large magnetic coils, not only do they need to fit around the science chamber but also around the initial MOT cooling chamber, where forced and sympathetic evaporation will be performed. Therefore, these coils had to be placed around the chamber before any of the other optics were implemented.

6.4 Conclusion

Single-site resolved imaging of ultracold bosons in an optical lattice has been developed over the past decade and interest in quantum-gas microscopes, for various quantum-simulation applications, has grown substantially from two labs to over a dozen. Over the four years of my PhD, I have managed to take an empty lab and transform it into a complex machine that is capable of imaging and manipulating single atoms. Considering during the majority of the last four years, there was a maximum of two people working on the experiment, I feel that this is a huge achievement for any experimentalist. This thesis has shown two main results: the fast creation of an all optical BEC of ^{87}Rb and the efficient creation and imaging of a single layer of ^{87}Rb with single-site resolution. The fast creation of an all-optical BEC shows that, even in a complex machine that has been designed for quantum-simulation experiments there is still the possibility to explore other avenues, which may seem to be well established. The long-term goal of the experiment is to create a configurable dual-species quantum-gas microscope that

[2]Reasonable is defined in this case, as anything below 400 G. Anything above this value and the calculated water pressure required for the efficient cooling of the magnetic coils - which are sealed using a neoprene gasket - would not be achievable.

is suitable for a broad variety of quantum-simulation experiments. I believe that the work I have done will hopefully benefit a new generation of PhD students and produce remarkable research results on spin frustration, out-of-equilibrium dynamics and impurity dynamics.

Appendix A

Coil design

The coils responsible for the the creation of the magnetic gradient were placed above and below the science chamber. The objective below the chamber puts stringent requirements on the size of the coils. A cross section of the objective inside the bottom vacuum window atop the microscope board is shown in figure A.1. As can be seen, the space between the bottom side of the vacuum window and the mount that the objective is attached to is quite small. There is a total separation of 56.85 mm between the two. This is the space in which the gradient coil has to be placed. This space is even further reduced when taking into account the vacuum gasket and the bolts which are attached to the flange. This results in an maximum absolute width of the coil holders being 50 mm.

The coil holders were made of brass with an overall width of 34 mm and an outer diameter of 170 mm with the inner diameter for the wire of 76 mm. The interesting part of the coil support is the water cooling through a snaking channel cut into one side of the holder. This design (shown in figure A.2) allows for water to pass across the full area of one side of the coil holder. Although this design is not new, we did use a new method of sealing the coil. In the past, groups at Strathclyde have soldered a lid onto the coil mount to make it watertight, but this once lead to a leak in the joints between the two. Our method instead uses a neoprene gasket which is compressed down onto the top of the mount over the water channel and reduces the chance of a leak.

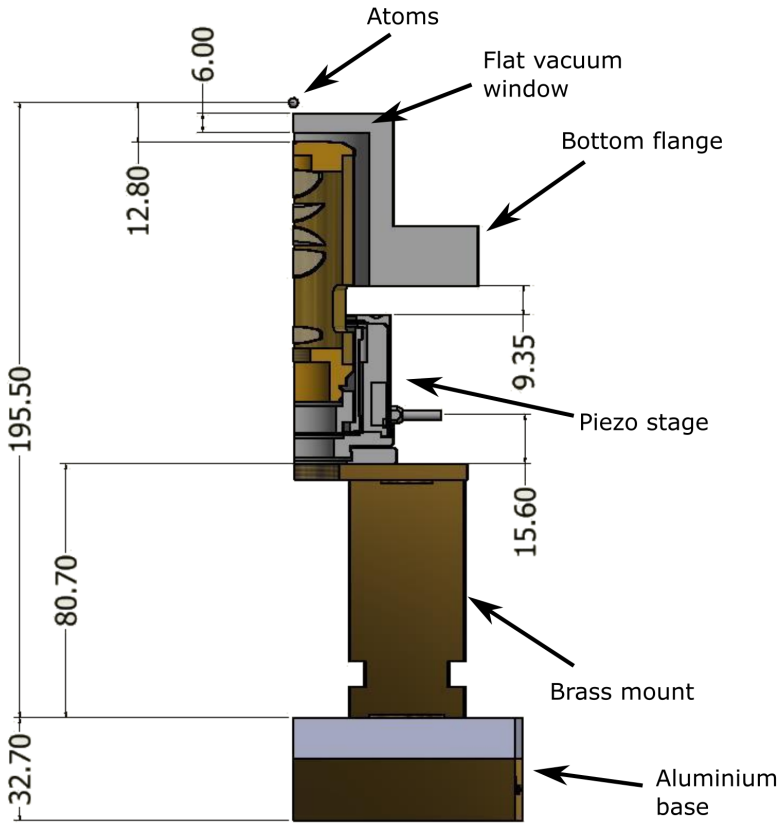

Figure A.1: A cross section of the objective with exact size measurements. The support board is below the objective with the bottom vacuum window above it.

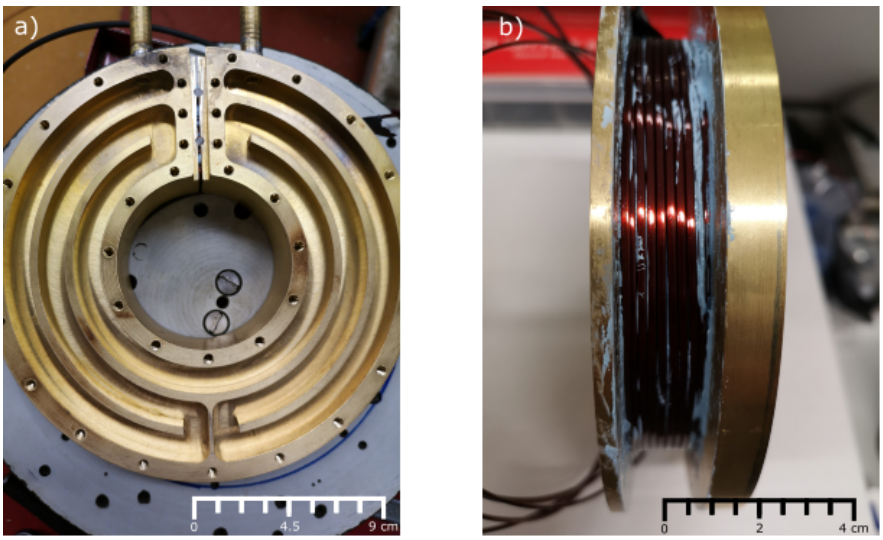

Figure A.2: a) Image of the gradient coil support with water channel visible. b) Image of the support during winding of the coil with blue thermal paste between each layer of windings.

One of the downsides to using a compression-fitted rubber gasket over a soldered seal, is that the water channel will not be able to handle as much pressure. This can be a point of concern as lower flow through the channel will result in a lower rate of heat extraction. This is due to the cold water having time to heat up at the start of the channel and then not efficiently removing heat from the end of it. A number of tests were performed once the wire had been wound round the holder. The wire used was rectangular 2×1 mm copper wire which was wound for 9 windings with 25 layers resulting in a total resistance of 2.1 Ω. To test how well the water cooling dissipates heat, 50 A is passed through the coil for 5 minutes with a cycle time of 10 seconds on and 30 seconds off. During the test, temperature measurements were taken of the outer surface of the coil, the back of the brass mount and the top of the water channel continuously. Infrared images of the maximum temperatures measured of the outer surface of the coil and the uncooled side of the brass mount are shown in figure A.3. The water cooling is able to keep a 90 °C difference between the coil and the mount. This cooling is essential as the coil mount is attached directly onto the science chamber and the objective is placed through the center of the bottom coil. Any heating of the chamber or the objective could cause irreversible damage to either part.

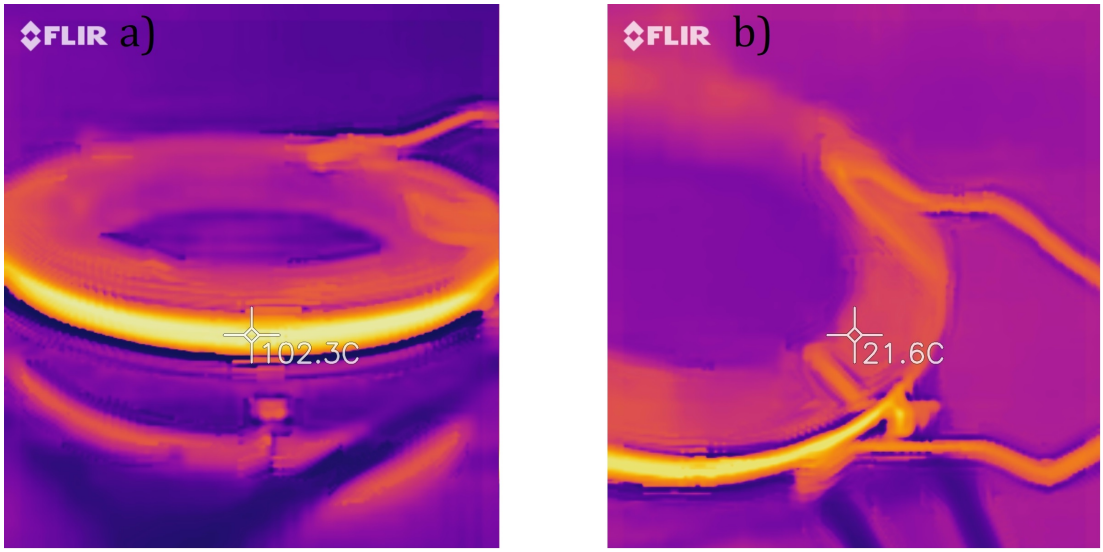

Figure A.3: FLIR infrared images of a gradient coil after a cycle time test. a) Maximum temperature of the uncooled outer surface of the coil - 102.3 °C. b) Maximum temperature of the uncooled back side of the brass mount - 21.6 °C.

Bibliography

[1] M. P. Fisher, P. B. Weichman, G. Grinstein, and D. S. Fisher, "Boson localization and the superfluid-insulator transition," *Physical Review B*, vol. 40, no. 1, p. 546, 1989.

[2] D. A. Steck, "Rubidium 87 D line data," 2001.

[3] D. A. Cotta, *A single-site resolution fermionic quantum-gas microscope*. PhD thesis, University of Strathclyde, 2018.

[4] R. Shankar, *Principles of quantum mechanics*. Springer Science & Business Media, 2012.

[5] G. Benenti and G. Strini, "Quantum simulation of the single-particle Schrödinger equation," *American Journal of Physics*, vol. 76, no. 7, pp. 657–662, 2008.

[6] V. Burdyuzha, O. Lalakulich, Y. Ponomarev, and G. Vereshkov, "New scenario for the early evolution of the universe," *Physical Review D*, vol. 55, no. 12, p. R7340, 1997.

[7] J. Preskill, "Quantum computing in the NISQ era and beyond," *Quantum*, vol. 2, p. 79, 2018.

[8] G. Benenti, G. Casati, and G. Strini, *Principles of Quantum Computation and Information-Volume II: Basic Tools and Special Topics*. World Scientific Publishing Company, 2007.

[9] F. Arute, K. Arya, R. Babbush, D. Bacon, J. C. Bardin, R. Barends, R. Biswas, S. Boixo, F. G. Brandao, D. A. Buell, *et al.*, "Quantum supremacy using a pro-

grammable superconducting processor," *Nature*, vol. 574, no. 7779, pp. 505–510, 2019.

[10] G. Wendin, "Quantum information processing with superconducting circuits: a review," *Reports on Progress in Physics*, vol. 80, no. 10, p. 106001, 2017.

[11] P. Krantz, M. Kjaergaard, F. Yan, T. P. Orlando, S. Gustavsson, and W. D. Oliver, "A quantum engineer's guide to superconducting qubits," *Applied Physics Reviews*, vol. 6, no. 2, p. 021318, 2019.

[12] J. I. Cirac and P. Zoller, "Quantum computations with cold trapped ions," *Physical Review Letters*, vol. 74, no. 20, p. 4091, 1995.

[13] K. Wright, K. Beck, S. Debnath, J. Amini, Y. Nam, N. Grzesiak, J.-S. Chen, N. Pisenti, M. Chmielewski, C. Collins, *et al.*, "Benchmarking an 11-qubit quantum computer," *Nature Communications*, vol. 10, no. 1, pp. 1–6, 2019.

[14] C. Figgatt, A. Ostrander, N. M. Linke, K. A. Landsman, D. Zhu, D. Maslov, and C. Monroe, "Parallel entangling operations on a universal ion-trap quantum computer," *Nature*, vol. 572, no. 7769, pp. 368–372, 2019.

[15] A. Aspuru-Guzik and P. Walther, "Photonic quantum simulators," *Nature Physics*, vol. 8, no. 4, pp. 285–291, 2012.

[16] J.-L. Tambasco, G. Corrielli, R. J. Chapman, A. Crespi, O. Zilberberg, R. Osellame, and A. Peruzzo, "Quantum interference of topological states of light," *Science Advances*, vol. 4, no. 9, 2018.

[17] K. Sun, J. Gao, M.-M. Cao, Z.-Q. Jiao, Y. Liu, Z.-M. Li, E. Poem, A. Eckstein, R.-J. Ren, X.-L. Pang, *et al.*, "Mapping and measuring large-scale photonic correlation with single-photon imaging," *Optica*, vol. 6, no. 3, pp. 244–249, 2019.

[18] H.-S. Zhong, H. Wang, Y.-H. Deng, M.-C. Chen, L.-C. Peng, Y.-H. Luo, J. Qin, D. Wu, X. Ding, Y. Hu, *et al.*, "Quantum computational advantage using photons," *Science*, vol. 370, no. 6523, pp. 1460–1463, 2020.

[19] D. S. Weiss and M. Saffman, "Quantum computing with neutral atoms," *Physics Today*, vol. 70, no. 7, 2017.

[20] I. S. Madjarov, J. P. Covey, A. L. Shaw, J. Choi, A. Kale, A. Cooper, H. Pichler, V. Schkolnik, J. R. Williams, and M. Endres, "High-fidelity entanglement and detection of alkaline-earth Rydberg atoms," *Nature Physics*, vol. 16, no. 8, pp. 857–861, 2020.

[21] M. Saffman, T. G. Walker, and K. Mølmer, "Quantum information with Rydberg atoms," *Reviews of Modern Physics*, vol. 82, no. 3, p. 2313, 2010.

[22] G. Zhu, Y. Subaşı, J. D. Whitfield, and M. Hafezi, "Hardware-efficient fermionic simulation with a cavity–QED system," *Quantum Information*, vol. 4, no. 1, pp. 1–10, 2018.

[23] C. Yang, K. Chan, R. Harper, W. Huang, T. Evans, J. Hwang, B. Hensen, A. Laucht, T. Tanttu, F. Hudson, *et al.*, "Silicon qubit fidelities approaching incoherent noise limits via pulse engineering," *Nature Electronics*, vol. 2, no. 4, pp. 151–158, 2019.

[24] W. S. Bakr, J. I. Gillen, A. Peng, S. Fölling, and M. Greiner, "A quantum gas microscope for detecting single atoms in a Hubbard-regime optical lattice," *Nature*, vol. 462, no. 7269, pp. 74–77, 2009.

[25] R. P. Feynman, "Simulating physics with computers," in *Feynman and computation*, pp. 133–153, CRC Press, 2018.

[26] J. F. Sherson, C. Weitenberg, M. Endres, M. Cheneau, I. Bloch, and S. Kuhr, "Single-atom-resolved fluorescence imaging of an atomic Mott insulator," *Nature*, vol. 467, no. 7311, pp. 68–72, 2010.

[27] H. Metcalf and P. van der Straten, "Cooling and trapping of neutral atoms," *Physics Reports*, vol. 244, no. 4-5, pp. 203–286, 1994.

[28] W. D. Phillips and H. Metcalf, "Laser deceleration of an atomic beam," *Physical Review Letters*, vol. 48, no. 9, p. 596, 1982.

[29] E. Raab, M. Prentiss, A. Cable, S. Chu, and D. E. Pritchard, "Trapping of neutral sodium atoms with radiation pressure," *Physical Review Letters*, vol. 59, no. 23, p. 2631, 1987.

[30] C. Townsend, N. Edwards, C. Cooper, K. Zetie, C. Foot, A. Steane, P. Szriftgiser, H. Perrin, and J. Dalibard, "Phase-space density in the magneto-optical trap," *Physical Review A*, vol. 52, no. 2, p. 1423, 1995.

[31] H. F. Hess, "Evaporative cooling of magnetically trapped and compressed spin-polarized hydrogen," *Physical Review B*, vol. 34, no. 5, p. 3476, 1986.

[32] N. Masuhara, J. M. Doyle, J. C. Sandberg, D. Kleppner, T. J. Greytak, H. F. Hess, and G. P. Kochanski, "Evaporative cooling of spin-polarized atomic hydrogen," *Physical Review Letters*, vol. 61, no. 8, p. 935, 1988.

[33] M. H. Anderson, J. R. Ensher, M. R. Matthews, C. E. Wieman, and E. A. Cornell, "Observation of Bose-Einstein condensation in a dilute atomic vapor," *Science*, vol. 269, no. 5221, pp. 198–201, 1995.

[34] K. B. Davis, M.-O. Mewes, M. R. Andrews, N. J. van Druten, D. S. Durfee, D. Kurn, and W. Ketterle, "Bose-Einstein condensation in a gas of sodium atoms," *Physical Review Letters*, vol. 75, no. 22, p. 3969, 1995.

[35] M. Barrett, J. Sauer, and M. Chapman, "All-optical formation of an atomic Bose-Einstein condensate," *Physical Review Letters*, vol. 87, no. 1, p. 010404, 2001.

[36] D. Jaksch, C. Bruder, J. I. Cirac, C. W. Gardiner, and P. Zoller, "Cold bosonic atoms in optical lattices," *Physical Review Letters*, vol. 81, no. 15, p. 3108, 1998.

[37] I. Bloch, "Quantum simulations come of age," *Nature Physics*, vol. 14, no. 12, pp. 1159–1161, 2018.

[38] P. S. Jessen and I. Deutsch, "Optical lattices," *Advances in Atomic, Molecular, and Optical Physics*, vol. 37, pp. 95–138, 1996.

[39] J. I. Gillen, *The Quantum Gas Microscope*. PhD thesis, Harvard University, Cambridge, Massachusetts, 2009.

[40] V. Vuletić, C. Chin, A. J. Kerman, and S. Chu, "Degenerate Raman sideband cooling of trapped cesium atoms at very high atomic densities," *Physical Review Letters*, vol. 81, no. 26, p. 5768, 1998.

[41] B. P. Anderson and M. A. Kasevich, "Macroscopic quantum interference from atomic tunnel arrays," *Science*, vol. 282, no. 5394, pp. 1686–1689, 1998.

[42] S. Rolston, "Optical lattices," *Physics World*, vol. 11, no. 10, p. 27, 1998.

[43] M. Greiner, O. Mandel, T. Esslinger, T. W. Hänsch, and I. Bloch, "Quantum phase transition from a superfluid to a Mott insulator in a gas of ultracold atoms," *Nature*, vol. 415, no. 6867, pp. 39–44, 2002.

[44] I. Bloch, J. Dalibard, and S. Nascimbene, "Quantum simulations with ultracold quantum gases," *Nature Physics*, vol. 8, no. 4, pp. 267–276, 2012.

[45] C. Weitenberg, *Single-atom resolved imaging and manipulation in an atomic Mott insulator*. PhD thesis, Ludwig Maximilian University of Munich, 2011.

[46] J. Simon, W. S. Bakr, R. Ma, M. E. Tai, P. M. Preiss, and M. Greiner, "Quantum simulation of antiferromagnetic spin chains in an optical lattice," *Nature*, vol. 472, no. 7343, pp. 307–312, 2011.

[47] R. Islam, R. Ma, P. M. Preiss, M. E. Tai, A. Lukin, M. Rispoli, and M. Greiner, "Measuring entanglement entropy in a quantum many-body system," *Nature*, vol. 528, no. 7580, pp. 77–83, 2015.

[48] M. Endres, M. Cheneau, T. Fukuhara, C. Weitenberg, P. Schauss, C. Gross, L. Mazza, M. C. Banuls, L. Pollet, I. Bloch, *et al.*, "Observation of correlated particle-hole pairs and string order in low-dimensional mott insulators," *Science*, vol. 334, no. 6053, pp. 200–203, 2011.

[49] M. Endres, M. Cheneau, T. Fukuhara, C. Weitenberg, P. Schauß, C. Gross, L. Mazza, M. C. Bañuls, L. Pollet, I. Bloch, *et al.*, "Single-site and single-atom resolved measurement of correlation functions," *Applied Physics B*, vol. 113, no. 1, pp. 27–39, 2013.

[50] T. Fukuhara, A. Kantian, M. Endres, M. Cheneau, P. Schauß, S. Hild, D. Bellem, U. Schollwöck, T. Giamarchi, C. Gross, *et al.*, "Quantum dynamics of a mobile spin impurity," *Nature Physics*, vol. 9, no. 4, pp. 235–241, 2013.

[51] A. Lukin, M. Rispoli, R. Schittko, M. E. Tai, A. M. Kaufman, S. Choi, V. Khemani, J. Léonard, and M. Greiner, "Probing entanglement in a many-body–localized system," *Science*, vol. 364, no. 6437, pp. 256–260, 2019.

[52] P. M. Preiss, R. Ma, M. E. Tai, A. Lukin, M. Rispoli, P. Zupancic, Y. Lahini, R. Islam, and M. Greiner, "Strongly correlated quantum walks in optical lattices," *Science*, vol. 347, no. 6227, pp. 1229–1233, 2015.

[53] E. Haller, J. Hudson, A. Kelly, D. A. Cotta, B. Peaudecerf, G. D. Bruce, and S. Kuhr, "Single-atom imaging of fermions in a quantum-gas microscope," *Nature Physics*, vol. 11, no. 9, pp. 738–742, 2015.

[54] M. F. Parsons, F. Huber, A. Mazurenko, C. S. Chiu, W. Setiawan, K. Wooley-Brown, S. Blatt, and M. Greiner, "Site-resolved imaging of fermionic ^{6}Li in an optical lattice," *Physical Review Letters*, vol. 114, no. 21, p. 213002, 2015.

[55] L. W. Cheuk, M. A. Nichols, M. Okan, T. Gersdorf, V. V. Ramasesh, W. S. Bakr, T. Lompe, and M. W. Zwierlein, "Quantum-gas microscope for fermionic atoms," *Physical Review Letters*, vol. 114, no. 19, p. 193001, 2015.

[56] A. Mazurenko, C. S. Chiu, G. Ji, M. F. Parsons, M. Kanász-Nagy, R. Schmidt, F. Grusdt, E. Demler, D. Greif, and M. Greiner, "A cold-atom Fermi–Hubbard antiferromagnet," *Nature*, vol. 545, no. 7655, pp. 462–466, 2017.

[57] M. Boll, T. A. Hilker, G. Salomon, A. Omran, J. Nespolo, L. Pollet, I. Bloch, and C. Gross, "Spin-and density-resolved microscopy of antiferromagnetic correlations in Fermi-Hubbard chains," *Science*, vol. 353, no. 6305, pp. 1257–1260, 2016.

[58] L. W. Cheuk, M. A. Nichols, K. R. Lawrence, M. Okan, H. Zhang, E. Khatami, N. Trivedi, T. Paiva, M. Rigol, and M. W. Zwierlein, "Observation of spatial

charge and spin correlations in the 2D fermi-hubbard model," *Science*, vol. 353, no. 6305, pp. 1260–1264, 2016.

[59] Y. Wang, X. Zhang, T. A. Corcovilos, A. Kumar, and D. S. Weiss, "Coherent addressing of individual neutral atoms in a 3D optical lattice," *Physical Review Letters*, vol. 115, no. 4, p. 043003, 2015.

[60] P. Zupancic, P. M. Preiss, R. Ma, A. Lukin, M. E. Tai, M. Rispoli, R. Islam, and M. Greiner, "Ultra-precise holographic beam shaping for microscopic quantum control," *Optics Express*, vol. 24, no. 13, pp. 13881–13893, 2016.

[61] D. Barredo, S. De Léséleuc, V. Lienhard, T. Lahaye, and A. Browaeys, "An atom-by-atom assembler of defect-free arbitrary two-dimensional atomic arrays," *Science*, vol. 354, no. 6315, pp. 1021–1023, 2016.

[62] D. Barredo, V. Lienhard, S. De Leseleuc, T. Lahaye, and A. Browaeys, "Synthetic three-dimensional atomic structures assembled atom by atom," *Nature*, vol. 561, no. 7721, pp. 79–82, 2018.

[63] R. Yamamoto, J. Kobayashi, T. Kuno, K. Kato, and Y. Takahashi, "An ytterbium quantum gas microscope with narrow-line laser cooling," *New Journal of Physics*, vol. 18, no. 2, p. 023016, 2016.

[64] M. Miranda, R. Inoue, Y. Okuyama, A. Nakamoto, and M. Kozuma, "Site-resolved imaging of ytterbium atoms in a two-dimensional optical lattice," *Physical Review A*, vol. 91, no. 6, p. 063414, 2015.

[65] G. A. Phelps, *A dipolar quantum gas microscope*. PhD thesis, Harvard University, Cambridge, Massachusetts, 2019.

[66] J. Koepsell, S. Hirthe, D. Bourgund, P. Sompet, J. Vijayan, G. Salomon, C. Gross, and I. Bloch, "Robust bilayer charge pumping for spin-and density-resolved quantum gas microscopy," *Physical Review Letters*, vol. 125, no. 1, p. 010403, 2020.

[67] H. Bernien, S. Schwartz, A. Keesling, H. Levine, A. Omran, H. Pichler, S. Choi, A. S. Zibrov, M. Endres, M. Greiner, *et al.*, "Probing many-body dynamics on a 51-atom quantum simulator," *Nature*, vol. 551, no. 7682, pp. 579–584, 2017.

[68] H. Labuhn, D. Barredo, S. Ravets, S. De Léséleuc, T. Macrì, T. Lahaye, and A. Browaeys, "Tunable two-dimensional arrays of single Rydberg atoms for realizing quantum Ising models," *Nature*, vol. 534, no. 7609, pp. 667–670, 2016.

[69] J. Zhang, G. Pagano, P. W. Hess, A. Kyprianidis, P. Becker, H. Kaplan, A. V. Gorshkov, Z.-X. Gong, and C. Monroe, "Observation of a many-body dynamical phase transition with a 53-qubit quantum simulator," *Nature*, vol. 551, no. 7682, pp. 601–604, 2017.

[70] A. Ulibarrena, *Creation of an All-Optical Bose-Einstein Condensate*. PhD thesis, University of Strathclyde, 2020.

[71] W. Ketterle, *Twenty years of atomic quantum gases: 1995-2015*. Cambridge University Press, 2017.

[72] S. Chu, "Laser manipulation of atoms and particles," *Science*, vol. 253, no. 5022, pp. 861–866, 1991.

[73] K. Dieckmann, R. Spreeuw, M. Weidemüller, and J. Walraven, "Two-dimensional magneto-optical trap as a source of slow atoms," *Physical Review A*, vol. 58, no. 5, p. 3891, 1998.

[74] A. Steane and C. Foot, "Laser cooling below the Doppler limit in a magneto-optical trap," *Europhysics Letters*, vol. 14, no. 3, p. 231, 1991.

[75] P. D. Lett, W. D. Phillips, S. Rolston, C. E. Tanner, R. Watts, and C. Westbrook, "Optical molasses," *Journal of the Optical Society of America B*, vol. 6, no. 11, pp. 2084–2107, 1989.

[76] C. S. Adams, H. J. Lee, N. Davidson, M. Kasevich, and S. Chu, "Evaporative cooling in a crossed dipole trap," *Physical Review Letters*, vol. 74, no. 18, p. 3577, 1995.

[77] C. J. Foot *et al.*, *Atomic Physics*, vol. 7. Oxford University Press, 2005.

[78] H. Metcalf, V. der Straten, and P. L. Cooling, "Laser cooling and trapping," *Graduate Texts in Contemporary Physics Springer New York*, 1999.

[79] F. Dalfovo, S. Giorgini, L. P. Pitaevskii, and S. Stringari, "Theory of Bose-Einstein condensation in trapped gases," *Reviews of Modern Physics*, vol. 71, no. 3, p. 463, 1999.

[80] D. J. Wineland and W. M. Itano, "Laser cooling of atoms," *Physical Review A*, vol. 20, no. 4, p. 1521, 1979.

[81] T. W. Hänsch and A. L. Schawlow, "Cooling of gases by laser radiation," *Optics Communications*, vol. 13, no. 1, pp. 68–69, 1975.

[82] P. D. Lett, R. N. Watts, C. I. Westbrook, W. D. Phillips, P. L. Gould, and H. J. Metcalf, "Observation of atoms laser cooled below the Doppler limit," *Physical Review Letters*, vol. 61, no. 2, p. 169, 1988.

[83] T. Binnewies, G. Wilpers, U. Sterr, F. Riehle, J. Helmcke, T. Mehlstäubler, E. M. Rasel, and W. Ertmer, "Doppler cooling and trapping on forbidden transitions," *Physical Review Letters*, vol. 87, no. 12, p. 123002, 2001.

[84] C. Adams, S. Cox, E. Riis, and A. Arnold, "Laser cooling of calcium in a 'golden ratio'quasi-electrostatic lattice," *Journal of Physics B: Atomic, Molecular and Optical Physics*, vol. 36, no. 10, p. 1933, 2003.

[85] S. Stellmer, B. Pasquiou, R. Grimm, and F. Schreck, "Laser cooling to quantum degeneracy," *Physical Review Letters*, vol. 110, no. 26, p. 263003, 2013.

[86] A. Steane, M. Chowdhury, and C. Foot, "Radiation force in the magneto-optical trap," *Journal of the Optical Society of America B*, vol. 9, no. 12, pp. 2142–2158, 1992.

[87] C. N. Cohen-Tannoudji and W. D. Phillips, "New mechanisms for laser cooling," *Physics Today*, vol. 43, no. 10, pp. 33–40, 1990.

[88] J. Dalibard and C. Cohen-Tannoudji, "Laser cooling below the Doppler limit by polarization gradients: simple theoretical models," *Journal of the Optical Society of America B*, vol. 6, no. 11, pp. 2023–2045, 1989.

[89] C. S. Adams and E. Riis, "Laser cooling and manipulation of neutral particles," *The New Optics*, pp. 1–39, 1997.

[90] P. Hamilton, G. Kim, T. Joshi, B. Mukherjee, D. Tiarks, and H. Müller, "Sisyphus cooling of lithium," *Physical Review A*, vol. 89, no. 2, p. 023409, 2014.

[91] C. Triché, P. Verkerk, and G. Grynberg, "Blue-Sisyphus cooling in cesium gray molasses and antidot lattices," *The European Physical Journal D-Atomic, Molecular, Optical and Plasma Physics*, vol. 5, no. 2, pp. 225–228, 1999.

[92] J. Lim, J. Almond, M. Trigatzis, J. Devlin, N. Fitch, B. Sauer, M. Tarbutt, and E. Hinds, "Laser cooled YbF molecules for measuring the electron's electric dipole moment," *Physical Review Letters*, vol. 120, no. 12, p. 123201, 2018.

[93] E. S. Shuman, J. F. Barry, and D. DeMille, "Laser cooling of a diatomic molecule," *Nature*, vol. 467, no. 7317, pp. 820–823, 2010.

[94] S. Truppe, H. Williams, M. Hambach, L. Caldwell, N. Fitch, E. Hinds, B. Sauer, and M. Tarbutt, "Molecules cooled below the Doppler limit," *Nature Physics*, vol. 13, no. 12, pp. 1173–1176, 2017.

[95] J. McFerran, L. Yi, S. Mejri, and S. Bize, "Sub-Doppler cooling of fermionic Hg isotopes in a magneto-optical trap," *Optics Letters*, vol. 35, no. 18, pp. 3078–3080, 2010.

[96] J. Miao, J. Hostetter, G. Stratis, and M. Saffman, "Magneto-optical trapping of holmium atoms," *Physical Review A*, vol. 89, no. 4, p. 041401, 2014.

[97] Y. Castin, K. Berg-So, J. Dalibard, and K. Mo, "Two-dimensional Sisyphus cooling," *Physical Review A*, vol. 50, no. 6, p. 5092, 1994.

[98] H. Katori, T. Ido, Y. Isoya, and M. Kuwata-Gonokami, "Magneto-optical trapping and cooling of strontium atoms down to the photon recoil temperature," *Physical Review Letters*, vol. 82, no. 6, p. 1116, 1999.

[99] J. Jersblad, H. Ellmann, and A. Kastberg, "Experimental investigation of the limit of Sisyphus cooling," *Physical Review A*, vol. 62, no. 5, p. 051401, 2000.

[100] C. Soloman, J. Dalibard, W. Phillips, A. Clairon, and S. Guellati, "Laser cooling of cesium atoms below 3 μK," *Europhysics Letters*, vol. 12, pp. 683–688, 1990.

[101] N. R. Newbury, C. Myatt, E. A. Cornell, and C. Wieman, "Gravitational Sisyphus cooling of ^{87}Rb in a magnetic trap," *Physical Review Letters*, vol. 74, no. 12, p. 2196, 1995.

[102] D. Lucas, P. Horak, and G. Grynberg, "Sisyphus cooling of rubidium atoms on the D_2 line: The role of the neighbouring transitions," *The European Physical Journal D-Atomic, Molecular, Optical and Plasma Physics*, vol. 7, no. 3, pp. 261–267, 1999.

[103] D. Boiron, A. Michaud, J. Fournier, L. Simard, M. Sprenger, G. Grynberg, and C. Salomon, "Cold and dense cesium clouds in far-detuned dipole traps," *Physical Review A*, vol. 57, no. 6, p. R4106, 1998.

[104] M. Shahriar, P. Hemmer, M. Prentiss, P. Marte, J. Mervis, D. Katz, N. Bigelow, and T. Cai, "Continuous polarization-gradient precooling-assisted velocity-selective coherent population trapping," *Physical Review A*, vol. 48, no. 6, p. R4035, 1993.

[105] D. Boiron, C. Triché, D. Meacher, P. Verkerk, and G. Grynberg, "Three-dimensional cooling of cesium atoms in four-beam gray optical molasses," *Physical Review A*, vol. 52, no. 5, p. R3425, 1995.

[106] M. Weidemüller, T. Esslinger, M. A. Ol'shanii, A. Hemmerich, and T. W. Hänsch, "A novel scheme for efficient cooling below the photon recoil limit," *EPL (Europhysics Letters)*, vol. 27, no. 2, p. 109, 1994.

[107] G. D. Bruce, E. Haller, B. Peaudecerf, D. A. Cotta, M. Andia, S. Wu, M. Y. Johnson, B. W. Lovett, and S. Kuhr, "Sub-Doppler laser cooling of ^{40}K with Raman gray molasses on the D_2 line," *Journal of Physics B: Atomic, Molecular and Optical Physics*, vol. 50, no. 9, p. 095002, 2017.

[108] G. Salomon, L. Fouché, P. Wang, A. Aspect, P. Bouyer, and T. Bourdel, "Gray-molasses cooling of ^{39}K to a high phase-space density," *Europhysics Letters*, vol. 104, no. 6, p. 63002, 2014.

[109] S. Rosi, A. Burchianti, S. Conclave, D. S. Naik, G. Roati, C. Fort, and F. Minardi, "Λ-enhanced grey molasses on the D_2 transition of rubidium-87 atoms," *Scientific Reports*, vol. 8, no. 1, pp. 1–9, 2018.

[110] D. Boiron, A. Michaud, P. Lemonde, Y. Castin, C. Salomon, S. Weyers, K. Szymaniec, L. Cognet, and A. Clairon, "Laser cooling of cesium atoms in gray optical molasses down to 1.1 μK," *Physical Review A*, vol. 53, no. 6, p. R3734, 1996.

[111] A. J. Kerman, V. Vuletić, C. Chin, and S. Chu, "Beyond optical molasses: 3D Raman sideband cooling of atomic cesium to high phase-space density," *Physical Review Letters*, vol. 84, no. 3, p. 439, 2000.

[112] A. Griffin, D. W. Snoke, and S. Stringari, *Bose-Einstein condensation*. Cambridge University Press, 1996.

[113] F. Dalfovo, S. Giorgini, L. P. Pitaevskii, and S. Stringari, "Theory of Bose-Einstein condensation in trapped gases," *Reviews of Modern Physics*, vol. 71, no. 3, p. 463, 1999.

[114] F. London, "On the Bose-Einstein condensation," *Physical Review*, vol. 54, no. 11, p. 947, 1938.

[115] W. Ketterle, D. S. Durfee, and D. Stamper-Kurn, "Making, probing and understanding Bose-Einstein condensates," *ArXiv preprint cond-mat/9904034*, 1999.

[116] E. A. Cornell and C. E. Wieman, "The Bose-Einstein condensate," *Scientific American*, vol. 278, no. 3, pp. 40–45, 1998.

[117] O. Penrose and L. Onsager, "Bose-Einstein condensation and liquid helium," *Physical Review*, vol. 104, no. 3, p. 576, 1956.

[118] S. N. Bose, "Plancks gesetz und lichtquantenhypothese," *Physik*, vol. 26, pp. 178–181, 1924.

[119] A. Einstein, "Quantum theory of the monatomic ideal gas," *Academy lecture: Royal Prussian Academy of Sciences*, p. 261–267, 1924.

[120] C. J. Pethick and H. Smith, *Bose–Einstein condensation in dilute gases*. Cambridge university press, 2008.

[121] S. Stringari, "Bose–Einstein condensation and superfluidity in trapped atomic gases," *Comptes Rendus de l'Académie des Sciences-Series IV-Physics*, vol. 2, no. 3, pp. 381–397, 2001.

[122] W. Ketterle and N. Van Druten, "Evaporative cooling of trapped atoms," *Advances in Atomic, Molecular, and Optical Physics*, vol. 37, pp. 181–236, 1996.

[123] I. Bloch, J. Dalibard, and W. Zwerger, "Many-body physics with ultracold gases," *Reviews of Modern Physics*, vol. 80, no. 3, p. 885, 2008.

[124] L. P. Pitaevskii, "Vortex lines in an imperfect Bose gas," *Journal of Experimental and Theoretical Physics*, vol. 13, no. 2, pp. 451–454, 1961.

[125] E. P. Gross, "Structure of a quantized vortex in Boson systems," *Il Nuovo Cimento (1955-1965)*, vol. 20, no. 3, pp. 454–477, 1961.

[126] O. Morsch and M. Oberthaler, "Dynamics of Bose-Einstein condensates in optical lattices," *Reviews of Modern Physics*, vol. 78, no. 1, p. 179, 2006.

[127] I. Bloch, "Ultracold quantum gases in optical lattices," *Nature Physics*, vol. 1, no. 1, pp. 23–30, 2005.

[128] R. Grimm, M. Weidemüller, and Y. B. Ovchinnikov, "Optical dipole traps for neutral atoms," *Advances in Atomic, Molecular, and Optical Physics*, vol. 42, pp. 95–170, 2000.

[129] P. Törmä and K. Sengstock, *Quantum Gas Experiments*. World Scientific, 2014.

[130] H. Gersch and G. Knollman, "Quantum cell model for bosons," *Physical Review*, vol. 129, no. 2, p. 959, 1963.

[131] D. Jaksch and P. Zoller, "The cold atom Hubbard toolbox," *Annals of physics*, vol. 315, no. 1, pp. 52–79, 2005.

[132] A. J. Leggett, *Quantum liquids: Bose condensation and Cooper pairing in condensed-matter systems*. Oxford university press, 2006.

[133] M. Endres, *Probing correlated quantum many-body systems at the single-particle level*. PhD thesis, Ludwig Maximilian University of Munich, 2014.

[134] N. Gemelke, X. Zhang, C.-L. Hung, and C. Chin, "In situ observation of incompressible Mott-insulating domains in ultracold atomic gases," *Nature*, vol. 460, no. 7258, pp. 995–998, 2009.

[135] G. Batrouni, V. Rousseau, R. Scalettar, M. Rigol, A. Muramatsu, P. Denteneer, and M. Troyer, "Mott domains of bosons confined on optical lattices," *Physical Review Letters*, vol. 89, no. 11, p. 117203, 2002.

[136] J. Bjorkholm, "Collision-limited lifetimes of atom traps," *Physical Review A*, vol. 38, no. 3, p. 1599, 1988.

[137] T. Horiuchi and R. Reed, *Austenitic steels at low temperatures*. Springer Science & Business Media, 2012.

[138] P. D. Lett, R. N. Watts, C. I. Westbrook, W. D. Phillips, P. L. Gould, and H. J. Metcalf, "Observation of atoms laser cooled below the Doppler limit," *Physical Review Letters*, vol. 61, no. 2, p. 169, 1988.

[139] G. Grynberg and J.-Y. Courtois, "Proposal for a magneto-optical lattice for trapping atoms in nearly-dark states," *Europhysics Letters*, vol. 27, no. 1, p. 41, 1994.

[140] G. Colzi, G. Durastante, E. Fava, S. Serafini, G. Lamporesi, and G. Ferrari, "Sub-Doppler cooling of sodium atoms in gray molasses," *Physical Review A*, vol. 93, no. 2, p. 023421, 2016.

[141] J.-F. Clément, J.-P. Brantut, M. Robert-De-Saint-Vincent, R. A. Nyman, A. Aspect, T. Bourdel, and P. Bouyer, "All-optical runaway evaporation to Bose-Einstein condensation," *Physical Review A*, vol. 79, no. 6, p. 061406, 2009.

[142] J. Wu, R. Newell, M. Hausmann, D. J. Vieira, and X. Zhao, "Loading dynamics of optical trap and parametric excitation resonances of trapped atoms," *Journal of Applied Physics*, vol. 100, no. 5, p. 054903, 2006.

[143] D. Jacob, E. Mimoun, L. De Sarlo, M. Weitz, J. Dalibard, and F. Gerbier, "Production of sodium Bose–Einstein condensates in an optical dimple trap," *New Journal of Physics*, vol. 13, no. 6, p. 065022, 2011.

[144] E. Burt, R. Ghrist, C. Myatt, M. Holland, E. A. Cornell, and C. Wieman, "Coherence, correlations, and collisions: What one learns about Bose-Einstein condensates from their decay," *Physical Review Letters*, vol. 79, no. 3, p. 337, 1997.

[145] C. D. Colquhoun, *A New Apparatus for Experiments with Caesium Bose-Einstein Condensates*. PhD thesis, University of Strathclyde, 2019.

[146] B. Peaudecerf, M. Andia, M. Brown, E. Haller, and S. Kuhr, "Microwave preparation of two-dimensional fermionic spin mixtures," *New Journal of Physics*, vol. 21, no. 1, p. 013020, 2019.

[147] M. Ammenwerth, *An optical transport trap for quantum gas microscope experiments*. Internship report for the university of Strathclyde, 2019.

[148] T. Savard, K. O'hara, and J. Thomas, "Laser-noise-induced heating in far-off resonance optical traps," *Physical Review A*, vol. 56, no. 2, p. R1095, 1997.

[149] M. Khudaverdyan, W. Alt, I. Dotsenko, L. Förster, S. Kuhr, D. Meschede, Y. Miroshnychenko, D. Schrader, and A. Rauschenbeutel, "Adiabatic quantum

state manipulation of single trapped atoms," *Physical Review A*, vol. 71, no. 3, p. 031404, 2005.

[150] M. Garwood and L. DelaBarre, "The return of the frequency sweep: designing adiabatic pulses for contemporary NMR," *Journal of Magnetic Resonance*, vol. 153, no. 2, pp. 155–177, 2001.

[151] A. Itah, H. Veksler, O. Lahav, A. Blumkin, C. Moreno, C. Gordon, and J. Steinhauer, "Direct observation of a sub-poissonian number distribution of atoms in an optical lattice," *Physical Review Letters*, vol. 104, no. 11, p. 113001, 2010.

[152] T. Gericke, P. Würtz, D. Reitz, T. Langen, and H. Ott, "High-resolution scanning electron microscopy of an ultracold quantum gas," *Nature Physics*, vol. 4, no. 12, pp. 949–953, 2008.

[153] W. S. Bakr, A. Peng, M. E. Tai, R. Ma, J. Simon, J. I. Gillen, S. Foelling, L. Pollet, and M. Greiner, "Probing the superfluid–to–Mott insulator transition at the single-atom level," *Science*, vol. 329, no. 5991, pp. 547–550, 2010.

[154] J. F. Sherson, C. Weitenberg, M. Endres, M. Cheneau, I. Bloch, and S. Kuhr, "Single-atom-resolved fluorescence imaging of an atomic Mott insulator," *Nature*, vol. 467, no. 7311, pp. 68–72, 2010.

[155] P. Schauss, *High-resolution imaging of ordering in Rydberg many-body systems*. PhD thesis, Ludwig Maximilian University of Munich, 2015.

[156] V. N. Mahajan, "Strehl ratio for primary aberrations in terms of their aberration variance," *JOSA*, vol. 73, no. 6, pp. 860–861, 1983.

[157] A. T. Grier, I. Ferrier-Barbut, B. S. Rem, M. Delehaye, L. Khaykovich, F. Chevy, and C. Salomon, "λ-enhanced sub-doppler cooling of lithium atoms in D_1 gray molasses," *Physical Review A*, vol. 87, no. 6, p. 063411, 2013.

[158] D. R. Fernandes, F. Sievers, N. Kretzschmar, S. Wu, C. Salomon, and F. Chevy, "Sub-doppler laser cooling of fermionic ^{40}K atoms in three-dimensional gray optical molasses," *Europhysics Letters*, vol. 100, no. 6, p. 63001, 2012.

[159] M. Brown, T. Thiele, C. Kiehl, T.-W. Hsu, and C. Regal, "Gray-molasses optical-tweezer loading: controlling collisions for scaling atom-array assembly," *Physical Review X*, vol. 9, no. 1, p. 011057, 2019.

[160] J. Sasián and J. Sasian, *Introduction to aberrations in optical imaging systems*. Cambridge University Press, 2013.

[161] M. Born and E. Wolf, *Principles of optics: electromagnetic theory of propagation, interference and diffraction of light*. Elsevier, 2013.

[162] B. D. Guenther and D. Steel, *Encyclopedia of modern optics*. Academic Press, 2018.

[163] Data sheet. Leica Microsystems, *Point-spread function simulations for varying objective tilts*, 2012.

[164] W. S. Bakr, A. Peng, M. E. Tai, R. Ma, J. Simon, J. I. Gillen, S. Foelling, L. Pollet, and M. Greiner, "Probing the superfluid–to–Mott insulator transition at the single-atom level," *Science*, vol. 329, no. 5991, pp. 547–550, 2010.

[165] D. Husmann, S. Uchino, S. Krinner, M. Lebrat, T. Giamarchi, T. Esslinger, and J.-P. Brantut, "Connecting strongly correlated superfluids by a quantum point contact," *Science*, vol. 350, no. 6267, pp. 1498–1501, 2015.

[166] A. Joshi and R. Peters, "Mott transition and magnetism in a fragile topological insulator," *Physical Review B*, vol. 103, p. 165130, Apr 2021.

[167] A. Ramirez, "Geometrically frustrated matter—magnets to molecules," *MRS Bulletin*, vol. 30, no. 6, pp. 447–451, 2005.

[168] H. Diep *et al.*, *Frustrated spin systems*. World Scientific, 2013.

[169] A. Eckardt, P. Hauke, P. Soltan-Panahi, C. Becker, K. Sengstock, and M. Lewenstein, "Frustrated quantum antiferromagnetism with ultracold bosons in a triangular lattice," *Europhysics Letters*, vol. 89, no. 1, p. 10010, 2010.

[170] G.-B. Jo, J. Guzman, C. K. Thomas, P. Hosur, A. Vishwanath, and D. M. Stamper-Kurn, "Ultracold atoms in a tunable optical kagome lattice," *Physical review letters*, vol. 108, no. 4, p. 045305, 2012.

[171] J. Ruostekoski, "Optical Kagomé lattice for ultracold atoms with nearest neighbor interactions," *Physical Review Letters*, vol. 103, no. 8, p. 080406, 2009.

[172] L. Santos, M. Baranov, J. I. Cirac, H.-U. Everts, H. Fehrmann, and M. Lewenstein, "Atomic quantum gases in Kagomé lattices," *Physical Review Letters*, vol. 93, no. 3, p. 030601, 2004.

[173] E. Altman, W. Hofstetter, E. Demler, and M. D. Lukin, "Phase diagram of two-component bosons on an optical lattice," *New Journal of Physics*, vol. 5, no. 1, p. 113, 2003.

[174] L.-M. Duan, E. Demler, and M. D. Lukin, "Controlling spin exchange interactions of ultracold atoms in optical lattices," *Physical Review Letters*, vol. 91, no. 9, p. 090402, 2003.

[175] E. Demler and F. Zhou, "Spinor bosonic atoms in optical lattices: symmetry breaking and fractionalization," *Physical Review Letters*, vol. 88, no. 16, p. 163001, 2002.

[176] A. Recati, P. Fedichev, W. Zwerger, and P. Zoller, "Spin-charge separation in ultracold quantum gases," *Physical Review Letters*, vol. 90, no. 2, p. 020401, 2003.

[177] C. Chin, R. Grimm, P. Julienne, and E. Tiesinga, "Feshbach resonances in ultracold gases," *Reviews of Modern Physics*, vol. 82, no. 2, p. 1225, 2010.

[178] C. L. Blackley, C. R. Le Sueur, J. M. Hutson, D. J. McCarron, M. P. Köppinger, H.-W. Cho, D. L. Jenkin, and S. L. Cornish, "Feshbach resonances in ultracold ^{85}Rb," *Physical Review A*, vol. 87, no. 3, p. 033611, 2013.

[179] Z. Li, S. Singh, T. Tscherbul, and K. Madison, "Feshbach resonances in ultracold ^{85}Rb - ^{87}Rb and ^{6}Li - ^{87}Rb mixtures," *Physical Review A*, vol. 78, no. 2, p. 022710, 2008.